Millennial scale events from marine sediment cores in the SW Pacific during Marine Isotope Stage 3

By

Bryn Taiapa

A thesis
submitted to Victoria University of Wellington
in fulfilment of the requirements for the degree of
Master of Science in Geology.

School of Geography, Environmental and Earth Sciences
Victoria University Wellington
2016

Contents

List of Figures

List of Tables

Acknowledgements

I would like to begin by thanking my marvellous supervisors Helen Bostock and Lionel Carter, for supporting me through the past year and helping keep me (and my project) on track. Helen you have been amazing, ensuring I don't get too side tracked by miniscule aspects of my project and being available to discuss any queries I had about my data. I am not sure how you did all this as a new mother. And Lionel, you have been vital in the interpretation of ongoing oceanographic processes at my study site and I really appreciate your prompt return of all my chapters, particularly when it came close to crunch time. Both of you were very helpful, friendly and approachable and I really enjoyed working with you.

I am extremely grateful to AINSE who provided the research grant and facilities to run radiocarbon dates and ITRAX analysis at ANSTO in Australia. A special thankyou must go to Patricia Gadd who took me under her wing at ANSTO and prepared all ITRAX data for analysis, and Geraldine Jacobsen and Vladimir Levchenko for their work developing radiocarbon dates. I would also like to thank Ian Schipper (VUW) for his work on the electron microprobe, Jamie Howarth (GNS) for his help developing and running OxCal age models and Helen Neil and Colin Nankivell for stable isotope analysis.

A special shout out has to go out to the NIWA staff who were both accommodating and welcoming to a new masters student in their midst. I really enjoyed all the lunch time sporting opportunities and am impressed with the enthusiasm in many of these players. I don't think I have ever run as much as I did in ultimate frisbee and I am sure we can all remember winning the dodgeball tournament fondly. I would also like to thank the geology department for including me in their staff functions and multiple dress-up opportunities. Watching you all run around in glittery ~~capes~~ wings with giant mosquito headgear will be a memory I won't soon forget.

A special thankyou has to go to Lisa Northcote for all her help setting up and running experiments in the lab. You were always friendly and helpful, and made working in the lab fun. I would also like to thank Susi Woelz for sharing her office space. It was nice to have someone to talk to when the thesis got a bit repetitive and I am amazed that you were so accommodating when it got to the editing stage and I began sighing a lot and whispering to myself.

To the ten thirty crew: You are all rad. Morning coffee breaks were the highlight of many of my days and I will miss you all terribly. I am amazed that there was so much to talk about when we saw each other, sometimes multiples times, every day. And to the flat: Frances, Matt and Ben, you guys have been champs throughout these final weeks and I really appreciate all the support you have given. I couldn't ask for better flat mates. I would also like to take this opportunity to thank members of the proof reading party. There ain't no party like a proof reading party. Just kidding, we never said that. Helping with the last push may have made the difference between handing in a completed thesis and having a smashed lap top, and I would like to take this opportunity to thank you all for keeping me smiling.

And finally to my family, particularly Api who was the most sympathetic, we would totally be friends even if we weren't related. Thanks for all your support throughout these MANY long years of study. Ron I want to thank you for listening to me ramble on about my study even if you weren't that interested. Wanda I want to thank you for always being happy when I was coming home to visit and ensuring I got all my favourite meals which I cannot afford on a student budget. Max thanks for coming to visit so often. It is always exciting when you come down as it means a weekend of adventures and activities, and I know I can rely on you to communicate properly and stick to your plan. And finally Api. My little study buddy. You always make things interesting and I wish you all the best of luck with your thesis over the coming year.

Abstract

Marine Isotope Stage 3 (MIS3) is an important period in the Earth's climate history as it contains a series of millennial scale events. These can be reconstructed to help interpret the response of the Earths ocean/climate system to rapid climate events and this may have important connotations for the Earth's system response under anthropogenically induced climate change. During MIS3, millennial scale events in the Antarctic ice core record occur out of phase with millennial scale events in the Greenland ice core record. Antarctic millennial scale events are defined peaks in $\delta^{18}O$ and are known as Antarctic Isotope Maxima (AIM) events. These events have been recorded in high-resolution marine sediment records in the Southern Ocean, but there is sparse literature at a high enough resolution to extract the millennial scale signal from marine cores in the SW Pacific during MIS3.

This study developed high-resolution marine sediment records in the New Zealand region from cores TAN1106-28, collected in the Solander Trough region south of New Zealand, and MD97-2121, collected off the east coast of Hawkes Bay, to reconstruct millennial scale variability in the SW Pacific during MIS3. Productivity and terrestrial mass accumulation rates (MAR) were combined with stable isotopes and ITRAX XRF analysis to reconstruct ocean/climate variability during MIS3 and identify AIM events. ITRAX XRF produced high-resolution (1 mm scale) elemental proxy data which showed a high correlation coefficient between ITRAX Ca, and $CaCO_3$ % calculated using the vacuum gasometic procedure. This suggested that ITRAX XRF accurately represented elemental variations in these marine sediment cores, and that it may be a valuable tool for high-resolution climate reconstruction. ITRAX XRF was also used to identify the Rotoehu, Tahuna and Kawakawa cryptotephra in MD97-2121. However, this analysis was only moderately successful as ITRAX elemental proxies showed multiple cryptotephra events. Samples which contained these events then had to be classified as a cryptotephra deposit using a binocular microscope, and identified as a specific tephra eruption through electron microprobe analysis.

MIS3 reconstructions for TAN1106-28 show AIM events in both productivity fluctuations and terrestrial sedimentary input. Productivity at the site of TAN1106-28 increased during AIM events and this is consistent with findings from marine sediment cores throughout the Southern Ocean. In the New Zealand region increased productivity during AIM events was inferred to be a response to the increased availability of light or warmer sea surface temperatures, as iron decreased during AIM events, suggesting productivity was not driven by iron fertilisation. The decrease in iron and other terrigenous proxies likely reflects increased glacial erosion during the stadial phase of Antarctic millennial scale events as recorded in the onshore record during the Antarctic Cold Reversal. Overriding these millennial scale fluctuations was an increase in terrigenous accumulation heading into the MIS2 glaciation.

Like TAN1106-28, sediment accumulation increased at the site of MD97-2121 heading into the MIS2 glacial. This suggests that eustatic sea level variations have a strong control on terrestrial accumulation in the wider New Zealand region. Unlike TAN1106-28 however, there is little evidence for AIM events in MD97-2121 to the north of the front, strongly suggests the STF acts

as a boundary to the AIM signal, restricting northward movement of the signal in the Southern Hemisphere mid latitudes.

1 Introduction

Marine Isotope Stage 3 (MIS3) spans from 57 to 29 ka (Lisiecki and Raymo, 2005) and contains a series of periodically spaced, short term climate events (Figure 1.0.1). These events occur on a millennial timescale and show temperature changes of $< 16.5 \pm 3°C$ in compiled Greenland ice core records (Kindler et al., 2014) and $1 - 3°C$ in the Siple Dome, Antarctic ice core record (Ahn and Brook, 2014). Millennial scale climate events are not restricted to MIS3, but this is the period which shows the greatest regularity in the timing of these events (Buizert and Schmittner, 2015; Schulz, 2002)(Figure 1.0.1), and therefore is an ideal period to analyse to better determine the timing, magnitude and extent of rapid climate change events. Considering the complications and hazards associated with anthropogenic induced climate change, a greater understanding of the processes and responses which drive MIS3's rapid climate change events.

A considerable amount of information is available about climate variability during MIS3 in the Northern Hemisphere and Antarctica, but there is significantly less published literature which focuses on MIS3 in the Southern Hemisphere marine sediment record. This knowledge gap is been addressed by SHAPE (Southern Hemisphere Assessment of Paleo-Environments), a collaborative project whose primary objective is to develop high-resolution records in the Southern Hemisphere from 60 ka, the limit of radiocarbon dating, to the present. The SHAPE project is using proxy data from ice, marine sediment cores, and terrestrial records, and comparing them with model outputs to establish possible drivers of climate change and build a comprehensive representation of spatial variability during the last 60 ka.

High-resolution marine records in the Southern Ocean have been developed for the South Atlantic (e.g. Barker et al. 2009), South Indian (e.g. Sicre et al. 2005), and SE Pacific (e.g. Caniupán et al. 2011) Oceans. However, there are limited records at a high enough resolution from the SW Pacific to extract rapid climate events during MIS3 and tease out the Northern or Southern Hemisphere driving mechanisms behind them.

New Zealand is located in the SW Pacific, between subtropical waters (STW) to the north, and subantarctic waters (SAW) to the south. By analysing high-resolution marine sediment core records in this region, a more comprehensive understanding about how Antarctic and tropical climate signals influence ocean/atmosphere processes at this site will be developed. These records will then be compared with the New Zealand terrestrial record, the compiled Antarctic ice core record (CAICR)(Pedro pers comm.), and other Southern Ocean marine sediment records, to provide information on the Southern Hemisphere oceanic response to millennial scale events during MIS3 and contribute to the SHAPE project.

The separation of SAW and STW in the New Zealand region occurs across the Subtropical Front (STF). In the New Zealand region the STF is a narrow, well defined frontal system (Smith et al., 2013). It flows around southern New Zealand as the Southland Current (SC) and eastward along the Chatham Rise where is meets the STW introduced to the New Zealand region via the Tasman Front (TF) (Sikes et al., 2002a; Smith et al., 2013). Comparison between marine sediment cores

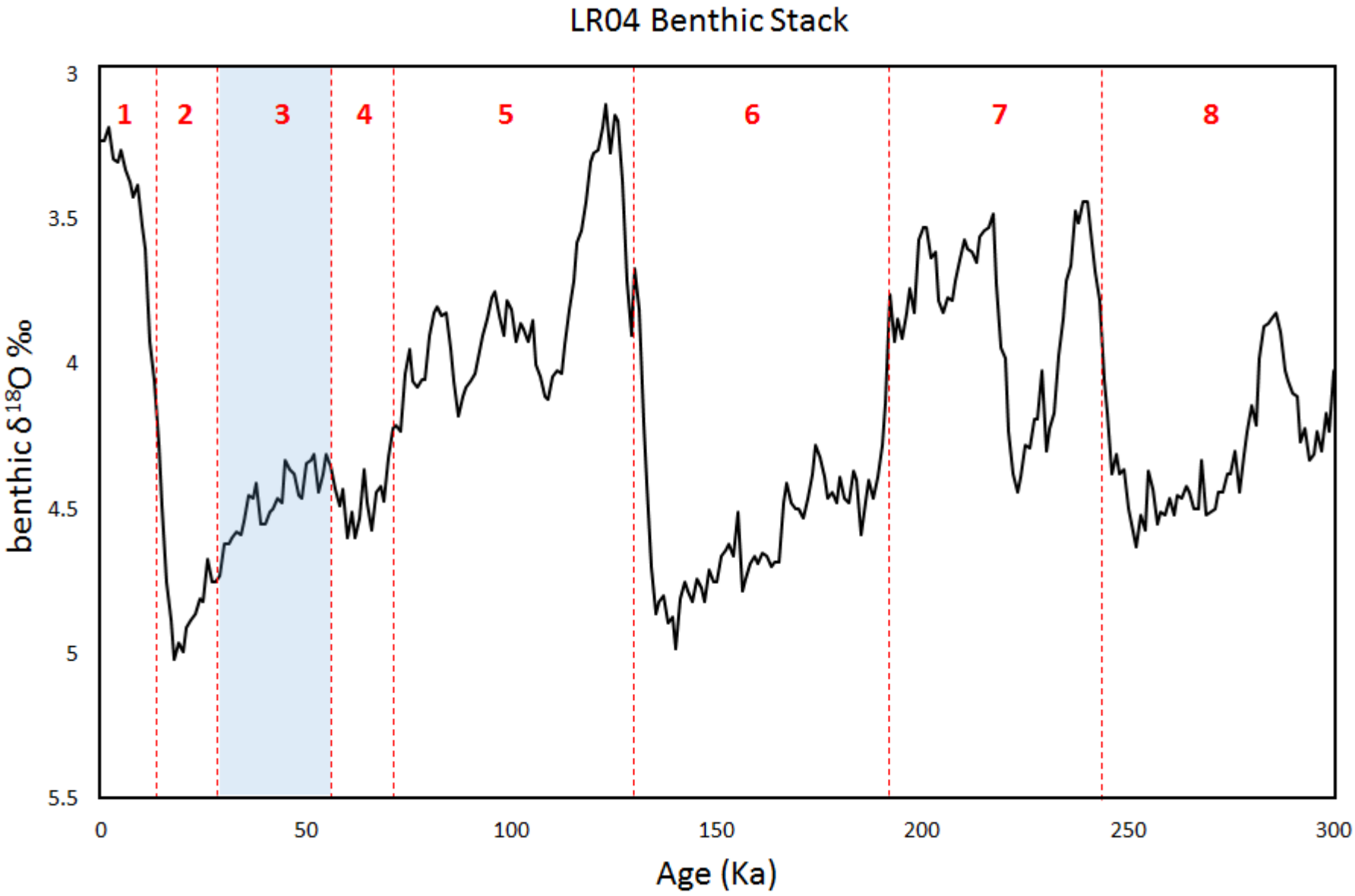

Figure 1.0.1: LR04 Benthic δ^{18}O Stack from Lisiecki and Raymo (2005). Dashed lines show the transitions between Marine Isotope Stages which are numbered in red and the blue shaded area shows MIS3

TAN1106-28 to the south of the front, and MD97-2121 to the north, will therefore show the extent to which the STF acts as a boundary to Antarctic millennial scale events, and the buffering capacity of STW at the site of MD97-2121.

To analyse MIS3 millennial scale events at the site of TAN1106-28 and MD97-2121, traditional methods such as $\delta^{18}O$, $CaCO_3$ %, grainsize analysis and radiocarbon dating were utilised, along with newly developed ITRAX techniques. ITRAX is a high-resolution (mm scale) analytical technique that has been sparsely used in published literature on Southern Hemisphere marine sediment cores (expanded in Section 4.6). Elemental proxy data from ITRAX X-ray fluorescence (XRF) were used to identify rhyolitic cryptotephra in MD97-2121, and reconstruct biological productivity and terrigenous variability in both cores. This allowed the analysis of variations in biological productivity and terrestrial sediment influx to be evaluated.

1.1 Thesis Aims

The primary objectives of this thesis are to:

- Generate high-resolution paleoceanographic records for MIS3 in the SW Pacific and identify millennial scale ocean/climate events during MIS3,
- Identify cryptotephra deposits in MD97-2121 using newly developed ITRAX techniques and
- Compare evidence for changes in oceanic conditions, including temperature and productivity, with ice core records, the New Zealand terrestrial record and other marine sediment records to establish the extent to which the STF acts as a boundary to the Antarctic climate signal.

2 Marine Isotope Stage 3 (MIS3)

The cool climate conditions of MIS3 are reflected in the δ^{18}O values which range from 4.72 to 4.31‰ in the LR04 benthic stack, and show a heavier signature heading towards the MIS2 glaciation reflecting the transition to cooler climate conditions (Figure 1.0.1). Heavier δ^{18}O values also reflect lower eustatic sea levels, and this is confirmed by coral reef sea level reconstructions which suggest sea levels were 60 m below present at the beginning of MIS3 and lowered to 80 m below present half way through the interstadial and importantly, concluded that sea level changes reflected ice loss/gain in Antarctica (Siddall et al., 2008).

2.1 Millennial Scale Events

MIS3 also contains several millennial scale events. These are defined by abrupt changes in δ^{18}O‰ (Figure 1.0.1) reflecting transitions between cool stadial and warmer interstadial conditions in both Greenland (Section 2.1.1) and Antarctic (Section 2.1.3) ice core records.

2.1.1 Dansgaard-Oeschger events

Millennial scale events during MIS3 were identified in the Greenland ice core record by Dansgaard et al. (1983). These events have been termed Dansgaard-Oeschger (D-O) events and display a distinct saw tooth pattern, caused by a rapid, decadal warming $< 16.5 \pm 3$°C (Kindler et al., 2014), followed by a centennial cooling back to stadial conditions (Huber et al., 2006). To allow for ready identification and comparison between events, each D-O event is associated with a number. This begins with D-O event 1 and increases numerically with age (Figure 2.1.1).

2.1.2 Heinrich events

During the coolest D-O events, distinct, short lived, cool climate periods known as Heinrich events occurred. These events took place less frequently than D-O events (Figure 2.1.1) and are distinguished through evidence of massive ice berg discharge into the North Atlantic (Huber et al., 2006). These events have been recorded in multiple North Atlantic marine sediment cores as wide-spread layers of ice-rafted debris (IRD) (Heinrich, 1988) which can be traced for over 3000km (Bond et al., 1992). IRD forms due to the discharge of coarse grained terrigenous sediment from the bottom of ice bergs. This terrigenous sediment is eroded from the glacial bed and frozen into glacial ice to be released as the ice berg melts. Marine sediment with such deposits therefore suggests the presence of ice bergs over these core sites (Dowdeswell, 2009). However, this record needs to be interpreted with care as IRD can result from changing oceanic conditions, or changing ocean temperatures, the mechanics of which are still not fully understood (Hemming, 2004). In terms of Heinrich events, IRD layers are thought to reflect both a massive increase in ice berg discharge, though the source of these ice bergs is contentious (Álvarez-Solas et al., 2011; Hemming, 2004; Hulbe et al., 2004), and an equatorward expansion of cold polar waters (Bond et al., 1992).

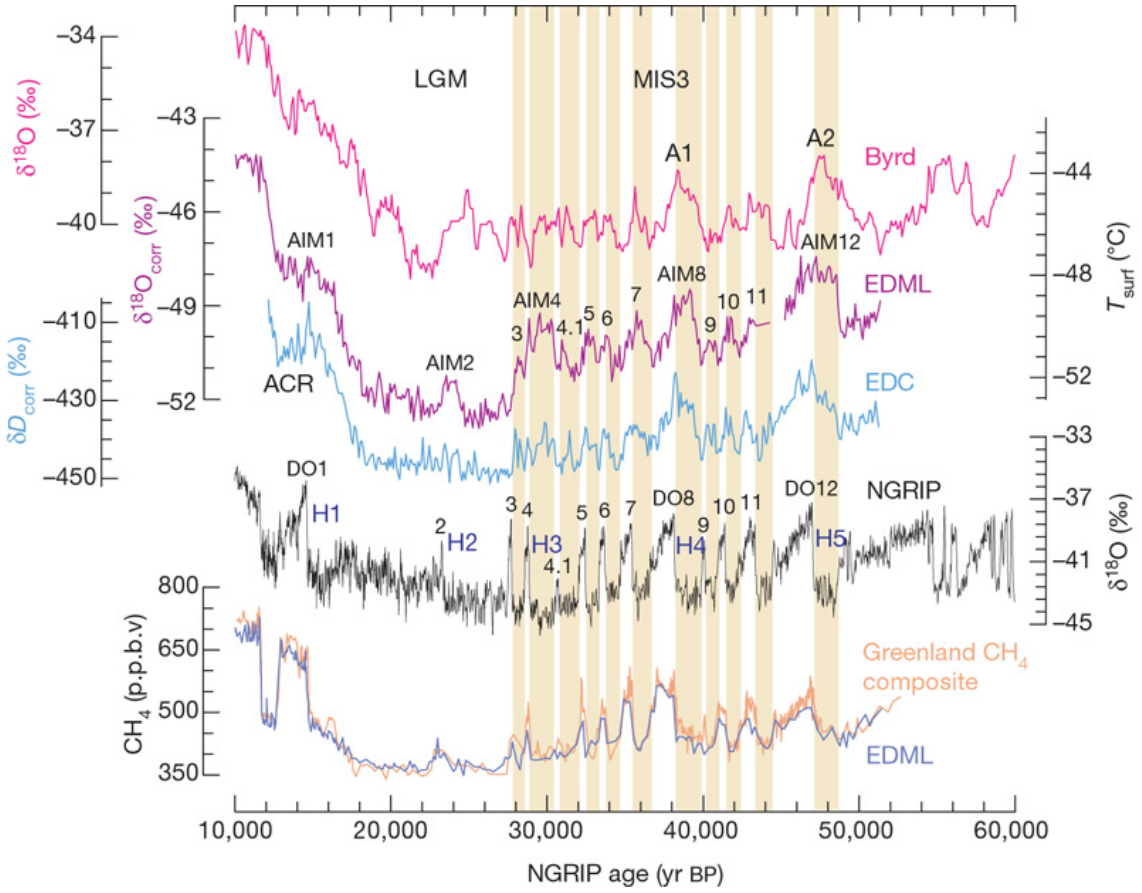

Figure 2.1.1: Figure taken from EPICA community members (2006). Displayed are 100-yr averages during MIS3 in the Antarctic ice cores, EDML, EDC and Byrd ice cores for the time interval 10-60 kyr BP in comparison with the NGRIP δ^{18}O record from northern Greenland. All records are CH_4 synchronized and given on the GICC05 age scale for the NGRIP ice core, which has been derived by counting annual layers down to 41 kyr and by a flow model for older ages (Andersen et al., 2004, 2006). Yellow bars indicate the Greenland stadial periods that EPICA community members (2006) relate to respective Antarctic temperature increases. The approximate timing of Heinrich layers in North Atlantic sediments are annotated with an H and their event number. DO and AIM events are similarly labelled. The y axis on the right side indicates approximate temperature changes at EDML based on the modern spatial gradient between δ^{18}O and temperature.

2.1.3 Antarctic Isotope Maxima (AIM) events

Millennial scale events in the Antarctic ice core record are known as Antarctic Isotope Maxima (AIM) events. During AIM events $\delta^{18}O$ ‰lightens, reflecting warming events over the Antarctic continent. AIM events are shorter in duration and show less drastic climate change than Greenland D-O events (Figure 2.1.1) with atmospheric temperatures in Antarctica varying by 1-3°C across AIM events (Ahn and Brook, 2014; Watanabe et al., 2003), and temperatures in Greenland varying by < 16.5°C during D-O events. Although these events are well preserved in ice core records in Antarctica, there are still gaps in the Southern Ocean marine sediment record. This is particularly evident in the SW Pacific where there is no data of a sufficient resolution to accurately recognise AIM or D-O events.

2.2 Drivers

There is little consensus surrounding the mechanisms which drive millennial scale climate events. Theories have arisen around solar forcing (Braun et al., 2008), due to a proposed 1470 year periodicity of D-O oscillations (Rahmstorf, 2003; Schulz, 2002); and/or variable internal mechanisms (Siddall et al., 2008) such as sea ice extent (Li et al., 2005), or internal ice sheet dynamics (Timmermann et al., 2003).

2.2.1 Bipolar Seesaw

General consensus has, however, been reached about the mechanism which transfers millennial scale climate events between the two hemispheres. High-resolution correlation between Greenland and Antarctic ice core records using global atmospheric changes in CH_4 showed that D-O events occur out of phase with AIM events (Blunier and Brook, 2001; Blunier et al., 1998; EPICA community members, 2006; Zhang et al., 2014), with Antarctic warming preceding its respective Northern Hemisphere D-O event (Figure 2.1.1)(Blunier and Brook, 2001). This out of phase relationship is known as the bipolar seesaw (Broecker, 1998), and as the transfer of climate signals by the atmosphere occurs rapidly (≈ 1 year between hemispheres (Blunier and Brook, 2001)), the lag time of the Greenland D-O event means the climate signal must be transferred via ocean circulation patterns. The Atlantic Meridional Overturning Circulation (AMOC) links the Southern and Northern Hemispheres via the transport of water masses between the Southern Ocean, and the North Atlantic, Pacific and Indian Oceans. The northern branch contains productive surface waters which sink, due to a density and temperature contrast, and are transported south (Talley, 2013). As these deep waters move southwards they upwell in the Southern Ocean releasing heat, nutrients and CO_2 (d'Orgeville et al., 2010; Sigman et al., 2010; Toggweiler et al., 2006).

During Greenland stadials the AMOC shuts down, or is severely reduced, due to freshwater perturbations from the Northern Hemisphere ice sheets (Timmermann et al., 2003). A weakening of the AMOC reduces the northward movement of warm waters resulting in cooler temperatures over Greenland, and a warming of the South Atlantic. When convection is renewed at the beginning of the interstadial, these climate conditions are reversed and heat is drawn away from the Southern Ocean towards the North Atlantic (Rasmussen et al., 2016; EPICA community members, 2006; Stocker and Johnsen, 2003). While, the AMOC is generally accepted as the mechanism behind the bipolar seesaw, there is little consensus on the underlying processes which may have affected AMOC variability, how they interacted with each other, and whether they are initiated in the Northern or Southern Hemisphere (Leduc et al., 2009; Rasmussen et al., 2016), although it has

been suggested that enhanced bottom water transport in the Southern Ocean may be necessary to account for surface water heat transport and CO_2 ventilation during AIM events.

2.3 Southern Ocean

Antarctic ice core records show that during AIM events atmospheric CO_2 levels increased by 20-30 ppmv in phase with Antarctic temperature records (Figure 2.3.1), although this lags by 870 $\pm$90 years during MIS3 (Bereiter et al., 2012). The understanding of mechanisms behind this relationship is constantly evolving but, it is likely that a considerable source of atmospheric CO_2 was provided via ventilation of the Southern Ocean during MIS3 (Fischer et al., 2010; Martinez-Garcia et al., 2009; Toggweiler et al., 2006). There is no direct proxy for atmospheric CO_2 in Southern Ocean marine sediment cores. However, CO_2 ventilation in the Southern Ocean has been inferred using opal fluxes in the marine sediment, and the isotopic composition of gas bubbles in the Antarctic ice core records (d'Orgeville et al., 2010). These proxies have allowed the reconstruction of Southern Ocean ventilation during the abrupt climate events of MIS3.

Enhanced ventilation of the Southern Ocean is the result of reduced sea ice extent, a weakening of ocean stratification, changes in Southern Ocean productivity (though this is thought to be negligible (Fischer et al., 2010; Martinez-Garcia et al., 2009)), and increased strength of the westerly wind belt (d'Orgeville et al., 2010; Fischer et al., 2010; Martinez-Garcia et al., 2009; Gildor et al., 2002). It is therefore likely that during MIS3, one or more of these processes was helping contribute to the changes in the Southern Ocean ventilation of CO_2 during AIM events.

The breakdown of the AMOC during AIM events causes warmer waters to migrate south (Rasmussen et al., 2016; EPICA community members, 2006; Stocker and Johnsen, 2003). This results in less sea ice and an enhanced temperature gradient over the Southern Ocean which increases westerly wind strength (Lamy et al., 2004). The reduction in sea-ice increases the air-sea exchange of CO_2 (Ziegler et al., 2013), and enhanced westerly winds drive upwelling, releasing CO_2 from the deep ocean into the atmosphere (d'Orgeville et al., 2010; Toggweiler et al., 2006) and resulting in increased atmospheric CO_2 during AIM events. In contrast, during Greenland interstadials these processes reverse and CO_2 remains sequestered in the sub-surface Southern Ocean due to a decline in wind strength, increased sea ice extent and enhanced ocean stratification (d'Orgeville et al., 2010; Toggweiler et al., 2006).

2.4 Biological productivity

Biological productivity in the Southern Ocean also shows AIM variability during MIS3 (Sachs and Anderson, 2005). Surface water productivity is controlled by light, temperature, and the availability of macronutrients (nitrate and phosphate) and micronutrients, the most prominent of which is iron. When these conditions are favourable, surface water productivity increases, drawing down CO_2 from the atmosphere and allowing it to be sequestered in the deep ocean in a process known as the biological pump (Sigman et al., 2010; Toggweiler et al., 2006). In high macronutrient but low chlorophyll (HNLC) waters, such as the Southern Ocean, productivity is limited by a lack of iron (Maldonado et al., 2005; Martin, 1990). The iron fertilisation hypothesis (Martin, 1990) proposes that increased dust input during glacial conditions increases surface productivity which draws down atmospheric CO_2 and sequesters it in the deep ocean. However, this has since been

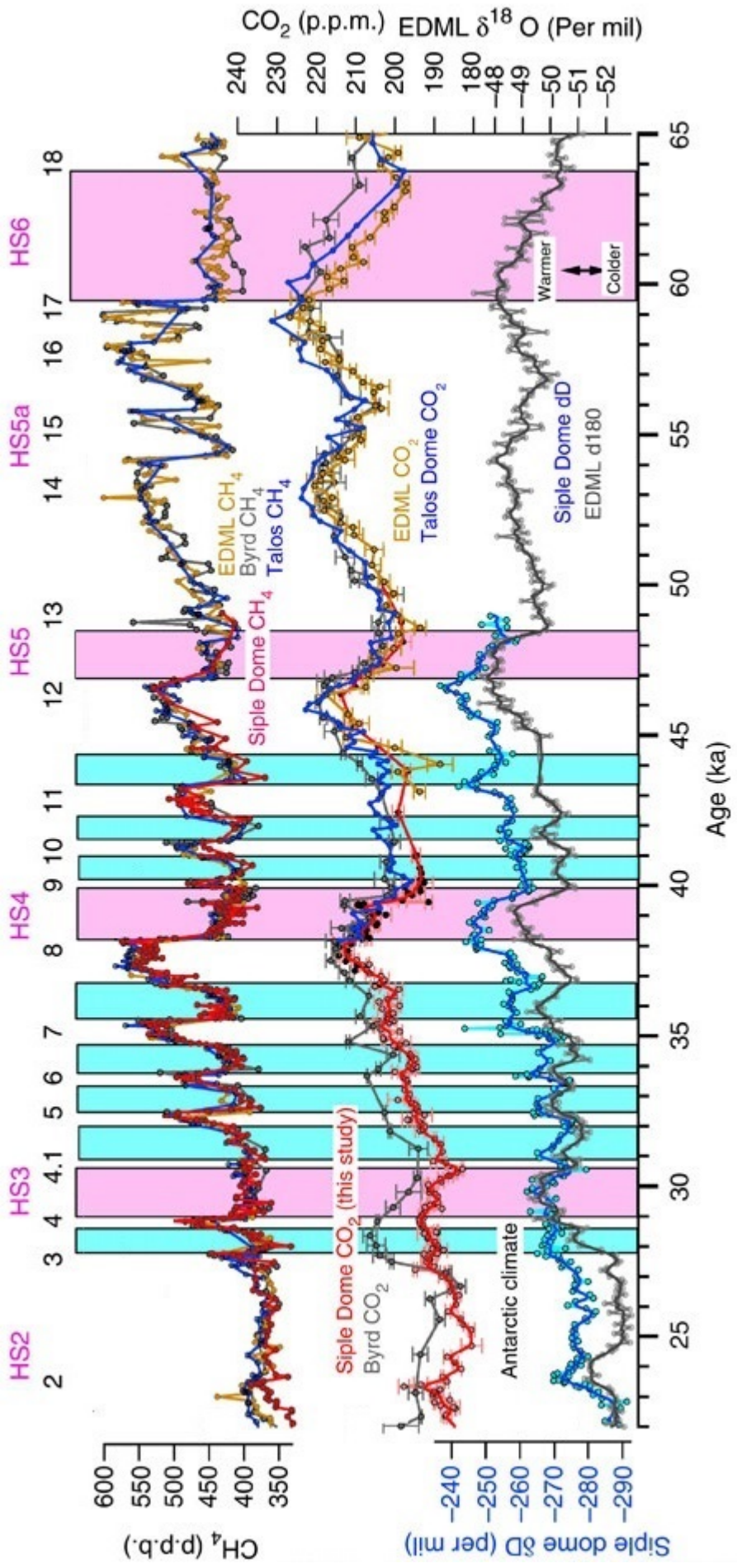

Figure 2.3.1: Comparison between atmospheric CO_2 and Antarctic climate records from Ahn and Brook (2014)

contested (Boyd et al., 2000), in part because changes in biological productivity cannot explain the full extent of atmospheric CO_2 variability between glacial and interglacial conditions (Martinez-Garcia et al., 2009; Kohfeld et al., 2005), and only account for an estimated 5-10 ppmv of the millennial CO_2 changes during MIS3 (Fischer et al., 2010). Increased dust input into the Southern Ocean therefore may result in an increase in primary productivity but, this cannot account for all CO_2 variation.

During MIS3 cold Antarctic events, the westerly wind belt moved north, blowing dust from the continents into the Southern Ocean. In the Atlantic and Indian sectors of the Southern Ocean this dust is sourced from Patagonia, but in the SW Pacific, aeolian dust is supplied from Australia and/or New Zealand (Lamy et al., 2014). The timing of these high dust input events is synchronous in all cores across the Southern Ocean, suggesting they likely derive from the same event. However, the relationship between dust input events, productivity, and CO_2 drawdown on millennial time-scales needs to be further developed in the Southern Ocean (Lamy et al., 2014; Ziegler et al., 2013).

2.5 Tropics and subtropics

Millennial scale climate events are also recognised in terrestrial and marine sediment records in the tropics (Dannenmann et al., 2003; Huang and Tian, 2012; Leduc et al., 2009; Saikku et al., 2009; Stott et al., 2002; Wang et al., 2001). Tropical climate systems such as the East Asian Monsoon (EAM), the Intertropical Convergence Zone (ITCZ), and the West Pacific Warm Pool (WPWP) show a strong coupling to climate conditions in the northern high latitudes during MIS3 (Huang and Tian, 2012; Leduc et al., 2009; Stott et al., 2002; Wang et al., 2001). During Northern Hemisphere interstadials, the EAM becomes more dominant (Huang and Tian, 2012; Wang et al., 2001), the ITCZ intensifies (Stott et al., 2002) and shifts north (Leduc et al., 2009), and the WPWP has lowered salinity levels (Stott et al., 2002) showing the influence of the Northern Hemisphere climate system. However, some climate proxies in the tropics also vary in phase with the Antarctic signal (Dürkop et al., 2008; Saikku et al., 2009).

The tropical West Pacific contains a bipolar signal, with sea surface temperature (SST) proxies showing variations that are in phase with D-O events, and benthic $\delta^{18}O$ showing variations in phase with AIM events (Dürkop et al., 2008; Saikku et al., 2009). The transfer of the Northern Hemisphere signal is attributed to atmospheric teleconnections via a coupling of the Australian and EAM systems (Dürkop et al., 2008), or a southward displacement of the ITCZ during the Greenland stadial in response to steeper meridional temperature gradients within the Pacific (Saikku et al., 2009). Further, the correlation with Antarctic atmospheric temperatures in the benthic $\delta^{18}O$ signal is thought to reflect variations in Southern Ocean temperatures at Pacific deep water formation zones (Saikku et al., 2009), or a surface migration of the West Australian Current (Dürkop et al., 2008). As similar results are found in the North Atlantic at core MD95-2042 off the Portuguese coast (Shackleton et al., 2000) this suggests that this is not a regional response and that both Antarctic and Greenland climate signals are experienced in the tropics during MIS3.

2.6 Summary of MIS3

MIS3 contains $\delta^{18}O$ values that are considerably heavier than interglacials of the Late Quaternary (Figure 1.0.1) (Lisiecki and Raymo, 2005) reflecting cooler temperatures and lower sea levels.

MIS3 also contains a complex system of millennial scale events. In Greenland ice core records, these events are known as D-O events and show air temperature changes of up to 16±3°C on a decadal timescale (Kindler et al., 2014; Huber et al., 2006). D-O events occur out of phase with AIM events in a relationship known as the bipolar seesaw which is thought to be driven by variations in the strength of the AMOC (EPICA community members, 2006).

In Antarctica, MIS3 contains AIM events 12-3 (EPICA community members, 2006). These events are lower magnitude climate change events in comparison with the corresponding Northern Hemisphere D-O events, with 1-3 °C change in air temperature (Ahn and Brook, 2014; Watanabe et al., 2003), and are experienced throughout the Southern Ocean (Barker et al., 2009; Caniupán et al., 2011; Dannenmann et al., 2003; Sicre et al., 2005) and in the deep water signal in the tropics (Dürkop et al., 2008; Saikku et al., 2009). Temperature changes during AIM events occur in conjunction with increases in CO_2 (Ahn and Brook, 2014; Bereiter et al., 2012; Lamy et al., 2004) and this is thought to relate to changes in biological productivity, upwelling and ventilation in the Southern Ocean (d'Orgeville et al., 2010; Toggweiler et al., 2006).

3 Regional Setting

Development of high-resolution marine sediment records in the SW Pacific will show how this region responds to rapid climate change events. However, in order to extract the Antarctic climate signal during MIS3, marine sediment cores first need to be assessed within the context of the ongoing oceanic processes and terrestrial variability at these core locations.

3.1 Oceanography

As New Zealand is located between STW to the north and SAW to the south, it is subject to both tropical and polar ocean/climate influences. Subtropical and SAW have different properties and are separated by the STF (Figure 3.1.1), a mid latitude frontal system which helps regulate the transfer of heat, salt and nutrients between subtropical gyres to the north, and the Southern Ocean in the south (Smith et al., 2013).

3.1.1 The Subtropical Front

The STF is considered to define the northernmost extent of the Southern Ocean (Bostock et al. 2015 and references therein). In general, it is a 400-500 km wide zone (Smith et al., 2013) which, barring the South American section, extends around the Southern Hemisphere at $\approx 40°$S (Belkin and Gordon, 1996; Orsi et al., 1995) and acts as a boundary between warm, saline, subtropical surface waters to the north, and cool, fresh, SAW to the south (Belkin and Gordon, 1996; Orsi et al., 1995). Off southernmost New Zealand, the STF has a vertical reach of $\approx$ 500 m (Smith et al., 2013) and a temperature gradient of $4 - 5°$C over $1°$ latitude. This temperature gradient likely increased slightly in MIS3 to $\approx 6°$C as subpolar waters cooled more than STW (Sikes et al., 2002b). Salinity and nutrient levels also vary across the front, with a salinity gradient of ≈ 0.7 (Bostock et al. 2015 and references therein), and a nutrient gradient between micronutrient rich STW to the north and macronuterient rich, but Fe limited SAW to the south (Schaefer et al. 2005 and references therein). Mixing between these two bodies of water creates a zone of high biological productivity over the front (Chiswell et al., 2013).

The STF has recently been identified as a double frontal structure, containing both a North-Subtropical Front (N-STF) and a South-Subtropical Front (S-STF) (Bostock et al. 2015 and references therein). The N-STF is a shallow frontal system which marks the northern limit of SAW while the deeper S-STF defines the southernmost extent of subsurface STW (Hamilton, 2006).

In the New Zealand region, the modern STF enters from the Tasman Sea in the west. It runs along the south-west coast of the South Island following the 500m isobath and crosses the Macquarie ridge and Solander Trough at 49°S (Sikes et al., 2002a; Smith et al., 2013). The front then turns equatorward and continues up the east coast of the South Island as the Southland Current (SC). The SC is SAW dominated and transports 8.3 Sv (Sutton, 2003) up the south-east coast of the South Island until it hits the Chatham Rise. Here the SC interacts with STW and other coastal currents reforming the STF and continuing east.

3.1.2 Sub-Antarctic Front (SAF)

The SAF is the northern boundary of the Antarctic Circumpolar Current (ACC), an unbroken current system which circles Antarctica (Orsi et al., 1995) containing strong currents, and enhanced temperature, and salinity gradients (Stanton and Morris, 2004). In the New Zealand region, the SAF is topographically steered by bathymetry (Chiswell et al., 2015). It enters the southern New Zealand waters from the west and is bathymetically forced through the Macquarie Ridge (in the vicinity of TAN1106-28) and around the south-eastern side of the Campbell Plateau before continuing eastward, adjacent to the STF, off the southern flank of the Chatham Rise (Heath, 1981; Stanton and Morris, 2004)(Figure 3.1.1).

3.1.3 East Coast currents

At the site of MD97-2121, there are three oceanic circulation systems. These are the East Cape Current (ECC), the Wairarapa Eddy, and the Wairarapa Coastal Current (WCC) (Figure 3.1.1).

- The ECC is a distant branch of the East Australian Current, the western boundary current of the South Pacific subtropical Gyre (Tilburg et al., 2001). This current is comprised of warm, high salinity subtropical water which comes into the New Zealand region via the Tasman Front (TF)(Carter et al., 2002). The TF transports the bulk of STW to the New Zealand region (Chiswell et al., 2015) and has a mean modern transport of 7.8 Sv (Sutton and Bowen, 2014). The TF reaches the top of northern New Zealand forming the East Auckland Current (EAUC) which flows down the north-east face of the North Island to become the ECC as it flows around the East Cape. The ECC transports 5-10 Sv of subtropical waters southwards along eastern New Zealand over the site of MD97-2121, before being deflected along the northern side of the Chatham Rise (Figure 3.1.1).
- A significant portion of ECC water remains entrained in the western and southern edge of the Wairarapa Eddy, a quasi-stationary anticyclonic eddy which is located off south-eastern New Zealand.
- The WCC transports 1.6 Sv (Chiswell et al., 2015) of cool, low salinity SAW, and modified STW from the d'Urville and Southland currents, up the east coast of the North Island. This water then becomes entrained into the ECC past northern Hawkes Bay (Chiswell, 2000).

3.2 Marine Reservoir Age

To accurately date the timing of millennial scale events, it is important to construct an age model using significant tie points and a variety of techniques. The age model for cores TAN1106-28 and MD97-2121 was constructed through the use of radiocarbon, tephra, and the matching of $CaCO_3$ and Ca peaks in TAN1106-28 with the Compiled Antarctic Ice Core Record (CAICR) (Pedro pers comm.). However, to calibrate radiocarbon dates they need to first be corrected for variations in the marine reservoir age of radiocarbon at the core site. The marine radiocarbon curve (MARINE13) models the difference between atmospheric, and oceanic CO_2 uptake (Reimer et al., 2013). However, the reservoir age of CO_2 in the ocean varies in both time and space and this needs to be accounted for when analysing ^{14}C.

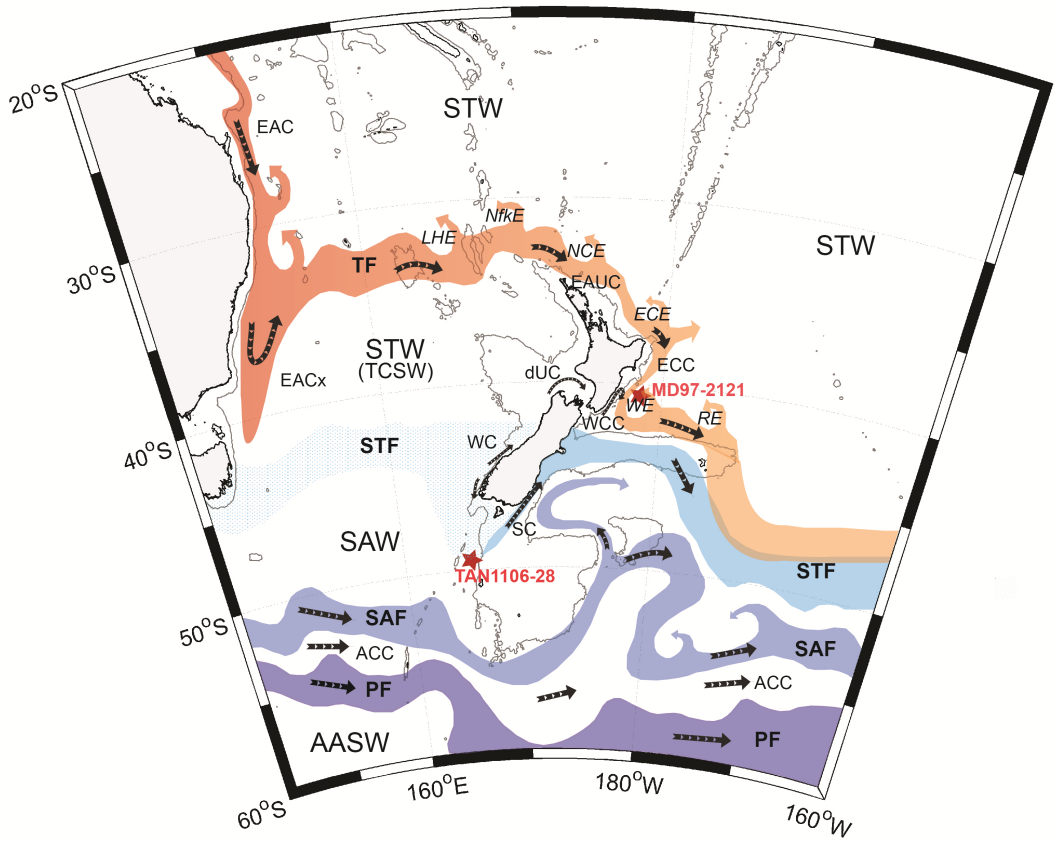

Figure 3.1.1: Ocean current systems in the New Zealand Region. Figure adapted from (Chiswell et al., 2015). The red stars mark core locations, with the southern star showing TAN1106-28 and the northern star MD97-2121. Ocean fronts around this region are: the Tasman Front (TF), the Subtropical Front (STF), the Subantarctic Front (SAF) and the Polar Front (PF) and contain arrows showing their flow direction. These fronts are also colour coded according to temperature with the warmer fonts shown in red and cooler fronts in blue. This map also shows local current systems, East Australian Current (EAC), East Australian Current extension (EACx), East Auckland Current (EAUC), East Cape Current (ECC), d'Urville Current (dUC), Wairarapa Coastal Current (WCC), Westland Current (WC), Southland Current (SC) and Antarctic Circumpolar Current (ACC). Eddies are Lord Howe Eddy (LHE), Norfolk Eddy (NfkE), North Cape Eddy (NCE), East Cape Eddy (ECE), Wairarapa Eddy (WE) and Rekohu Eddy (RE). Water Masses are Subtropical Water (STW), Tasman Sea Central Water (TSCW), Subantarctic Water (SAW) and Antarctic Surface Water (AASW).

Using tephra as stratigraphic tie points, marine sediment cores from the SW Pacific were used to reconstruct ^{14}C reservoir ages during the last glaciation (Sikes and Guilderson, 2016; Sikes et al., 2000; Skinner et al., 2015). These studies show that the surface reservoir age of ^{14}C in the ocean was elevated during the last glaciation in the SW Pacific. As MIS3 is characterised by a cooler climate, it is likely that this region was influenced by similar ocean/climate mechanisms to those driving ocean circulation during the last glaciation, albeit to a lesser extent. This suggests that during MIS3, the reservoir age of ^{14}C is likely to also be significantly older then the contemporary ^{14}C age. The reservoir age may vary within MIS3 as well due to the large ventilation changes behind the observed millennial scale variability, and this needs to be accounted for when calibrating radiocarbon ages.

The reservoir age of ^{14}C also varies between STW to the north, and SAW in the south (Sikes and Guilderson 2016 and references therein). There are sparse marine sediment cores in the immediate vicinity of TAN1106-28 which could be used to reconstruct the reservoir age of ^{14}C, mainly due to a lack of tephra tie points in this region. Therefore, the ^{14}C reservoir age needs to be interpolated from distal cores also located in SAW in the SW Pacific. Sikes and Guilderson (2016) reconstructed the marine reservoir age of ^{14}C during the last glaciation in cores south of the Chatham Rise (Figure 3.2.1). Although this is a considerable distance from TAN1106-28, these cores are located in SAW in the SW Pacific and therefore may reflect ^{14}C variation at the site of TAN1106-28. The surface marine reservoir age of ^{14}C at this site was $\approx$ 3200 $^{1}4C$ years, almost 5 times the modern surface reservoir age (400 years), and this was attributed to the upwelling of old deep waters from the abyssal Southern Ocean during the last glaciation (Sikes and Guilderson, 2016).

Cores used to reconstruct the subtropical surface water reservoir age were located in close proximity to the site of MD97-2121 (Firgure 3.2.1), and therefore are likely to accurately represent the ^{14}C reservoir age at that site. There reconstructions show that during the MIS2 glacial, the surface marine reservoir age of ^{14}C in subtropical waters was $\approx$ 700 years, 300 years older then the contemporary age (Sikes and Guilderson, 2016). This is significantly younger than the ^{14}C marine reservoir age reconstructed for SAW during the last glacial, and reflects an increased gradient between the surface reservoir age of subantarctic and subtropical surface waters. This increased ^{14}C gradient is likely due to the outcropping of old deep water in the Southern Ocean during the glaciation (Sikes and Guilderson, 2016).

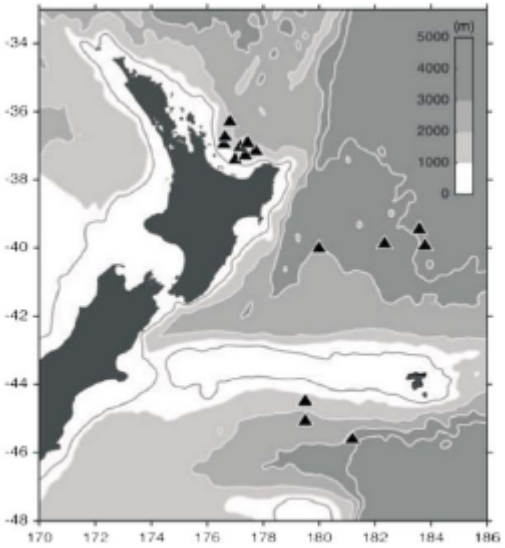

Figure 3.2.1: Location of cores used to reconstruct ^{14}C reservoir ages in subtropical and SAW during the last glacial in Sikes and Guilderson (2016). The black triangles show marine sediment core locations.

3.3 Reconstructing MIS3 in the New Zealand region

As there are limited high-resolution reconstructions of ocean/climate variability in the SW Pacific during MIS3, inferences need to be drawn from climate reconstructions during the MIS2 glacial and the short lived Younger Dryas cold event.

Reconstructions of the STF using paleotemperature estimates, show that it moved north by 3-5°during the last glacial to the south and west of New Zealand (Bostock et al., 2015; Kohfeld et al., 2013) (Figure 3.3.1). However, the bathymetric constraints of the Chatham Rise, and associated along-rise currents, act as a barrier, restricting northward movement of the front to the east of New Zealand (Bostock et al., 2015; Schaefer et al., 2005; Sikes et al., 2002b)(Figure 3.3.1). It is likely that a similar movement of the STF occurred during MIS3 and therefore, TAN1106-28 to the south of New Zealand (Section 4.1) was likely located in SAW, possibly close to the SAF (Bostock et al., 2015) during MIS3 (Figure 3.3.1) whereas, MD97-2121 likely remained in STW north of the STF (Figure 3.3.1).

Like the STF, the SAF is bathymetrically constrained and can not move from its position along the southern and eastern flanks of the Campbell Plateau during the glacial. However, a strengthening of the SAF during glacial conditions resulted in an enhanced supply of SAW through the Pukaki Saddle producing an enhanced temperature gradient ($< 6°C$) across the STF over the Chatham Rise (Neil et al., 2004). SAW likely continued north through the Mernoo Saddle to the site of MD97-2121 due to an intensification of the SC (Carter and Manighetti 2006 and references therein). It may have also been introduced to this site by the recirculation of SAW from the eastern end of the Chatham Rise, and it is likely that similar processes were operating, to a lesser extent, during MIS3.

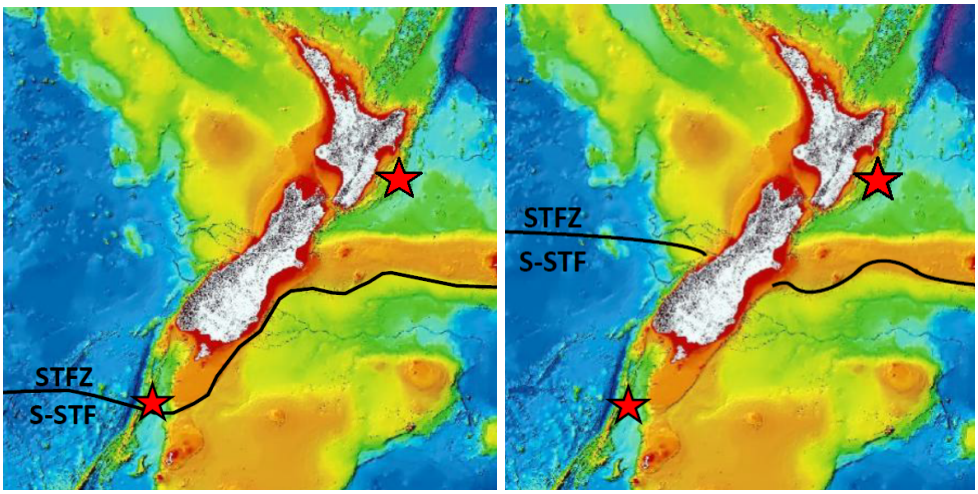

(a) Modern STF position (b) LGM STF position

Figure 3.3.1: Position of the Subtropical Front (STF) across New Zealand. The bathymetric image was revised from Mitchell et al. (2012) using STF positioning from Bostock et al. (2015). Figure (a) shows the modern STF location and Figure (b) shows the position of the STF during the Last Glacial Maximum (LGM). The southern star marks the location of TAN1106-28 and the northern star marks the location of MD97-2121. Cooler climate conditions during MIS3 likely caused a STF positioning similar to that of the LGM

As westerly winds in the Southern Hemisphere drive ocean circulation, northward movement of this wind belt may have been one of the mechanisms driving the STF and SAF north during the glacial (Kohfeld et al., 2013), and MIS3. Equatorward movement of the westerly wind belt may have also contributed to increased iron input in the Southern Ocean during cool climate events as movement of the wind belt over southern continents during dryer, cooler climates, likely increases the amount of aeolian dust transported into the ocean (Kohfeld et al., 2013).

TAN1106-28 has been previously analysed by Bostock et al. (2015) from the Last Glacial Maximum (LGM) to the Holocene. $CaCO_3$ %, Sea Surface Temperatures (SST) (derived from Modern Analytical Technique (MAT) applied to the Southern Ocean modern calibration foraminifera dataset SH0911), and $\delta^{18}O$ were used to reconstruct ocean/climate conditions over the upper metre of core (from $\approx$ 25 ka). These findings were used in conjunction with other marine sediment cores in a transect down the Solander Trough to reconstruct the position of the STF from the LGM to the present.

MD97-2121 has also been extensively analysed. However, like TAN1106-28 most analysis focused on the last 20 ka (Carter and Manighetti, 2006; Carter et al., 2008; Nelson et al., 2000; Pahnke and Sachs, 2006; Weaver et al., 1998). Carter and Manighetti (2006) and Pahnke and Sachs (2006), both analysed the entire 34.9 m (139 ka) record of MD97-2121 at a low resolution. Pahnke and Sachs (2006) used alkenone unstaturation ratios to develop SST estimates which showed a prominent warming towards the end of MIS3 from 47-23 ka, and Carter and Manighetti (2006) analysed terrigenous and biogenic Mass Accumulation Rates (MAR). During MIS3 terrigenous MARs varied with eustatic changes in sea level and biogenic carbonate MARs were reduced. This decline in marine productivity was attributed to a reduction in fluvialborne nutrients to the site of MD97-2121 as sediment was trapped on the shelf due to higher sea levels. Carter and Manighetti (2006)

also showed that biogenic and aeolian MAR profiles were out of phase. This suggested that dust induced iron fertilisation was not a major influence in this core.

In contrast, Carter et al. (2008) examined specific cold events, the Antarctic Cold Reversal (ACR) and the Younger Dryas in MD97-2121. These results showed a pause in the deglacial trend in the δ^{18}O benthic foraminfera signal during the ACR. This benthic response suggests the Antarctic signal was transferred via deep water circulation to the site of MD97-2121. Planktonic foraminifera δ^{18}O however, did not respond immediately to this event, reacting only when the ACR was at its coolest. The delay in the response of surface waters to this event was attributed to STW transported by the Tasman Front, which may have partially blocked some of this signal, and/or buffering by other tropical influences.

3.4 Geographic Setting

New Zealand sits astride the Pacific-Australian plate boundary. The Pacific plate subducts under the Australian plate in the Hikurangi Margin off the east coast of the North Island of New Zealand. This plate boundary extends south south-east through New Zealand as the transform Alpine Fault system, and continues past southern New Zealand as the Macquarie Ridge complex, a convergent plate boundary between the subducting Australian plate and the Pacific pate. This active tectonic region provides considerable uplift, seismic activity, and volcanism, which, when combined with New Zealand's high rainfall regime, makes this a system with high erosion rates (Pickering and Hiscott, 2015). These high erosion rates provide a considerable source of sediment to offshore New Zealand, which allows the development of high-resolution marine records.

TAN1106-28 was collected off southern New Zealand, to the west of Campbell Plateau in the Solander Trough region (Section 4.1 for site location and core collection details). The Solander Trough is a south south-west trending feature, extending from the bottom of the South Island to 52°S (Pickering and Hiscott, 2015). Marine sediment in the the Solander Trough region is hemipelagic, and predominantly comprised of terrigenous material discharged from the Southern Alps with sedimentation rates around 4-10cm/kyr (Bostock et al., 2015). This high terrigenous component contrasts with the more pelagic sediment of the neighbouring Campbell Plateau (Bostock et al., 2015).

MD97-2121 was collected to the north of the Chatham Rise, on the slope of a deep basin off southern Hawke's Bay (see Section 4.1 for more details about site location and core collection). This is a tectonically active region as the basin is located within an imbricate wedge in the Hikurangi Margin (Carter et al., 2002). Sediment deposited offshore of the east coast of the North Island of New Zealand is hemipelagic. However, like the site of TAN1106-28, it is comprised predominantly of terrigenous material. This is due to extremely high discharge levels from fluvial river systems, in particular the Waiapu, and Waipaoa rivers, with an average fluvial discharge of 80x10^6 t/yr of suspended load (Carter and Manighetti, 2006).

3.4.0.1 Volcanic activity

The close proximity of MD97-2121 to the Taupo Volcanic Zone has resulted in the deposition of multiple tephra layers, and these have been dated for the upper 980 cm of core to help constrain

chronology (Figure 3.4.1). The Rerewhakaaitu, Waiohau, Poronui, Rotoma, Tuhuna, Whakatane, Waimihia, Taupo and Kawakawa tephra have all been visually recognised and classified by Carter et al. (2008). Although there have been no tephra identified visually in the sections of core examined within the scope of this study, the use of ITRAX on this core has allowed the identification of cryptotephra.

Tephra deposited onshore during MIS3 include the Omataroa (16.2km^3 of estimated total erupted material), Mangaone (19.9km^3), Maketu (11km^3), Hauparu (15.2km^3), Tahuna (4km^3) and Rotoehu (200km^3) tephra (Holt et al., 2014) (See Section 4.8 for ages). Considering the eruptive volume of some of these tephra, and the identification of tephra within younger sections of the core (Carter et al., 2008), we expect to identify glass shards within MIS3. However, the core site also includes glass shards which have been reworked and deposited downslope.

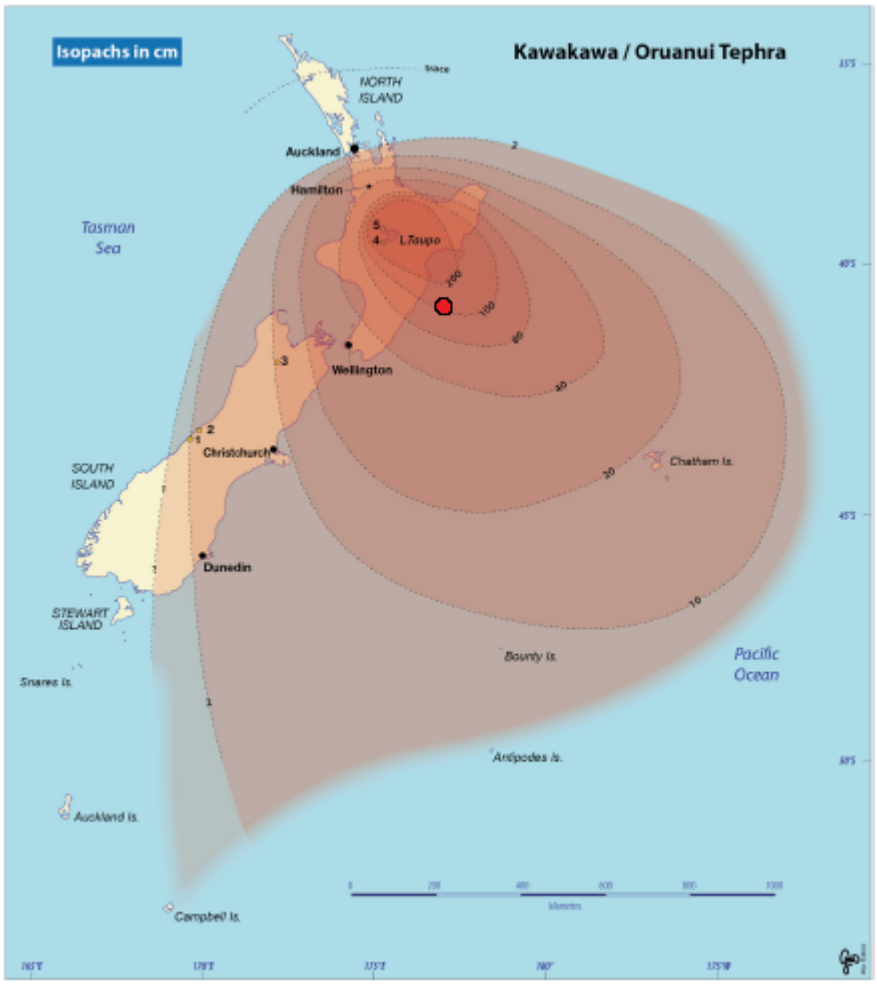

Figure 3.4.1: Dispersal pattern of the Kawakawa Tephra taken from (Vandergoes et al., 2013). The red dot marks the location of MD97-2121 and illustrates its proximity to the TVZ.

4 Methods

4.1 Core Collection

MD97-2121
Core MD97-2121 was collected on May 30th, 1997, using a 45 m-long Calypso giant piston corer. This was deployed during the IMAGES III-IPHIS (Indian and Pacific Ocean Pleistocene and Holocene History) cruise from the French ship, the RV Marion Dufresne. The core is located to the north of the STF, off the eastern coast of the north island of New Zealand at 40°22'56.10"S; 177°59'40.80"E (Figure 4.1.1) and was collected at a water depth of 2,314 m (Carter et al., 2002).

TAN1106-28
TAN1106-28 was collected between April 10th - May 1st, 2011, using a piston corer. This was deployed during the Solander Trough (TAN1106) Voyage of the NIWA vessel, the RV Tangaroa. The core is located just south of the STF south of New Zealand at 48°22'19.20"S; 165°39'32.40"E (Figure 4.1.1) at 2798 m water depth (Bostock, 2011).

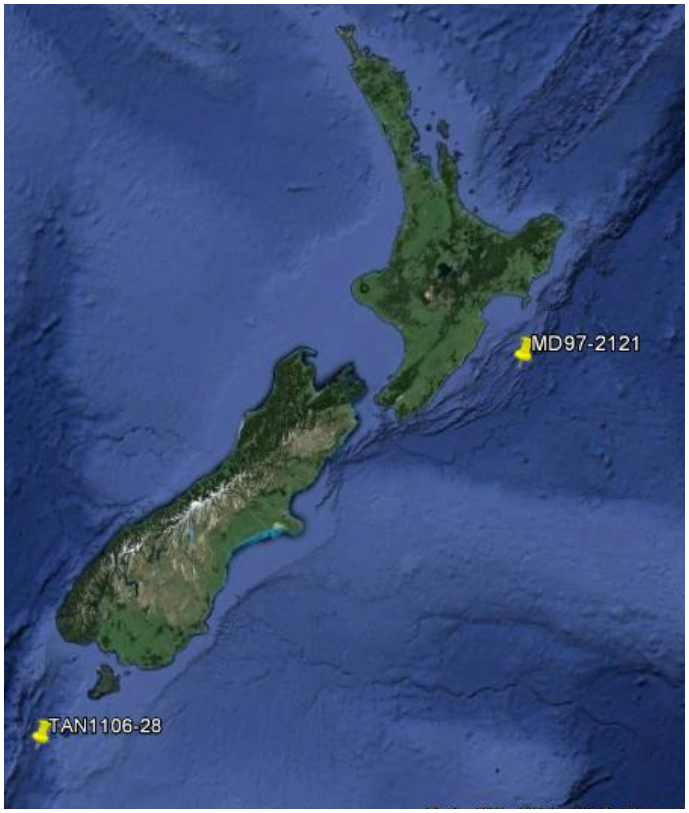

Figure 4.1.1: Location of the high resolution marine sediment cores TAN1106-28 and MD97-2121 analysed in this study

4.2 Sampling

To obtain the resolution needed to recognise millennial scale events, the cores were sampled every <500 yrs throughout the MIS3 time interval. Due to differing estimated sedimentation rates between the cores, this equated to 1 sample every 5 cm in MD97-2121, and 1 sample every 2-3 cm in TAN1106-28.

MD97-2121 had previously been sampled and analysed at a 50 cm resolution for this section of the core (Carter et al., 2002). The working half of core MD97-2121 had also been completely sampled and bagged at 1 cm intervals. Sub-samples were taken from these bags to be analysed during the course of this study. Where no sediment was left, the archive half of the core was sampled. TAN1106-28 had also been previously sampled at 5 cm increments and additional samples were taken between these from the working half of the core. Samples were removed from the core/or bags using a 0.5 cm spatula in the Sediment lab at NIWA and were placed in labelled bags prior to analysis. Care was taken to avoid sampling from the sides of the core as mud can slide along the core barrel during collection, contaminating the sample.

To ensure the entirety of MIS3 was analysed, samples were taken between 980-1,800 cm in core MD97-2121, and 100-455 cm in core TAN1106-28 as preliminary age depth models from lower resolution studies suggest that MIS3 should lie within this range (Carter et al., 2008; Bostock et al., 2015). Sampling from 980 cm also ensured that the Kawakawa tephra (identified by Carter and Manighetti (2006) at 984 cm) was included in the samples. Tephrochronology was used to provide additional age constraints during the development of an age model for MD97-2121. Likewise, sampling the δ^{18}O isotope increase at the end of MIS4 provided an additional tie point for core chronology.

U-channel samples were collected from the archive half of MD97-2121 and TAN1106-28 for ITRAX analysis. Before collecting U-channel samples, the exposed surface of the core was scraped widthwise to remove any oxidised material and reduce contamination. The samples were then cut into 50 cm sections, for ease of shipping, and sealed with electrical tape. Core MD97-2121 was sampled from 750-1,800 cm, and the entire length of core TAN1106-28 was sampled (0-455 cm). The samples were then sent to ANSTO (Australian Nuclear Science and Technology Organisation, Sydney, Australia) where they were gamma irradiated for biosecurity, prior to ITRAX analyses.

4.3 Grainsize

Grainsize analysis of marine sediment cores can give information about the origin of sediment, such as terrigenous mud or biogenic carbonate, and help pinpoint the depths at which cryptotephra may occur.

To prepare samples for grain size analyses, $\approx$ 6.5 g of sediment was wet weighed and placed in the oven at 50°C overnight. The dried sample was then re-weighed, to allow the calculation of water content, before being placed in a container with distilled water for an hour. This allowed the sample to disaggregate. The disaggregated sample was then washed through a 63 μm sieve which separated the mud component from the sand component. Sediment $<$ 63 μm was collected in a container and left to settle before the water was siphoned off and the remaining sediment placed in a warm area to dry. No further analysis was done on the $<$ 63 μm fraction and the dried sediment

was bagged and labelled for storage. The > 63 μm sediment was left to dry overnight on filter paper before being dry sieved to separate the $150 - 63$ μm fraction from the > 150 μm one. The dry weight of these separate grain sizes was recorded.

4.4 Calcium Carbonate

$CaCO_3$ content within a sample gives an indication of biological carbonate productivity in relation to terrestrial input. To prepare samples for carbonate analysis they were first dried at 100°C and then crushed in a mortar and pestle. Crushing of the sample ensures it is homogenised when sub-sampled and allows for a quicker reaction when acid is added. Carbonate content could then be analysed using the carbonate bomb method\vacuum gasometric procedure which has a precision of ±2% (Jones and Kaiteris, 1983). This system uses the change in pressure of a sealed bomb under vacuum, generated by the reaction resulting from adding acid to a sample, to allow the calculation of carbonate content.

A small fraction (0.3 g ±0.03) of sample was placed in the arm of the carbonate bomb with 5 ml of 70% orthophosphoric acid in the side arm. The bomb was then sealed and placed on the carbonate line. When the bomb lid was opened the carbonate line gave the pressure of the sealed bomb. A vacuumed cylinder, with a known volume, was then opened and the second pressure recorded. Applying the ideal gas law (PV=nRT, where P is absolute pressure, V is volume, T is absolute temperature, R is the universal gas constant (8.3145J/mol K), and n is the number of moles), and under a constant temperature (in Kelvins), the pressure of the bomb was calculated using the equation

$$V = \frac{(second\ pressure\ x\ known\ volume\ of\ cylinder)}{(first\ pressure\ -\ second\ pressure)}$$

The air in the bomb was then pumped out to create a vacuum and the new pressure was recorded. Acid from the side arm was mixed with the sample and reacted under vacuum. As the acid reacted with the carbonate in the sample, CO_2 was released changing the pressure within the bomb. To ensure all $CaCO_3$ had reacted with the acid, samples were left for 90 minutes and agitated periodically. The final pressure was recorded and the moles (n) of carbonate content within the sample were calculated using

$$n = \frac{((final\ pressure\ -\ inital\ pressure)(\frac{volume}{1000})}{(83.14472\ x\ temperature)}$$

As $n = mass\ x\ molar\ mass$, the mass of carbonate within the sample could then be calculated. This was divided by the initial weight of the dried sample to give the $CaCO_3$% within the sample. To ensure the accuracy of the machine, a standard (100% carbonate) was included in every run of 20 samples. If the standard was below 95% carbonate content, or the data fell outside of 5% of the original data sets, the samples were run again. Temperature was also recorded throughout the $CaCO_3$ run and the average was then used in the $CaCO_3$% calculations.

Carter et al. (2002) used the vacuum gasometric procedure to analyse the entire length of core MD97-2121 at 10 cm intervals. The samples which fell within 980-1,800 cm depth were incorporated into this study with the first 500 cm of this section repeated as a form of calibration. 1 sample in 10 was then repeated after 500 cm to test for consistency and repeatability.

4.5 Stable isotope analysis

Oxygen isotope ratios are affected by ice volume, salinity, temperature and vital effects, and therefore record changes in oceanic conditions over time. Variations in oceanic $\delta^{18}O$ from benthic foraminifera have been correlated with Milankovitch cycles to give global stacks, such as the LRO4 stack, which spans the last 5.3 myr (Lisiecki and Raymo, 2005). Oxygen isotope sequences from marine sediment cores can be matched with this global record to help constrain the chronology of marine sediment cores.

Individual foraminifera tests were selected from the 250-355 μm fraction, which limits the impact measurements on juvenile specimens can have on $\delta^{18}O$ values, as species vary their position in the water column during their life cycle. The planktic species *Globigerina bulloides* and the benthic species *Uvigerina peregrina* were then picked from each sample using a fine paintbrush under a binocular microscope. Care was taken to ensure the foraminifera picked were clean and contained no visible form of contamination. 4-5 foraminifera tests of each species were placed in a glass thimble, which was then transferred to a carousel of the Kiel device at NIWA. The Kiel device automatically prepares the samples by the addition of a few drops of orthophosphoric acid to produce water and CO_2. The water is removed and the CO_2 gas passes through liquid nitrogen traps before being ionised and pumped into a Finnigan MAT 252 (or 253) isotope ratio mass spectrometer. This device analyses the $\delta^{18}O$ with precision of $\pm$ 0.07 ‰. To ensure continued accuracy, a NBS-19 standard was analysed at the beginning of each run (Neil et al., 2004).

$\delta^{18}O$ isotopes and grain size analysis at 50 cm increments for core MD97-2121 had been analysed by Carter and Manighetti (2006) and were made available for this study. Likewise, $\delta^{18}O$ values at 10 cm intervals for core TAN1106-28 have been previously analysed (Bostock et al., 2015) and were provided for use in this study.

4.6 ITRAX

ITRAX is a non-destructive instrument which measures optical and radiograph variations, magnetic susceptibility, and elemental changes at very high-resolutions ($<$ 200 μm). This enables analysis on decadal to centennial, and possibly annual time scales for cores with high sedimentation rates. Proxy data preserved in the mineralogy and chemistry of sediment cores can then be used to reconstruct environmental change at these time scales. In marine sediment cores, Ca, Fe, Sr, K and Ti are now readily used as tracers of changing environmental conditions (Rothwell and Croudace, 2015).

Samples were run through the ITRAX machine at ANTSO in Lucas Heights, Australia with the help and expertise of Patricia Gadd (and funded by AINSE, grant number ALNGRA15502). They were first scraped horizontally to remove any contaminated sediment and improve the signal to noise ratio of the XRF scanner, before being placed in the ITRAX machine. Care was taken to ensure the sample was level so as not to skew the XRF measurements. Once placed in the ITRAX machine, samples were photographed using a high-resolution digital line scanning camera, with an exposure time of 0 ms and a line camera signal of 198402 at 25 ms. The sample was then covered with microfilm, to prevent drying, and microradiography (X-ray) and XRF were run. A Cr-He tube was used for XRF analysis to allow better detection of lighter elements. Microradiography and XRF scanning was done with a 1 mm step size and an exposure time of 10 seconds. Voltage was

30 Kv and the current was 55 mA for XRF scanning and 40 kV and 10 mA for radiograph analysis.

On ITRAX, magnetic susceptibility was run, at a 5 mm resolution after the XRF scan, as the magnetic sensor touches the surface of the core which can disrupt the surface profile. The break in sediment between 185-191 cm in core TAN1106-28 was filled with polystyrene. Magnetic susceptibility was also run using Bartington MS2 at 20 cm intervals for core TAN1106-28 (Jeromson, 2016) and at 2 and 10 cm intervals for MD97-2121 (Carter et al., 2002). These magnetic susceptibility measurements were made available for comparison with the ITRAX magnetic susceptibility data.

Data from ITRAX measurements were provided in a tabular format. Each U-channel sample corresponded to a folder containing XRF elemental data, magnetic susceptibility values and radiograph images. Spreadsheets for XRF and magnetic susceptibility were pasted together with the depth adjusted to correspond to the depth of the sample within the core. XRF data at the start and the end of the U-channel samples were analysed and removed if they gave an atypical signal (Figure 4.6.1), as the XRF scanner sometimes continued measuring beyond the end of the core. A gap in sediment in TAN1106-28 between 191-185 cm was also excluded from the final spread sheet, and so was an anomalous signal found across all elements between 1365-1346 cm in core MD97-2121 (Figure 4.6.1) although the reason for this is unclear.

4.7 Radiocarbon

Twenty radiocarbon dates were also funded under the AINSE grant. Nine samples were initially analysed for each core with two dates left in reserve in case of misplaced samples or inaccuracies in the construction of the initial age-depth models. Using all available sediment and isotope data, a preliminary age-depth model was constructed for both cores to ensure samples picked for dating were younger than $\approx$ 50 ka.

TAN1106-28
For TAN1106-28 an initial age model was developed by comparing the the amplitude and pattern of $CaCO_3$%, high-resolution ITRAX Ca concentration data, and $\delta^{18}O$ *G. bulloides* data (as a proxy for temperature) with AIM events found in the compiled Antarctic ice core record (CAICR) (Pedro pers comm.) (Figure 4.7.1). While this is circular logic, as one of the primary purposes of this study is to relate the trends in this core to AIM events the purpose of this preliminary age model was to ensure that the depths selected for radiocarbon dating lie within the applicability limit of radiocarbon dating ($\approx$ 50 ka), and a new depth model was developed using calibrated radiocarbon dates. Due to the low $CaCO_3$ % in this core, ^{14}C samples were picked from peaks in $CaCO_3$% ($\approx$ 10-20%), to make picking sufficient planktic foraminifera for radiocarbon analysis easier. More than 3 mg of mixed planktic foraminifera were picked at 133, 175, 218, 243, 255, 273, 283 , 313, and 330 cm depth and sent to ANSTO for radiocarbon analysis under grant number ALNGRA15502.

MD97-2121
An initial age model was developed for MD97-2121 using radiocarbon dates from Carter et al. (2008), which were recalibrated for use in this study (Table 4.1)(Section 4.9). Samples for radiocarbon analysis in this core were selected for depths immediately above and below the tephra horizons at 1345 cm and 1433 cm (See section for identification methods 5.4.3.3). The Kawakawa tephra horizon had been previously dated by Carter et al. (2008) and therefore was not selected

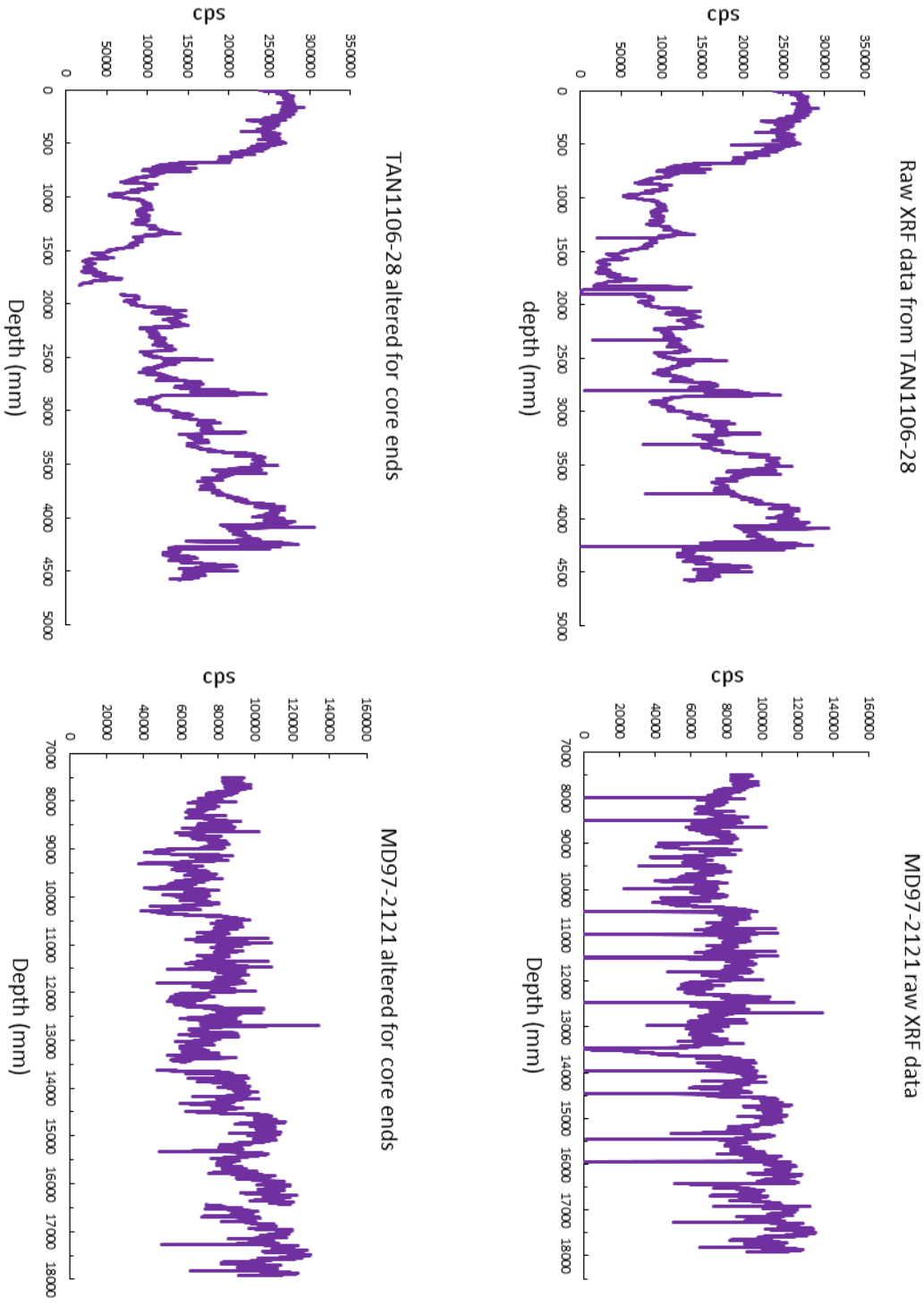

Figure 4.6.1: Adjusting the ITRAX XRF data for core ends. All figures show variations in Ca with figures on the left showing TAN1106-28 and figures on the right MD97-2121. The upper figures show the core data before correction. Ca values interact frequently with the x axis in these figures at core end locations. The lower figures show Ca values when core end discrepancies have been accounted for

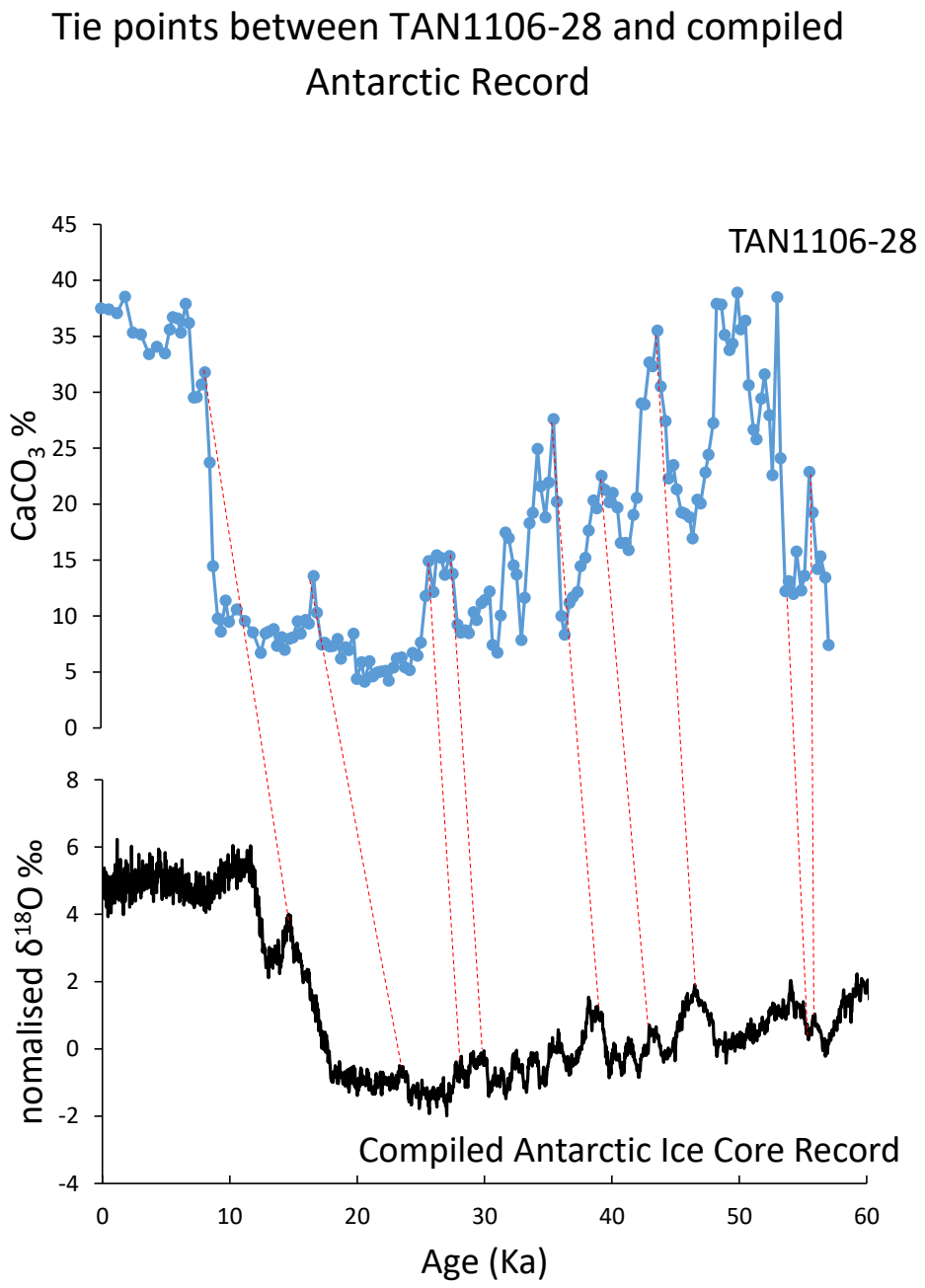

Figure 4.7.1: Correlation between $CaCO_3$% in TAN1106-28 and normalised $\delta^{18}O$ in the Antarctic ice core compilation record (CAICR)(Pedro pers comm.) for the development of a preliminary age model. The blue profile shows $CaCO_3$% through TAN1106-28, the black profile shows variations in $\delta^{18}O$ ‰, and the dashed red line shows tie points between the two records

for radiocarbon analysis. A further 5 samples were selected at depths of 1085, 1195, 1268, 1395, and 1490 cm as these depths filled in gaps between previously selected dates. More than 3 mg of mixed planktic foraminifera were picked per sample for radiocarbon dating at ANTSO (see above).

Depth (cm)	^{14}C (yr)	Error	Calibrated age (yr BP)
983	22590	230	26300
984	22450	130	25690
984	24200	140	27440
1041	24050	130	27290
1126	26250	150	29480
1154	28250	170	31490
1234	31090	250	34330
1309	33590	550	36830
1353	31890	350	35130
1439	38710	410	41950

Table 4.1: Radiocarbon ages for core MD97-2121 from Carter et al. (2008). This original calibration was calculated using a constant offset of + 3240 years

4.8 Tephra analysis

Visual inspection of the archive half of core MD97-2121 showed no obvious tephra layers. This suggests that if any tephra were present in the core, they were cryptotephra. Using the age depth model developed for MD97-2121 by Carter and Manighetti (2006), the depths at which tephra erupted during MIS3 were estimated. The main tephra erupted during MIS3 are the Rotoehu at 45.1±4 ka (Danisik et al., 2012), the Tahuna at 39.3±2.4 ka , the Hauparu at 38.5±2.5 ka (Froggatt and Lowe 1990 modified by Holt et al. 2014), the Maketu at 36.3±1.2 ka, the Mangaone at 33±0.3 ka (Jurado-Chichay and Walker, 2000), the Omataroa at 30.4±1.5 ka (Froggatt and Lowe 1990 modified by Holt et al. 2014), and the Kawakawa at 25.4±0.16 ka (Vandergoes et al., 2013). And, according to the Carter and Manighetti (2006) age depth model, these tephra should occur at ≈ 1461, 1352, 1336, 1290, 1116, 1103 and 984 cm respectively.

4.8.1 ITRAX contribution to tephra identification

Mn, Si, Zr, Fe, Ti, K, Ca, Fe/Ca, Sr and magnetic susceptibility (k) have been used as proxies for volcanic ash (Balascio et al., 2015; Gehrels et al., 2008; Kylander et al., 2012; Lowe, 2011; Vogel et al., 2010; Westerhold et al., 2009). However, as Mn shows considerable background noise it was excluded as a tephra proxy. Magnetic susceptibility was also discounted (Section 5.4.2), and so was Ca and Fe/Ca as the tephra signal is likely to be masked by $CaCO_3$ variation. The remaining tephra proxy elements were analysed to find depths which displayed considerable variation in one or several of these elements. Depths which showed this variation were then examined under the binocular microscope to find visual evidence for glass shards. Sediment examined under the microscope was restricted to the 125-63 μm size fraction, as this is the grainsize where cryptotephra glass shards are expected to be concentrated (Lowe, 2011). Particular attention was placed on variations which occurred in close proximity to the depths which the Carter and Manighetti (2006) age model suggested cryptotephra may occur. Increased frequency of glass shards at 1434, 1345,

1269 and 982 cm suggested cryptotephra were located at these depths.

4.8.2 Grainsize

To quantifiably ensure the depths suggested by the ITRAX data contained the highest concentration of glass shards, samples to either side of the elemental anomalies and 4 and 9 cm out were analysed. These samples were dried and weighed before being reacted with acetic acid to remove carbonate content. As acetic acid is a weak acid, it was less likely to alter the chemistry of the glass shards which is a problem associated with acid digestion (Lowe, 2011). The samples were then washed twice before being wet sieved to remove sediment < 63 μm. Once dry, both the > 63 μm and 150-63 μm size fractions were weighed and recorded.

4.8.3 Electron microprobe analysis

To confirm the origin of the cryptotephra, samples with the highest concentration of glass shards were prepared for electron microprobe analysis (EMP) at Victoria University, Wellington by placing glass shards were placed on double sided sellotape in groups according to the depth they were collected at. They were then placed in a mold and covered with epoxy. Once dried the sample is polished to expose the glass shards. These were then analysed by Dr Ian Schipper under the electron microprobe at Victoria University of Wellington: a JEOL JXA-8230 probe with an absorbed current of 8.0 nA at 15 Kv, and the beam defocused to a 10μm spot size.

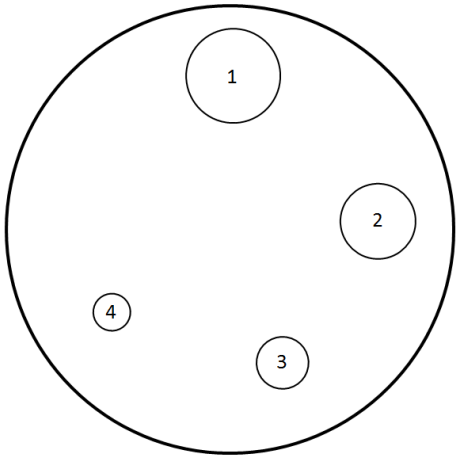

Figure 4.8.1: Glass shard placement on epoxy for EMP analysis. 1=1434 cm, 2=1345 cm, 3=1269 cm, and 4=983 cm

Major element data from the spot analysis of glass shards were then compared to the elemental compositions of the Kawakawa, Omataroa, Maketu, Tahuna and Rotoehu tephra in the literature to determine the origin of the cryptotephra layers in MD97-2121.

4.9 Developing an age-depth model

OxCal was used to develop a final age model for both cores which incorporated all radiocarbon dates, tephra chronology and the MIS4 isotope drop. OxCal is an open source software package

which uses Bayesian statistics for the calibration of radiocarbon dates and statistical analysis of ^{14}C and all other chronological data (Bronk Ramsey and Lee, 2013). Age-depth modelling was done with the help of Dr Jamie Howarth (GNS) on OxCal, version 4.2 (Bronk Ramsey, 2009), using the marine radiocarbon curve, Marine13 (Reimer et al., 2013). As the carbon reservoir age (ΔR) of the ocean is not constant in time (or space), and it has been suggested that it was significantly higher than the contemporary age during the last glacial (Skinner et al., 2015; Sikes and Guilderson, 2016; Sikes et al., 2000), ΔR was modelled using U(-400, 400) to account for this variation through time. To allow for fluctuations in depositions rates within the core, a P_Sequence deposition model was used. This is a Poisson-process deposition model and was used with an event spacing of 1 cm, an interpolation of 1 cm for TAN1106-28 and 5 cm for MD97-2121 and a uniform distribution that covered 2 orders of magnitude (P_Sequence 1, 0.2, U(-2, 2)).

To better develop the age-depth model a general outlier model was run. This identified outliers in time and gave them proportionately less weight in the calibration of the age-depth model. This negated the need to remove the outliers from the code, however it also resulted in agreement indices for the sequence which no longer accurately represented the relationship between the modelled and radiocarbon dates. OxCal was also able to give dates for specific depths within the model. Depths which were thought to contain glass shards (Section 4.8) could then be dated prior to obtaining the radiocarbon dates.

The age model for TAN1106-28 was developed using 3 radiocarbon dates from Bostock et al. (2015) and the 9 radiocarbon dates collected in this study. The age model for MD97-2121 was calculated using radiocarbon dates taken from Carter et al. (2008), which were recalibrated via OxCal to account for the latest adjustments to the radiocarbon curve (MARINE13), radiocarbon dates collected during this study and a selection of tephra dates. Tephra dates were inserted as calibrated dates not radiocarbon dates and therefore needed to be first converted to Gregorian calander ages. The most recent tephra ages were used from Danisik et al. (2012) for the Rotoehu (45.1±4 ka), Froggatt and Lowe (1990) for the Tahuna (39.3±2.4 ka, Vandergoes et al. (2013) for the Kawakawa (25.36 ±0.16 cal. yr BP), and Lowe et al. (2013) for the Rerewhakaaitu (17.46 ±0.46 ka), Waiohau (14.01 ±0.15 ka), (Poronui (11.17 ±0.12 ka), Rotoma (9.42 ± 0.12 ka), Tuhuna (6.58 ±0.55 ka), Whakatane (5.53 ±15 ka), Waimihia (3.40 ±0.11 ka), and Taupo (0.2 ± 0.01 ka) tephra (see appendix 2 for code).

Core	**data generated**	**Reference**
MD97-2121	Radiocarbon dates	Carter et al. (2002)
MD97-2121	$CaCO_3$% and MAR, Grainsize %	Carter and Manighetti (2006)
MD97-2121	$\delta^{18}O$	Carter et al. (2008)
MD97-2121	ITRAX, $\delta^{18}O$, $CaCO_3$% and MAR, EMP Grainsize% and radiocarbon dates	This study
TAN1106-28	$\delta^{18}O$, $CaCO_3$%, Grainsize% and radiocarbon dates	Bostock et al. (2015)
TAN1106-28	ITRAX, $\delta^{18}O$, $CaCO_3$% and MAR, Grainsize% and radiocarbon dates	This study

Table 4.2: Summary of data sets used in this study

5 Results

5.1 Grainsize

TAN1106-28

Grainsize data for TAN1106-28 shows that the dominant composition of this core is mud (< 63 μm grainsize). Grainsizes range between 0.13-19.88% for grains > 150 μm, and between 0.75-18.57% for the 63-150 μm sediment. These grainsize occurrences are strongly correlated in the analysed section of TAN1106-28 (with a correlation coefficient of 0.89), although they deviate at 283 cm and 220 cm, where the %150-63 μm peak exceeds that of the > 150 μm% fraction. Both grainsizes show abrupt peaks at 423, 403, 390, 353, 320, 303, 283, 255, 243 and 220 cm with smaller sub-peaks at 443 and 135 cm (Figure 5.1.1).

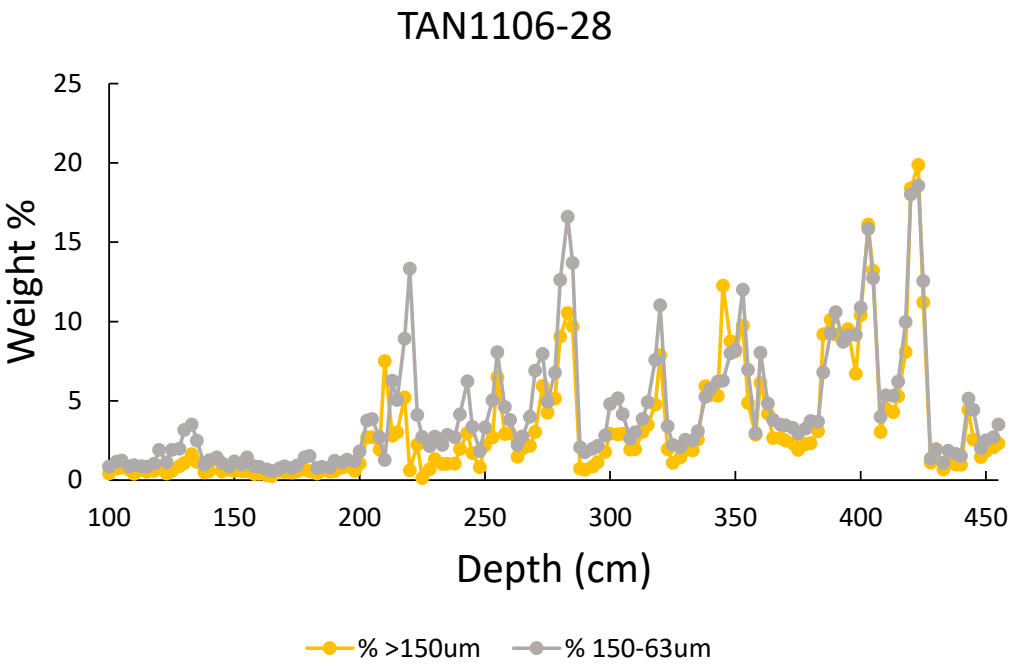

Figure 5.1.1: Grainsize proportions along a 350 cm section of TAN1106-28

MD97-2121

The dominant sediment in MD97-2121 is mud (< 63 μm grainsize) and overall the core displays no trend in grainsize and has only a moderate correlation between the $63 - 150$ μm% and the > 150 μm% sediment size fractions (with a correlation coefficient of 0.65). The percentage of both grainsizes is small with $63 - 150$ μm% grains ranging between 0.5%-5.07% and the > 150 μm% ranging between 0.29-6.25%. A prominent peak in both > 150 μm% and $63 - 150$ μm% sized grains occurs at 1480 cm, and, to a much smaller degree, at 1430 cm (Figure 5.1.2). There are also several increases in the $63 - 150$ μm% at 1695, 1345, 1,245, 1,695, 1,170, and 1,060 cm (Figure 5.1.2).

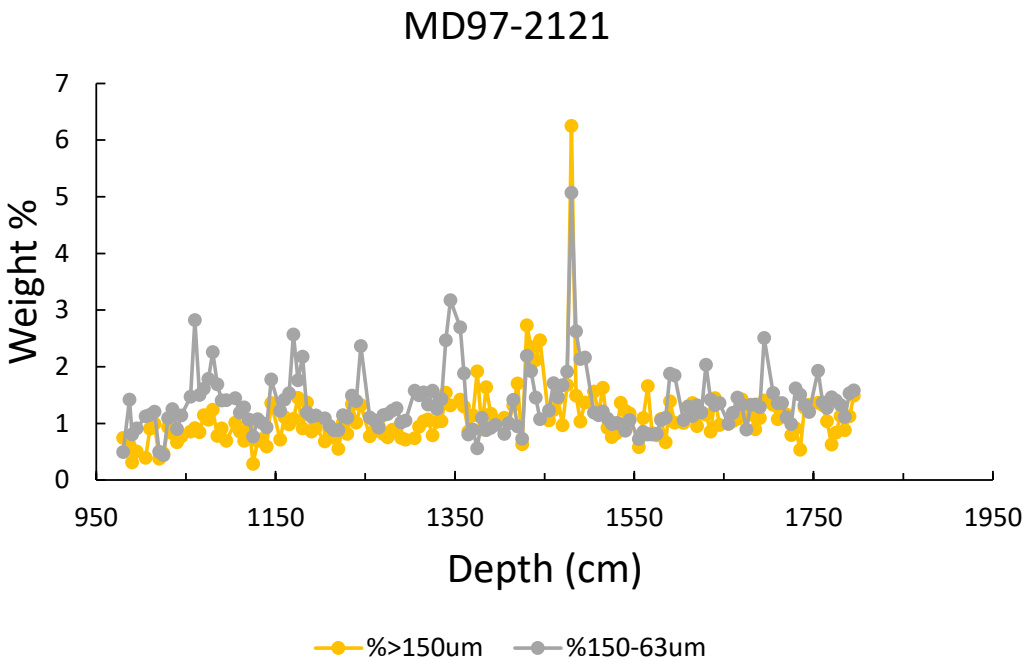

Figure 5.1.2: Grainsize proportions along a 1000 cm section of core MD97-2121.

5.2 Carbonate

TAN1106-28

$CaCO_3$ content is low-moderate in TAN1106-28, ranging from 4.14-38.91%. Although the general trend shows a decrease in $CaCO_3$% from 423-100cm, $CaCO_3$ % fluctuates rapidly between relative minima and maxima (Figure 5.2.1).

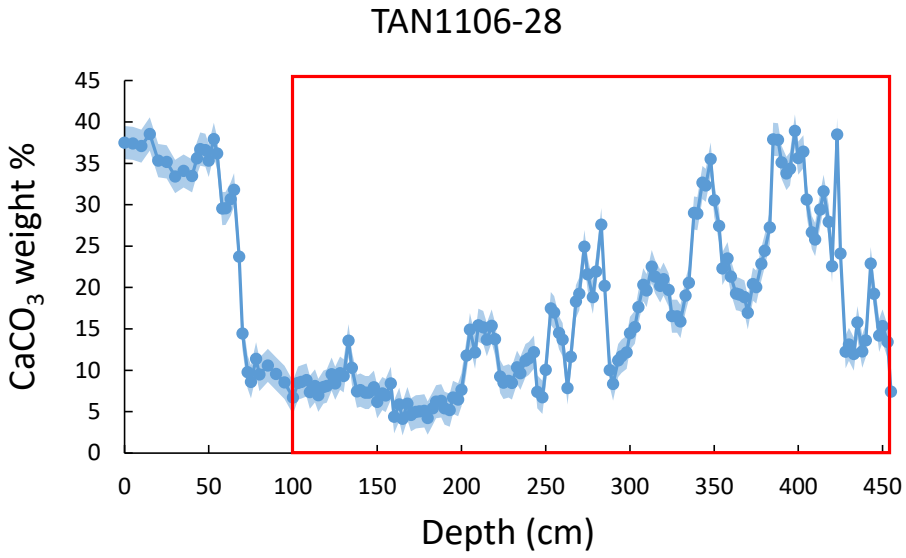

Figure 5.2.1: $CaCO_3$% in TAN1106-28. The red box encompasses MIS3 $CaCO_3$ % calculated through this study. The upper metre of core shows $CaCO_3$% from Bostock et al. (2015). The blue shaded area shows the error of the vacuum gasometic procedure ($\pm$ 2 %)

Peaks in $CaCO_3$% occur at 443, 423, 398, 348, 315, 283, 255, 220, and 133 cm in a saw tooth pattern (Figure 5.2.1). Excluding an anomalous low peak in carbonate content at 443 cm, these peaks follow a general trend, decreasing in both size and intensity from 425-100 cm. The upper meter of core, analysed by Bostock et al. (2015), does not display the $CaCO_3$ % peaks characteristic of the lower sections of core, but instead shows a sharp increase in carbonate content from 6.71%, at the end section of this study, to 41% at the top of the core (Figure 5.2.1).

There is a strong correlation between $CaCO_3$% and grainsize (Figure 5.2.2). For sediment size fraction $> 150\mu$m% and $CaCO_3$% the correlation coefficient is 0.84, and for the sediment fraction between $150 - 63\mu$m% the correlation is 0.76. The timing of grainsize peaks coincides with the timing of $CaCO_3$ peaks (Figure 5.2.2). However, although there is a strong correlation between the shape and location of peaks and the grainsize and carbonate data, sediment $> 63\mu$m does not show the same overall decreasing trend that the carbonate data displays.

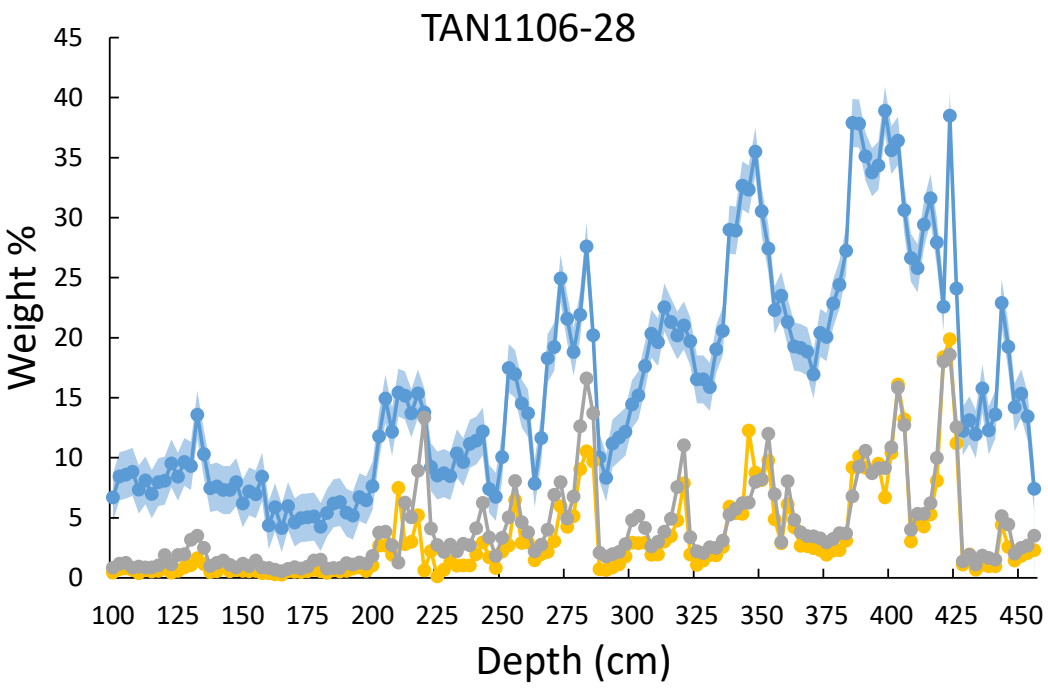

Figure 5.2.2: TAN1106-28 grainsize % and $CaCO_3$ %. The blue profile shows $CaCO_3$ % with the shaded area showing the error of the vacuum gasometic procedure ($\pm$ 2 %), the yellow profile shows the relative abundance of the >150 μm size fraction and the grey profile shows the same for the 150-63 μm size fraction

MD97-2121

MD97-2121 contains low levels of carbonate that range from 4.6-14.6% and show a decreasing trend in carbonate percentage toward the upper section of MIS3 (Figure 5.2.3b). There is not however, significant evidence for the saw-tooth pattern which governs the carbonate trend in core TAN1106-28. There is a negligible correlation between $CaCO_3$% and both the $63 - 150\mu$m% (a correlation coefficient of 0.19) and the $> 150\mu$m% (a correlation coefficient of 0.16).

When compared to $CaCO_3$ percentages analysed previously for the rest of this core, MIS3 carbonate values are distinct. This is the only section of core that shows a prolonged decrease in $CaCO_3$ % and there is a muting of $CaCO_3$ % peaks. The lack of variation in $CaCO_3$% within MIS3 is particularly evident when compared to the deeper sections of core where $CaCO_3$ values vary significantly (Figure 5.2.3a).

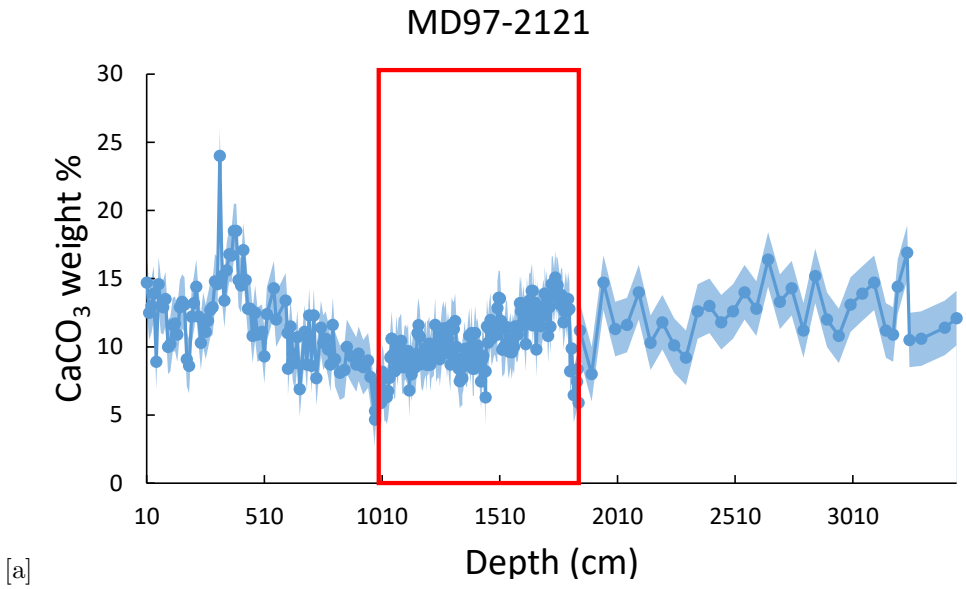

[a]

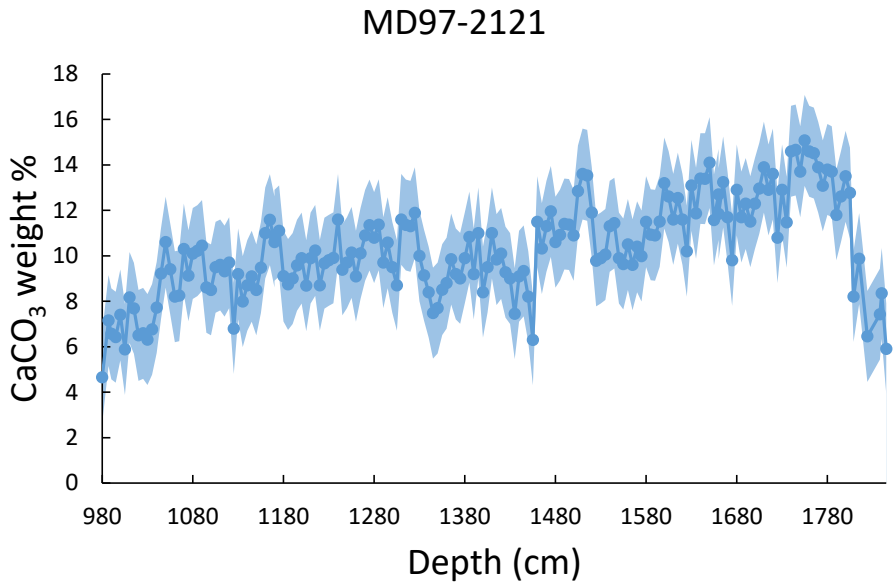

[b]

Figure 5.2.3: MD97-2121 $CaCO_3$%. The blue profile shows $CaCO_3$ % with the shaded area showing the error of the vacuum gasometic procedure (± 2 %). [a] = $CaCO_3$% for MD97-2121 from Carter et al., 2002. The red box outlines $CaCO_3$% for MIS3 with values from this study superimposed on this section, and [b] = $CaCO_3$% in MD97-2121 during MIS3 calculated from vacuum gasometic data

5.3 Stable isotope analysis

The $\delta^{18}O$ signatures of the high-resolution planktonic (*G. bulloides*), and the low resolution benthic (*U. peregrina*) foraminifera, show very little evidence for millennial scale events, through MIS3 in TAN1106-28 though the benthic signal contains large amplitude variations (Figure 5.3.1). Excluding anomalous $\delta^{18}O$ signals, at 188 cm in *G. bulloides*, and 390 cm in *U. peregrina*, $\delta^{18}O$ levels range from 1.93-3.95‰ for *G. bulloides*, and 3.90-5.14‰ for *U. peregrina* during MIS3. There are no millennial scale events visible in the high-resolution planktonic isotope signal but, the small

fluctuations in the low resolution benthic signal are defined by single points making it difficult to identify millennial scale events (if there are any). Stable oxygen isotopes run at a higher resolution for *U. peregrina* (that were prepared for this study, but are not yet available due to unforeseen circumstances), may enable the identification of millennial scale peaks during MIS3 in the benthic signal.

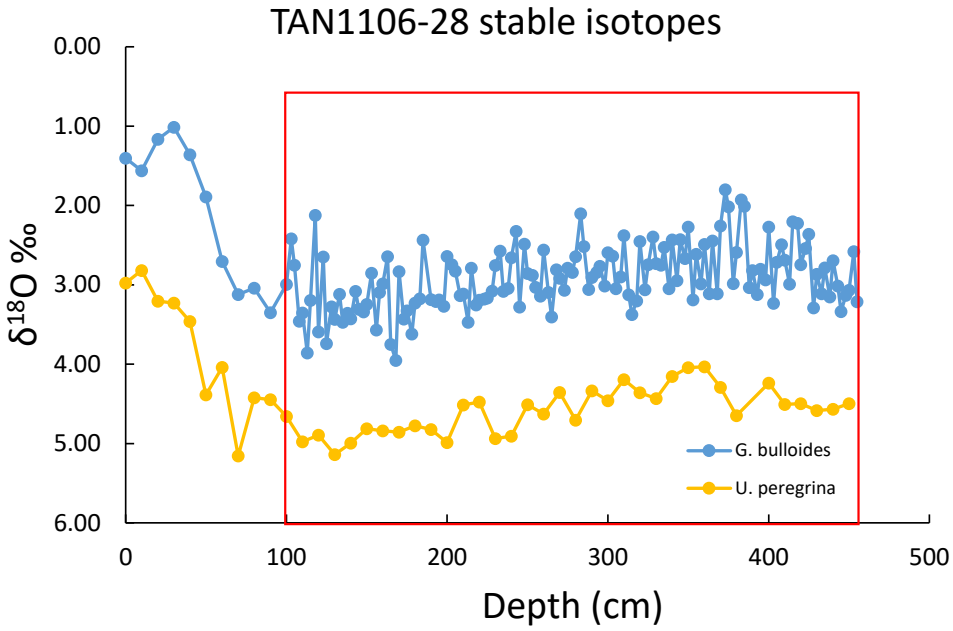

Figure 5.3.1: TAN1106-28 δ^{18}O. *G. bulloides*, in blue, is from Bostock et al. (2015) for the upper m of core and is combined with high resolution stable isotopes run during this study for MIS3. *U. peregrina*, in orange, is from Eva Calvo pers comm and the red box outlines MIS3. Outliers at 188 cm in G. bulloides and 390 cm in U. peregrina were not graphed

Low resolution isotope analysis for MD97-2121 was run for MIS3 at 20cm intervals by Carter and Manighetti (2006). The correlation coefficient between δ^{18}O values for *G. bulloides* and *U. peregrina* during this period is extremely high (0.90) (Figure 5.3.2a. However, *G. bulloides* has lower δ^{18}O values, ranging from 1.35 to 2.6, in comparison to the heavier *U. peregrina*, which ranges from 4.5 to 4.92. There some variation in the planktic δ^{18}O curve during MIS3 ($\approx 2‰$) but little variation in benthic δ^{18}O (Figure 5.3.2b). However, development of a high-resolution δ^{18}O record could discover peaks missed in the lower resolution analysis.

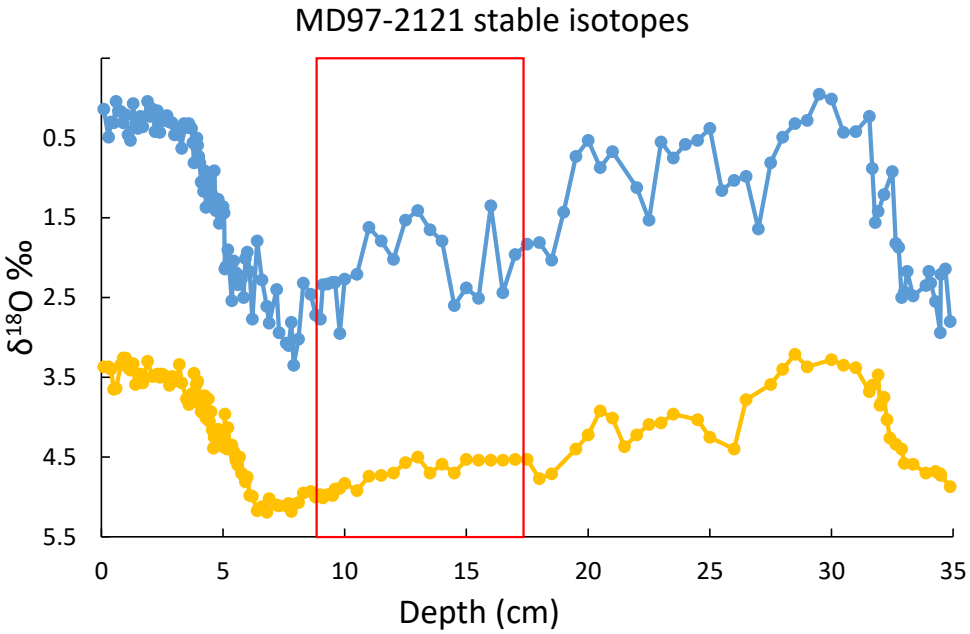

[a]

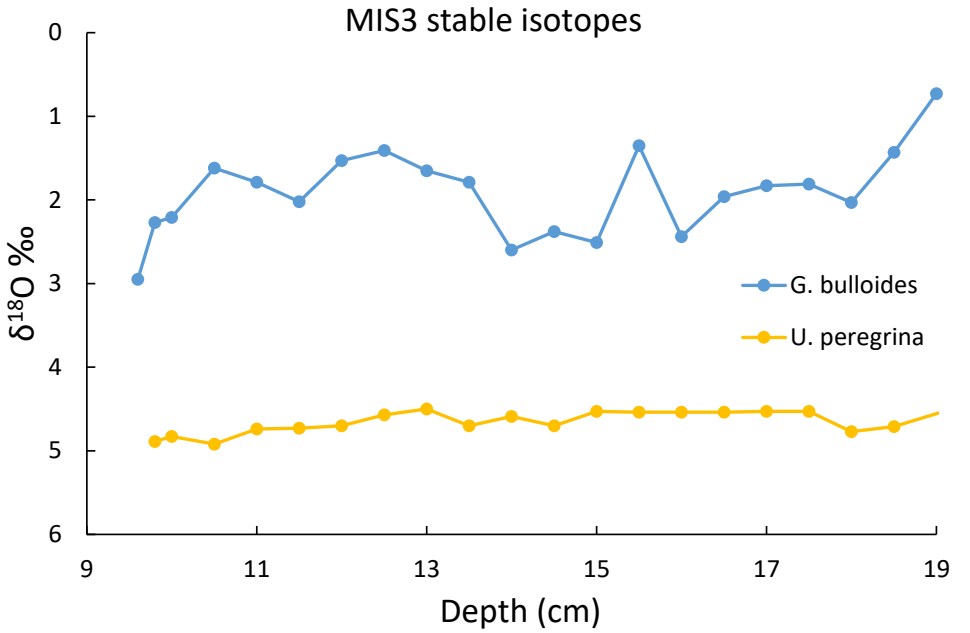

[b]

Figure 5.3.2: MD97-2121 MIS3 δ^{18}O from Carter and Manighetti (2006). (a) shows δ^{18}O for the entire length of MD97-2121 with the red box covering MIS3, and (b) shows only MIS3. *G. bulloides* for both figures is shown in blue, and *U. peregrina* is shown in orange

5.4 ITRAX

To test the validity of the ITRAX XRF Ca data, these were compared with $CaCO_3$ percentages calculated using the vacuum gasometric procedure (Section 4.4). The high correlation coefficient between the two, of 0.91 for TAN1106-28 and 0.72 for MD97-2121, helps legitimise the XRF findings and confirms that Ca is mainly hosted in $CaCO_3$ in these cores (Figure 5.4.1).

5.4.1 Radiograph (X-Ray)

The radiograph shows changes in density and can be used to recognise turbidites in marine sediment cores. As turbidites represent instantaneous deposition they render sections of the core unusable for the paleo-oceanographic purposes of this study. However, the homogeneous nature of both cores in the high-resolution X-ray images (see appendix 3) shows no evidence of turbidites.

5.4.2 Magnetic susceptibility

k is the sum of all mineral contributions to magnetic susceptibility measurements, including ferromagnetic, paramagnetic and diamagnetic minerals. As ferri/ferromagnetic minerals have the strongest magnetism they are a primary control over k (Rothwell and Croudace, 2015). Fe-Ti oxides are important ferri/ferromagnetic minerals and commonly correlate strongly with k measurements (Funk et al., 2004a,b).

Lower resolution magnetic susceptibility measurements obtained from Carter and Manighetti (2006) and Jeromson (2016), show a moderate correlation with the high-resolution ITRAX k data (Table 5.1).

	TAN1106-28$\boldsymbol{k}$	MD97-2121$\boldsymbol{k}$
Ti	0.35	-0.35
Fe	0.38	-0.31
Al	0.26	-0.10
k (Jeromson, 2016)	0.64	
k (Carter et al., 2008)		0.74

Table 5.1: Correlation coefficient between magnetic susceptibility and ferri/ferromagnetic elements for both cores

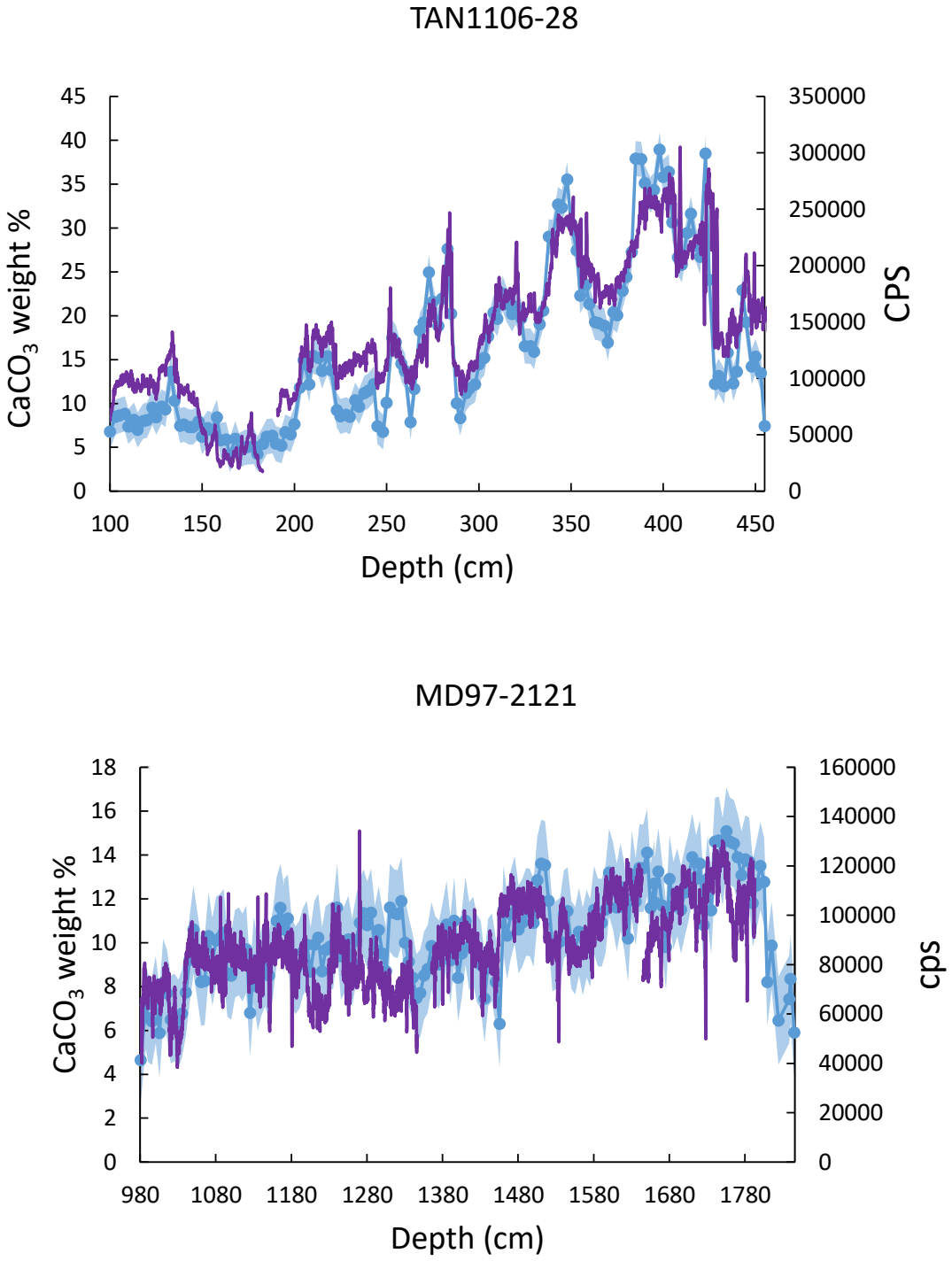

Figure 5.4.1: ITRAX Ca vs vacuum gasometic $CaCO_3$%. Purple = Ca, Blue = $CaCO_3$% and light blue shows the error associated with the vacuum gasometic procedure (±2%)

TAN1106-28

k from TAN1106-28 ranges from 7.24 to 101.78. The overall k trend shows two major peaks: a sharp peak at 442 cm and a broader, taller peak centred over 244 cm (Figure 5.4.2). There are oscillations in k overriding this overall trend, which occur $\approx$ every 25 cm in both the lower resolution and ITRAX data. However, in spite of the k cyclicity, these oscillations have neither the timing nor the magnitude of the $CaCO_3$ events.

MD97-2121

In MD-97-2121, k data ranges from 1.74 to 9.71. There is no discernible trend and k fluctuates rapidly in the ITRAX data throughout MIS3. Lower resolution k data from Carter et al., 2006 does not capture this variation (Figure 5.4.3) however, when compared with k values for the entire length of core, MIS3 still shows negligible change (Figure 5.4.3). This is particularly evident when compared to the magnitude of k that is found in the top 5.5 m of core. A possible explanation for this subdued signal across the two methods of k measurement, is diagenetic dissolution of magnetic minerals.

The possibility of diagenetic dissolution and the lack of correlation between Fe, Ti and k across both cores (Table 5.1) has resulted in k been deemed an unsuitable proxy for use in this study and is not discussed further.

5.4.3 XRF

XRF collects profiles for elements heavier than Mg. However, heavier elements (eg Mg and Al) are often unreliable. Some of these elements may provide information about climate and oceanographic conditions at the core site. Elements that were considered useful in this study needed to be well established as a proxy in literature and have significant cps to reduce the impact of the background signal. Data were analysed both as lone element signals and element ratios. Element ratios provide useful proxies as they can isolate different components impacting an elements cps and remove dilution effects (Weltje and Tjallingii, 2008). In this study, elements are normalised to Ca, to account for $CaCO_3$ variability, and Ti, to remove terrigenous variability. Al is a common aluminosilicate indicator however, in spite of the Cr XRF tube which allows better analysis of heavier elements, the Al data contains considerable background noise (see appendix 3) and therefore Ti was used instead.

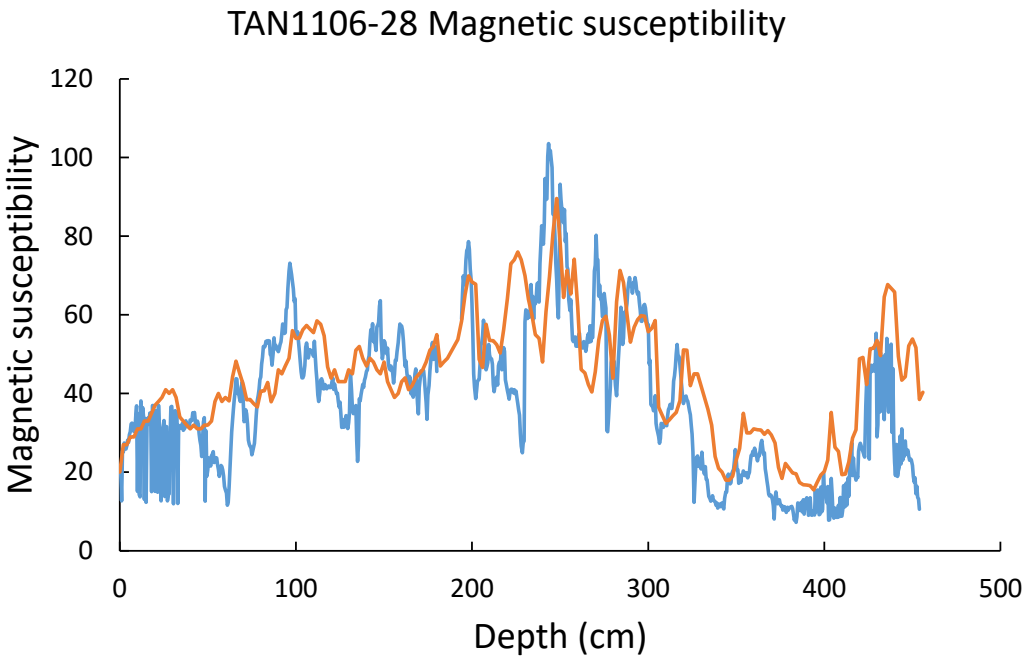

Figure 5.4.2: Comparison between magnetic susceptibility generated using ITRAX (blue) and Jeromson (2016) (orange) for TAN1106-28. Jeromson (2016) values were generated using a Bartington MS2 system with a hand held probe at NIWA

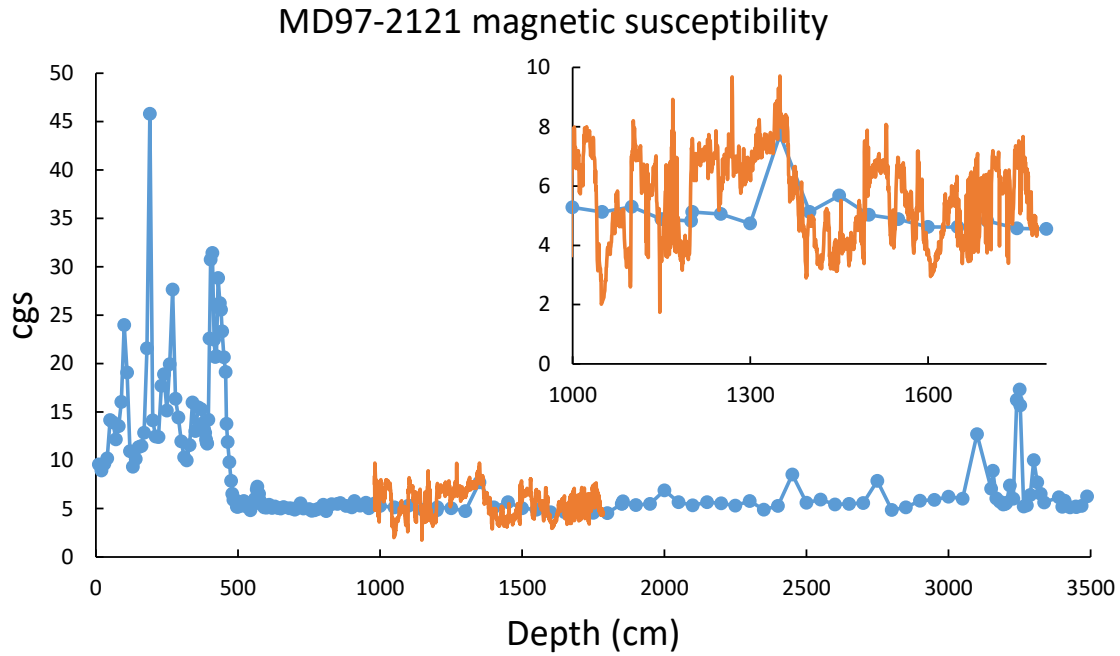

Figure 5.4.3: Comparison between magnetic susceptibility generated using ITRAX (orange) and Carter et al. (2008) (blue) for TAN1106-28. Carter et al. (2008) values were generated using a Bartington MS2 system with a hand held probe at NIWA

5.4.3.1 Terrigenous input

TAN1106-28

Elements used to indicate fluxes in terrigenous sediment in the literature include Al, Si, Fe, K and Ti (Rothwell and Croudace, 2015). These elements are often used in conjunction with Ca, to compare biological productivity to terrigenous input and give an indication of climate variability. Ti and Fe appear frequently in XRF studies of marine sediment cores as they best represent terrigenous variability (Agnihotri et al., 2008; Rothwell and Croudace, 2015). As Ti is redox insensitive it is used preferably over Fe in this study although, there is a strong correlation between Fe and Ti elements in both cores (Table 5.1) Si and K were excluded for use as they are used as proxies for other climate variables within this study (Section 5.4.3.2 and 5.4.3.3 respectively).

All terrigenous proxies are strongly correlated in TAN1106-28, with correlation coefficients of > 0.82. The correlation coefficient between Fe and Ti is particularly high (0.97), with both elements also displaying a moderate, negative correlation with Ca of -0.67 and -0.56 respectively (Figure 5.4.4). This anticorrelation is reflected in the antiphased timing of peaks and troughs through core TAN1106-28. The core end starts with a drop in Fe and Ti cps at 426 cm. This is followed by a series of sharp well defined peaks that defines the mid-section of core at 409, 355, 320, 284, 252, and 220 cm. These peaks become broader and less frequent upcore, deviating at the core break (191-185 cm), where both Ti and Fe show fluctuating decreases in cps before stabilising at high values at 150 cm (Figure 5.4.4a and 5.4.4b).

Ti/Ca values for TAN1106-28 show the same peaks as the terrigenous elements Ti and Fe. Notable differences between the terrigenous elements and the Ti/Ca ratio include, the large peak at 165 cm, and a steady increase in Ti/Ca upcore reflecting the broader Ca trend. The upper 100 cm of core displays a drastic drop in terrigenious elements (see appendix 3) which coincides with an increase in Ca (Figure 5.2.1).

MD97-2121

MD97-2121 shows variable correlations between terrigenous elements, ranging from 0.39-0.92 (Figure 5.4.5). The Fe-Ti correlation coefficent is strong, 0.83, but at times the two terrigenous proxies are out of phase with notable deviations occurring at 1096, 1145, 1270, 1345, 1434, and 1727 cm (Figure 5.4.5a and 5.4.5b). Neither Fe nor Ti show any correlation with Ca (Figure 5.4.5).

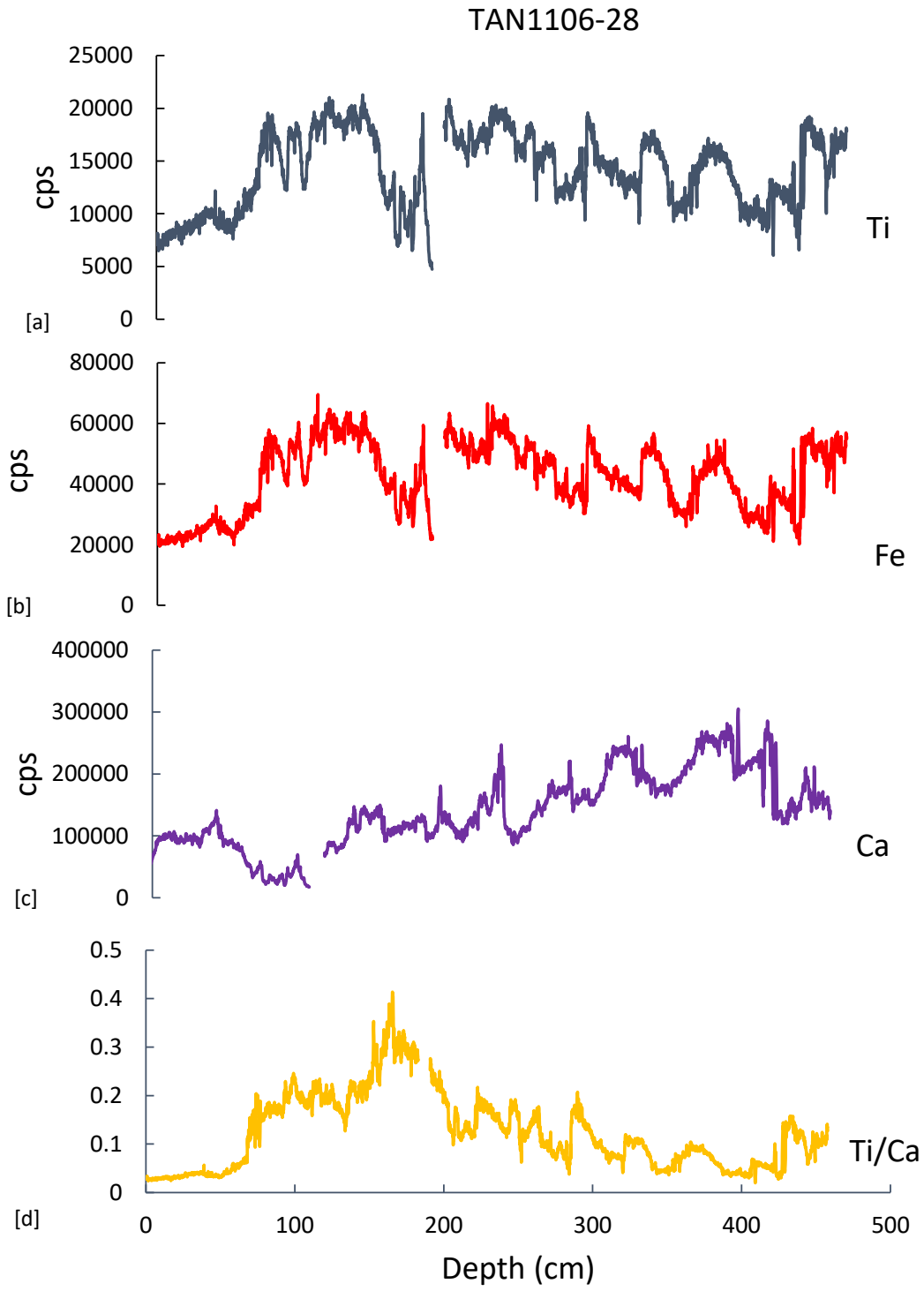

Figure 5.4.4: Comparison between terrigenous input and biological productivity for TAN1106-28. [a] shows Ti as a proxy element for terrigenous input, [b] shows Fe as a proxy element for terrigenous input, [c] shows Ca as a proxy element for biological input, and [d] shows the Ti/Ca ratio to compare the terrigenous and biological inputs.

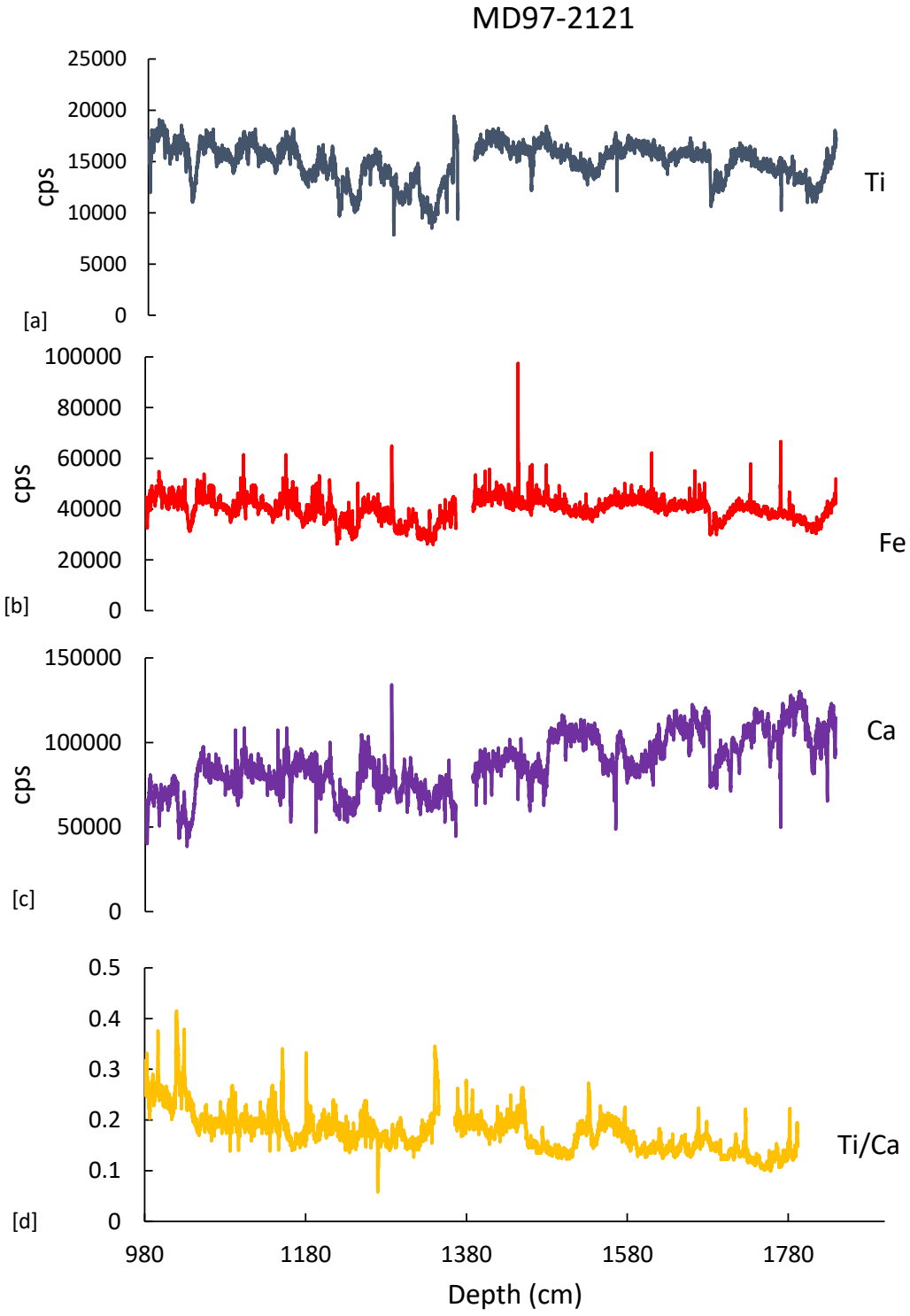

Figure 5.4.5: Comparison between terrigenous input and biological productivity for MD97-2121. [a] shows Ti as a proxy element for terrigenous input, [b] shows Fe as a proxy element for terrigenous input, [c] shows Ca as a proxy element for biological input, and [d] shows the Ti/Ca ratio to compare the terrigenous and biological inputs.

5.4.3.2 Biological productivity

TAN1106-28

Biological productivity was examined in both cores using the elemental proxies Ca, Si and Ba(Rothwell and Croudace, 2015). In the reconstruction of biological productivity, Si is commonly used to track opal changes (Agnihotri et al., 2008; Cartapanis et al., 2012; Ziegler et al., 2010), Ca shows variations in carbonate production (Cartapanis et al., 2012), and Ba precipitates with decaying organic matter (Ziegler et al. 2010 and references therein). All these biological proxies contain a detrital component, and therefore were normalised to a terrigenous element (Ti) to extract the biological signal (Agnihotri et al., 2008; Cartapanis et al., 2012; Ziegler et al., 2010). The Ba/Ti ratio has a wide range across both cores so a 20 pt average was calculated to better display long term trends and variability. Br can also be used as a proxy for ocean productivity (Agnihotri et al., 2008; Cartapanis et al., 2012) however, due to low cps and frequent interactions with the x axis (see appendix 3), it was excluded from use in this study.

In TAN1106-28, Ca/Ti shows the greatest variation, ranging between 50.28 and 2.42 cps. Major peaks in the Ca/Ti ratio occur at 445, 425, 409, 351, 320, 284 and 252 cm, with minor peaks at 215, and 134 cm (Figure 5.4.6a). This pattern is reflected in a more subdued manner in the Si/Ti ratio. Si/Ti ranges from 0.15-0.4 and shows peaks at 445, 425, 409, 351, 320, 284 and 250 cm (Figure 5.4.6b). The reproducibility in the timing of these peaks between Si/Ti and Ca/Ti is evident in the high correlation coefficient of 0.8.

Ba/Ti shows no correlation with Ca/Ti (with a correlation coefficient of 0.26), and very little correlation with Si/Ti (a correlation coefficient of 0.38). It intersects with the x-axis and ranges up to 0.09, suggesting that Ba/Ti might not accurately reflect changes in biological productivity at the site of TAN1106-28. Therefore it was excluded from further analysis of biological productivity within this core.

MD97-2121

The Ca/Ti ratio in MD97-2121 shows two major features. The first is a steady decrease in Ca/Ti from 1,800-970 cm, and the second is a major peak in Ca/Ti at 1,270 cm. This peak is not located near a core end and as it is defined by several points, it is unlikely to be a random outlier. Superimposed on these major trends are a series of smaller peaks which occur at 1,770, 1,660, 1,512, 1,408 and 1,319 cm (Figure 5.4.7a). This pattern shows no correlation with Si/Ti (with a correlation coefficient of 0.09). Si/Ti ratios range from 0.19-0.69 and show four possible peaks, at 982, 1,345, 1,533, and 1,727 cm, and 5 minor spikes, at 1,205, 1,332, 1,340, 1,448 and 1,782 cm (Figure 5.4.7b). As neither Ca/Ti (with a correlation coefficient of 0.16) nor Si/Ti (with a correlation coefficient of 0.17) showed any significant correlation with Ba/Ti and, as the Ba/Ti signal was low and contained significant background noise (Figure 5.4.7c), it was also excluded as a proxy for biological reconstruction at the site of MD97-2121.

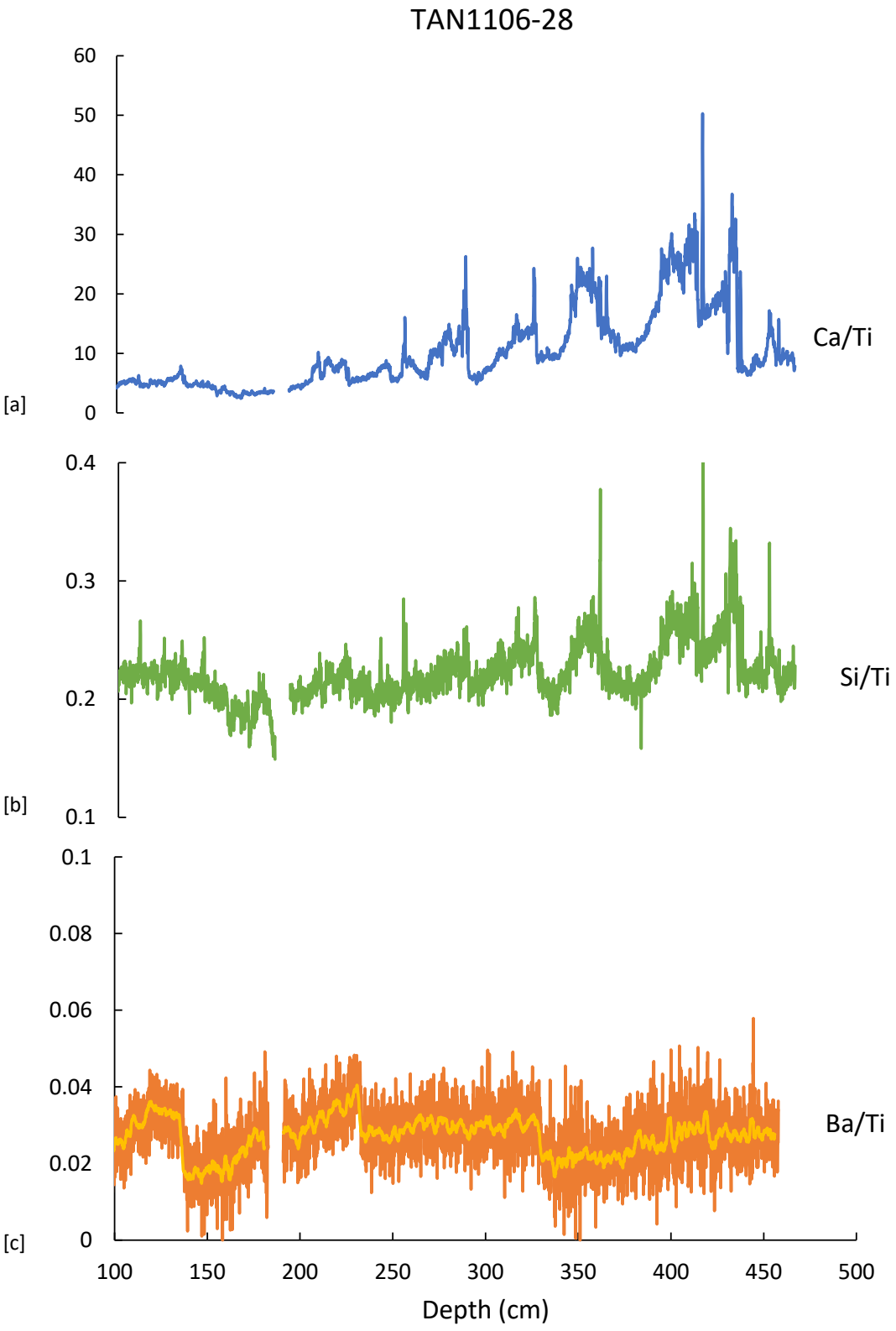

Figure 5.4.6: TAN1106-28 biological productivity proxies. [a] = Ca/Ti, [b] = Si/Ti and [c] = Ba/Ti with the thick yellow line showing a 20pt average for Ba/Ti

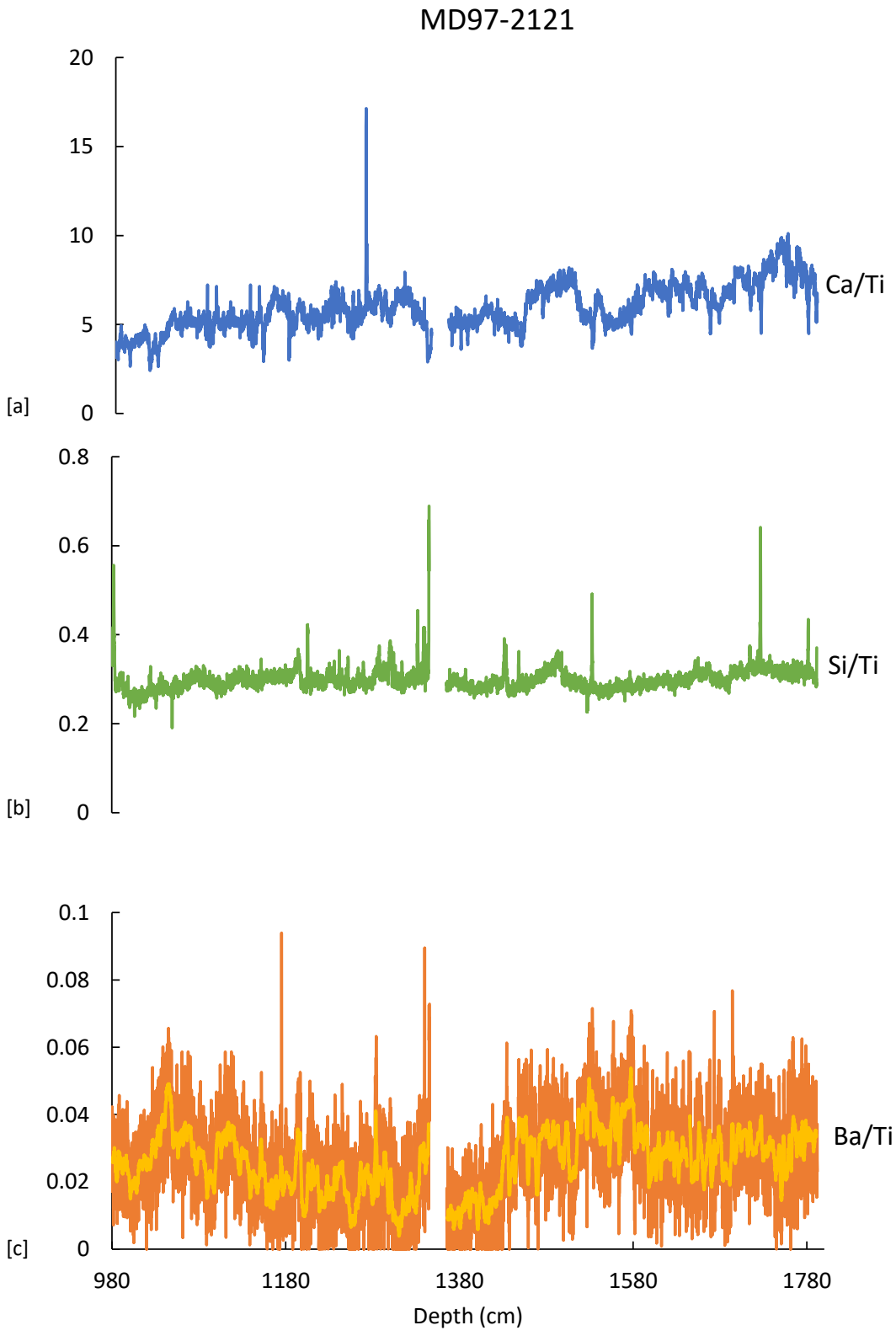

Figure 5.4.7: MD97-2121 biological productivity proxies. [a] = Ca/Ti, [b] = Si/Ti and [c] = Ba/Ti with the thick yellow line showing a 20pt average for Ba/Ti

5.4.3.3 Identifying cryptotephra

Relatively few studies have been published on the identification of cryptotephra layers in marine sediment cores through the use of high-resolution XRF data. Of the publications available, few appear confident in identifying rhyolitic cryptotephra due to the similarities in composition between rhyolitic tephra deposits and the background signal (Balascio et al., 2015). To locate tephra layers within MD97-2121, depths which showed changes in Zr, Sr, Ti, K, Fe and Si were examined under a binocular microscope for further observational evidence of glass shards, and this was considered confirmation of the presence of a cryptotephra deposit. As the oldest MIS3 tephra is the Rotoehu tephra, which erupted 45.1±4 ka (Danisik et al., 2012), elemental variations were only examined at depths shallower than 1550 cm as a preliminary age model from Carter and Manighetti (2006) suggests an age of 44.8 ka at this depth. TAN1106-28 was not analysed for tephra as it is located too far from the TVZ, the main source of volcanism in New Zealand, to record cryptotephra deposits, with the possible exception of the Kawakawa tephra which has been recorded on the Bounty Fan.

In sediment core MD97-2121 the Kawakawa tephra was identified in Carter and Manighetti (2006) at 982 cm. Notable variations in the ITRAX XRF data at 983 cm include a dramatic spike in Zr and, less drastic but still notable changes in Ti, K, and Si suggesting the presence of a rhyolitic tephra. Other notable changes in Zr, Sr, Ti, K, Fe and Si occurred at 1533, 1434, 1418, 1387, 1345, 1269, 1145, 1095, and 1023 cm (Figure 5.4.8). However, when examined under the microscope, only the 1345 and 1434 cm samples showed significant proportions of glass shards (above background levels). These samples were selected for further analysis (see below) along with the Kawakawa (983 cm) sample. ITRAX XRF data at 1,269 cm shows variations across all tephra proxies and therefore was also selected for further analysis in spite of a lack of observational evidence for glass shards above background levels. These samples will henceforth be referred to as tephra 1 (1434 cm), 2 (1345 cm), 3 (1269 cm), and 4 (983 cm).

Tephra 2 occurs near a u-channel core end and this has resulted in the loss of reliable ITRAX XRF data across this deposit. However, significant changes in Ti, Fe, Sr and K are still apparent, with Sr and K cps peaking and Ti and Fe dipping at this depth. Tephra 4 is also difficult to identify in the ITRAX XRF data. Peaks occur in Fe, K, and Zr and troughs are apparent in Sr and Ti, but this pattern is repeated across multiple depths (Figure 5.4.8) and the tephra was only distinguished through the use of the binocular microscope.

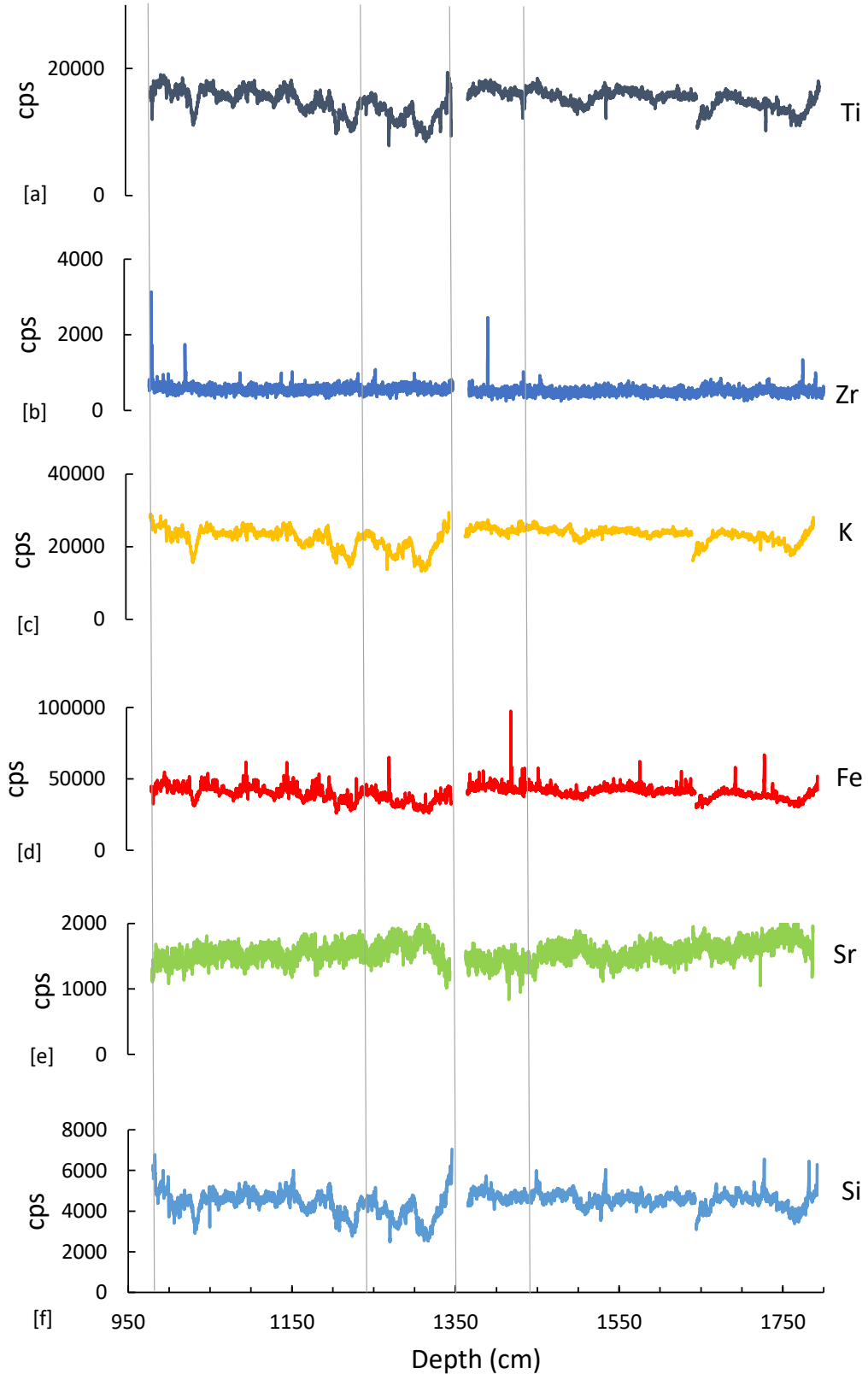

Figure 5.4.8: XRF Tephra proxies from core MD97-2121. [a] = Ti, [b] = Zr, [c] = K, [d] = Fe, [e] = Sr, [f] = Si, and the grey lines show potential cryptotephra deposits

5.5 Cryptotephra

To build on the information gathered via ITRAX XRF, a variety of techniques were used in an attempt to establish the exact location of cryptotephra deposits and accurately identify the eruption they originated from.

5.5.1 Grainsize analysis

Acid digestion removed all carbonate from the samples leaving terrigenous material, glass shards, and opal. Carter and Manighetti (2006) showed that opal% is negligible in MD97-2121 and therefore it was assumed that any sediment that was not dissolved during acid digestion was terrigenous in origin. As this method concentrated glass shards within a sample, it was assumed grainsize analysis of these samples should identify depths where glass shards were the most frequent. Because cryptotephra glass shards are typically found in the 150-125 μm grainsize fraction, it was assumed that there would be a peak in this grainsize once the sample had undergone acid digestion. Both 150-125 μm and > 150 μm percentages were analysed as some tephra contained glass shards > 150 μm however, overall changes in the grainsize% were small and displayed no consistent pattern across the four analysed tephra.

- Tephra 1 shows a range in the > 150 μm sediment of 10.3% which culminates in a peak at 1438 cm. This tephra is 3 cm deeper than the ITRAX XRF proxy data suggests (Figure 5.5.1a). However, when the XRF proxy data was examined at this deeper depth, no significant change in tephra proxy elements was found. The 150-125 μm sediment displayed a more muted pattern, ranging from 0.05-0.80% and showing a flat topped peak between 1436-1438 cm.

- Tephra 2 displays the most idealised grainsize graph with a major peak in both the $150-125$ μm and the > 150 μm sediment, centred on the XRF suggested tephra depth. The $150-125$ μm fraction increases from 0.67% to 3.08% at 1345 cm before dropping to 0.42% at 1346 cm which suggests that the XRF data managed to capture the maximum peak in tephra before malfunctioning at 1346 cm (Figure 5.5.1b).

- Tephra 3 shows minimal variation in grainsize%, with no variation in the samples either side of the tephra. There is a small peak in both the $150-125$ μm fraction and the > 150 μm fraction 4cm prior to the (XRF defined) tephra, but this does not appear to be significant, >1.75%(Figure 5.5.1c).

- Tephra 4 shows a slight dip in both grainsizes at 983 cm, which is the depth at which the ITRAX data suggests tephra 4 is located. There is a small deviation from this v shaped pattern at 982 cm where the $150-125$ μm fraction jumps slightly however, this is a change of only 0.02% (Figure 5.5.1d).

The lack of consistency in grainsize distributions between tephra, and small range in grainsize % across the tephra 2, 3 and 4 (2.8, 1.75 and 0.77% respectively in the > 150 μm sediment), suggests this is an ineffective method for measuring glass concentration (Figure 5.5.1). Other approaches for quantifying glass shard concentrations, such as physically separating glass shards or liquid density separation, were considered however, due to the time involved with these methods and the modest role the tephra play in the overall scope of this project, further analysis was deemed unnecessary.

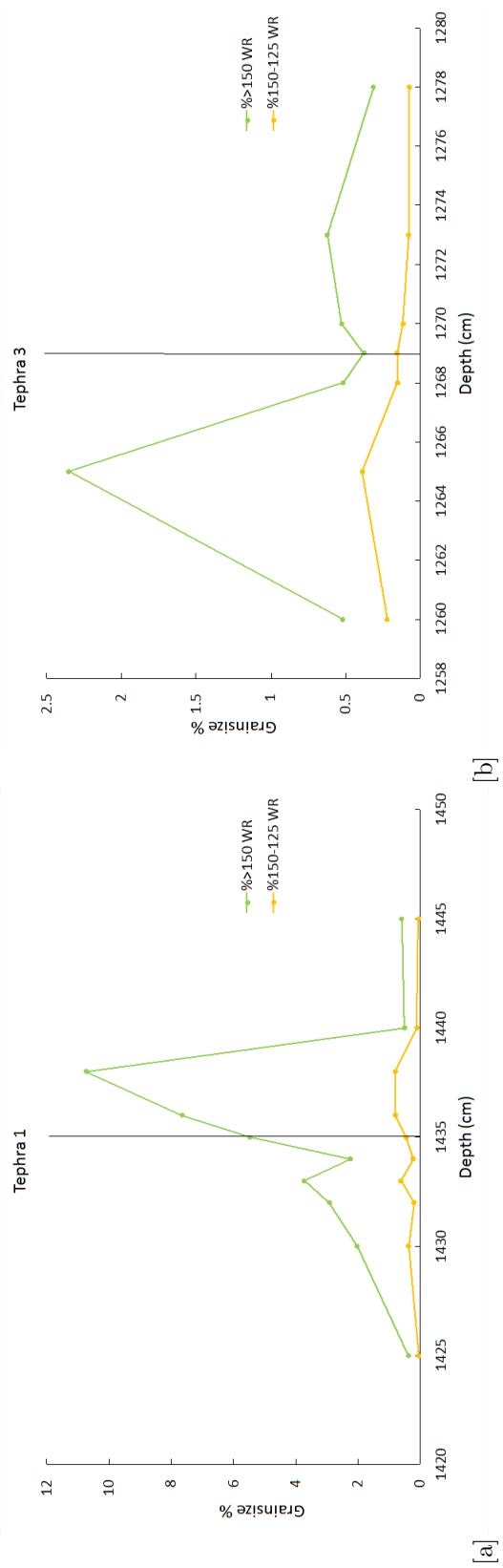

Figure 5.5.1: Grainsize variations near tephra locations. The black line marks the XRF implied location of the tephra based on elemental cps.

5.5.2 Electron microprobe

Major element data for tephra erupted during MIS3 have been used to distinguish specific tephra by comparing CaO wt% to K_2O wt% (Horrocks et al., 2000; Ryan et al., 2012; Shane et al., 2006), FeO wt% (Allan et al., 2008; Horrocks et al., 2000; Ryan et al., 2012; Smith and Shane, 2002; Smith et al., 2002), or SiO_2 wt% (Allan et al., 2008; Holt et al., 2014; Smith et al., 2002). Comparisons between the wt % of these major elements shows the glass shards from tephras 1-4 form three main clusters, centred on glass shards from tephras 1, 2 and 4 (Figure 5.5.2). The glass shards from tephra 3 do not form a distinct group but are instead comprised of shards which contain a mixture of chemical compositions from the other three tephra. This sample was therefore removed from consideration as a distinct cryptotephra layer within core MD97-2121 as it is likely reworked tephra from upslope.

When the average glass shard composition of tephra 1, 2 and 4 are plotted against published major element compositions of tephra erupted during MIS3, it is apparent that neither the Maketu nor the Hauparu tephra are represented in these glass shard compositions as they contain distinct major element signatures (Figure 5.5.3).

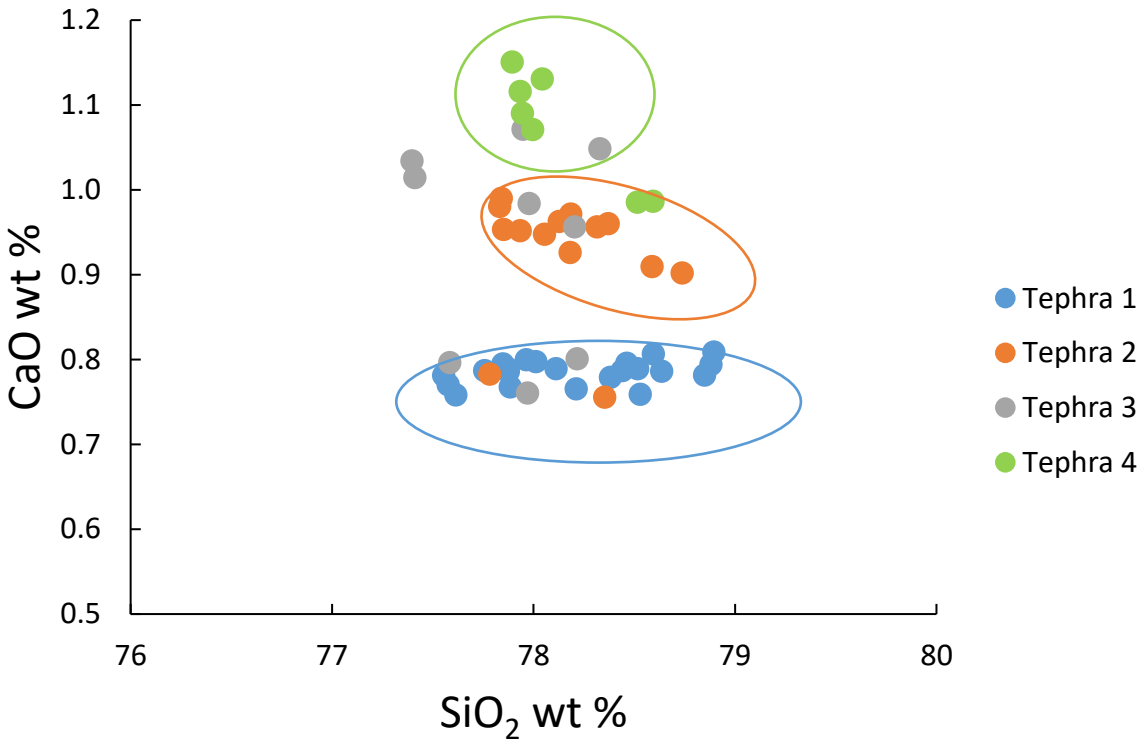

Figure 5.5.2: EMP CaO and SiO_2 wt % from glass shards. Tephra 1 = blue, tephra 2 = red, tephra 3 = gray, and tephra 4 = green.

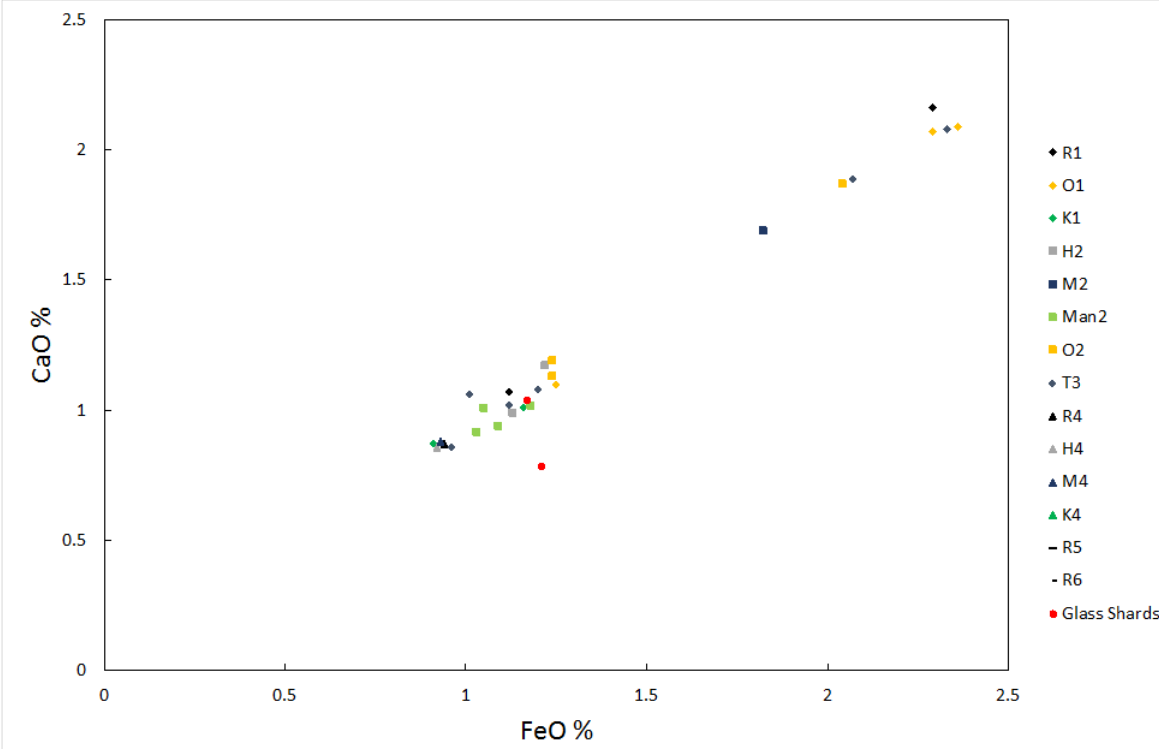

Figure 5.5.3: Major element analysis of glass shards erupted during MIS3. Tephra are defined by both colour and letter; R=Rotoehu, T=Tahuna, H=Hauparu, M=Maketu, Man=Mangaone, O=Omataroa and K=Kawakawa. The numbers define the studies the major element composition of glass shards was taken from; 1=Allan et al. (2008), 2=Smith et al. (2002), 3=Smith and Shane (2002), 4=Shane et al. (2006), 5=Horrocks et al. (2000) and 6=Alloway et al. (1994)

None of the shards analysed lay perfectly within the established range of any single tephra. Tephra 1 is closest in major element composition to the Rotoehu tephra but displays very little direct overlap. Although the SiO_2 wt % plot within the Rotoehu SiO_2 range, tephra 1 has a slightly lower CaO wt % (0.78 vs 0.86) (Figure 5.5.4). When the standard deviation (σ) of tephra 1 (see appendix 1) and the Rotoehu tephra (Allan et al., 2008; Alloway et al., 1994; Horrocks et al., 2000; Shane et al., 2006) are considered, however, there is some overlap in both CaO wt % and K_2O.

Tephra 2 is closest in major element composition to the Tahuna tephra. Like tephra 1, tephra 2 major element weight percentages lie slightly outside the values of the associated tephra with slightly higher SiO_2 wt % although this lies within the uncertainty constraints of the Tahuna tephra (Smith and Shane, 2002).

Tephra 4 is similar in composition to both the Omataroa and the Kawakawa tephra. It has similar weight percentages to both tephra in CaO however, like tephra 2, it has slightly higher SiO_2 wt % (77.96) than that of the Kawakawa (Allan et al., 2008; Shane et al., 2006) and Omataroa (Allan et al., 2008; Smith et al., 2002) tephra (77.60 and 77.40 respectively), although it does remain within σ.

Based on these elemental data and given the age ranges provided by the initial age model (Section 5.7), it is assumed that tephra 1 is the Rotoehu, tephra 2 is the Tahuna, and tephra 4 is the Kawakawa tephra. However, further research into the trace element compositions of these glass

shards is needed to confirm the identification of these tephra.

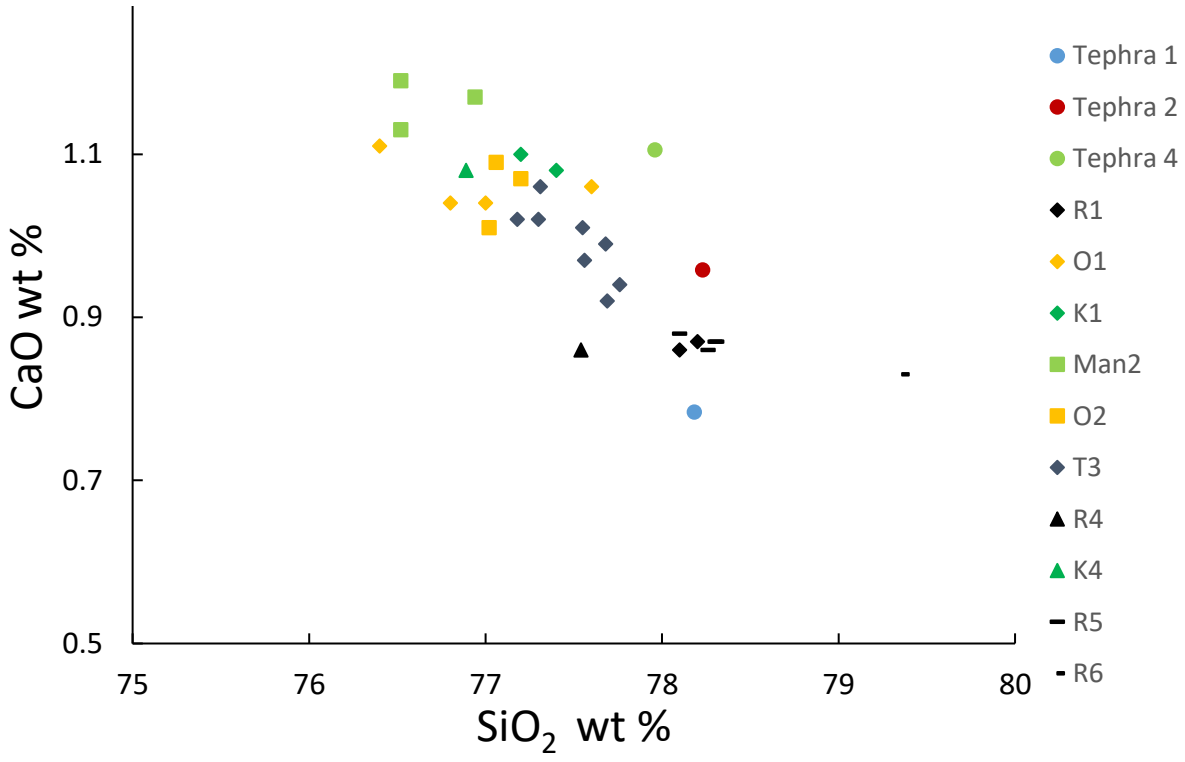

Figure 5.5.4: Major element composition of tephra 1, 2, 3 and 4 using SiO_2 vs CaO wt %. R=Rotoehu, T=Tahuna, H=Hauparu, M=Maketu, Man=Mangaone, O=Omataroa and K=Kawakawa. 1=Allan et al. (2008), 2=Smith et al. (2002), 3=Smith and Shane (2002), 4=Shane et al. (2006), 5=Horrocks et al. (2000) and 6=Alloway et al. (1994)

5.6 Radiocarbon

All calibrated dates for TAN1106-28 were in chronological order. They range from 24.3-46.16 ka and have low modelled errors (Table 5.2).

Depth (cm)	^{14}C (yrs BP)	Error (yrs BP)	Calibrated age (ka)	Modelled age (ka)	Modelled error (ka)
133-134	20920	70	24.24	24.3	0.35
175-176	22900	80	26.40	26.44	0.33
218-219	26440	100	29.82	29.95	0.39
243-244	29450	120	32.66	32.92	0.43
255-256	30170	120	33.49	33.69	0.29
273-274	32660	160	37.74	35.89	0.35
283-284	35130	140	38.83	38.88	0.40
313-314	40930	330	43.76	48.84	0.41
330-331	43730	400	46.16	46.16	0.48

Table 5.2: Radiocarbon dates run for TAN1106-28

For MD97-2121, calibrated radiocarbon dates from this study range from 29.14-46.19 ka. However, these radiocarbon dates were not in chronological order, with depths 1346-1347 cm and 1432-1433 cm containing earlier calibrated dates then deeper samples within the core (Table 5.3). This suggests there might be some form of error associated with these dates.

Depth (cm)	^{14}C (yrs BP)	Error (yrs BP)	Calibrated age (ka)	Modelled age (ka)	Modelled error (ka)
1085-1086	25500	100	28.75	29.14	0.19
1195-1196	29810	140	33.10	33.64	0.29
1268-1269	31500	140	34.64	34.96	0.17
1344-1345	32160	140	35.27	35.80	0.19
1346-1347	37940	230	41.63	35.90	1.22
1395-1396	33120	150	36.25	36.75	0.45
1432-1433	40010	250	43.02	42.55	0.35
1434-1435	38660	260	42.14	42.56	0.25
1490-1491	43500	330	45.94	46.19	0.41

Table 5.3: Radiocarbon dates run for MD97-2121

5.7 Age Model and Mass Accumulation Rates

Age models for TAN1106-28 and MD97-2121 were developed using radiocarbon dates, tie points from tephra layers and distinct isotope events seen in the CAICR (Pedro pers comm.). For TAN1106-28, radiocarbon dates were also taken from Bostock et al. (2015) for earlier sections of core, and for MD97-2121 they were taken from Carter et al. (2008). These age models were then used to calculate linear sedimentation and MARs for both cores.

The MAR of $CaCO_3$ within a sample reflects the volume (g/cm^2) of carbonate per thousand years (kyr) irrespective of any dilution effects. It is described by the equation

$$CaCO_3\ MAR\ =\ LSR \times DBD\ (CaCO_3\%/100)$$

, where LSR is the linear sedimentation rate, and DBD is the dry bulk density. Dry bulk densities for MD97-2121 were extrapolated from the dry bulk densities used in Carter and Manighetti (2006). However, as there is no published DBD data for TAN1106-28, a value of 1 was used following the findings of Carter et al. (2000) who derived a relationship between $CaCO_3$ % and DBD using a selection of marine sediment cores from the SW Pacific.

TAN1106-28

In TAN1106-28, OxCal was modelled to give age estimates for every cm of core. These age estimates were calibrated using 9 radiocarbon dates in the construction of an age model for the upper 455-100 cm of core. Radiocarbon dates were selected between 330-100 cm, 46.16 ka to 21.06 ka, and this trend was then extrapolated by OxCal to extend to 455cm (63.54 ka) (Figure 5.7.1). There were no tie points in the lower section of core, between 330-455 cm (46.16-63.54 ka) as this is the end limit of radiocarbon dating, and therefore the uncertainty in this section of core is the largest (Figure 5.7.1).

Overall the sedimentation rate within TAN1106-28 is uniform, averaging 8.99 cm/kyr throughout most the core. However, there is one small deviation between 19.2-34 ka where sedimentation rates increase to 25.27 cm/kyr, peaking at 19.64 ka (Figure 5.7.2a). During MIS3 the linear sedimentation rate begins at 7.16 cm/kyr at the MIS4/3 transition, and remains stable till 34 ka when sedimentation rates begin to increase heading into the 19.64 ka peak (Figure 5.7.2b). This stability at the beginning of MIS3 is likely the result of a lack of tie points in this section of core (Figure 5.7.1). Care must therefore be taken with this interpretation as fluctuations in the linear sedimentation rate could be masked by the lack of tie points.

$CaCO_3$ MARs in TAN1106-28, range from 4.26-0.28 g/cm^2/kyr during MIS3 (Figure 5.7.2b). These MARs show considerable variation and mainly reflect $CaCO_3$ % changes (Figure 5.7.2c and 5.7.2d).

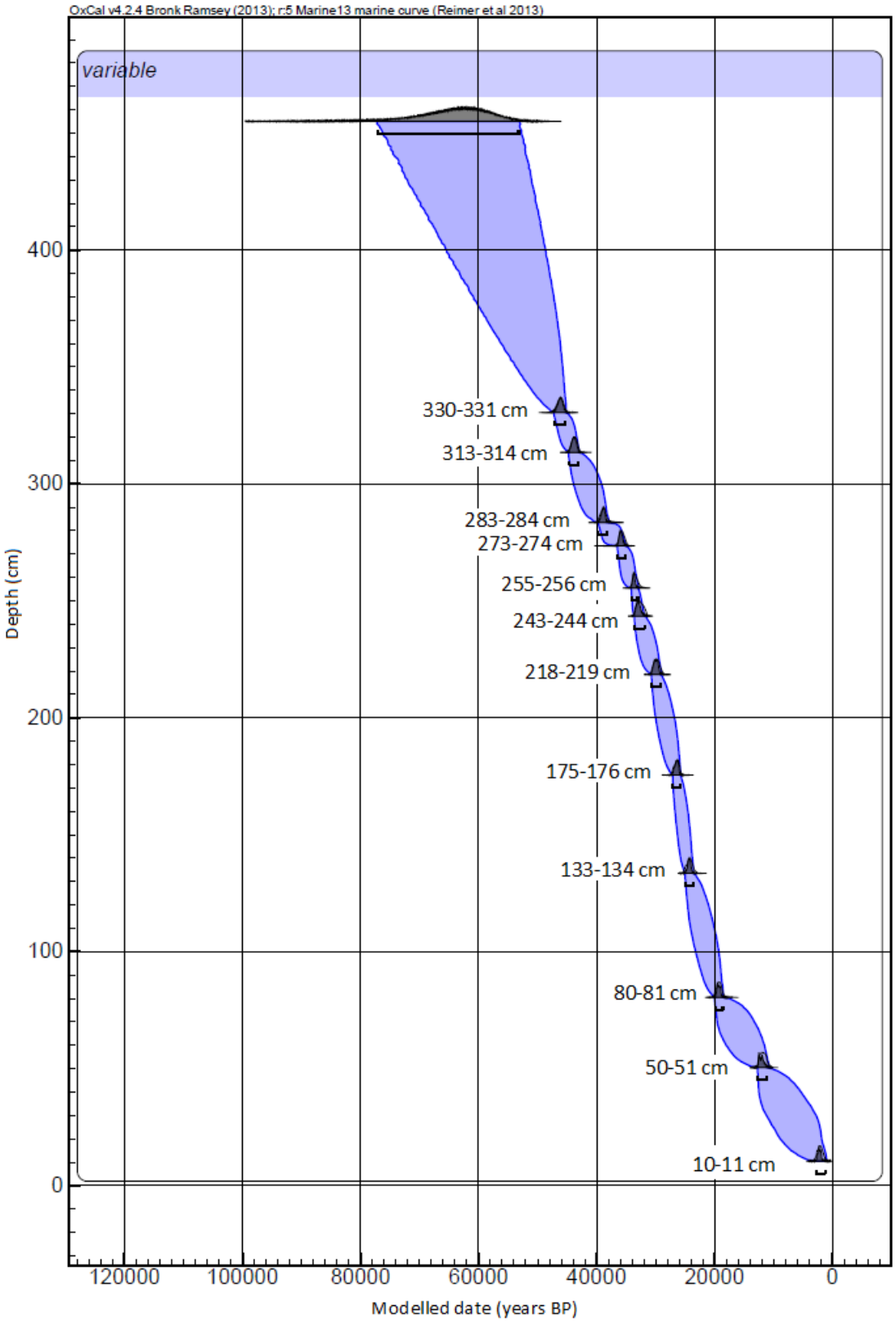

Figure 5.7.1: OxCal age model for TAN1106-28. The shaded blue area shows the 95% confidence interval, the dark curve distrubtion curve shows the modelled calibrated age

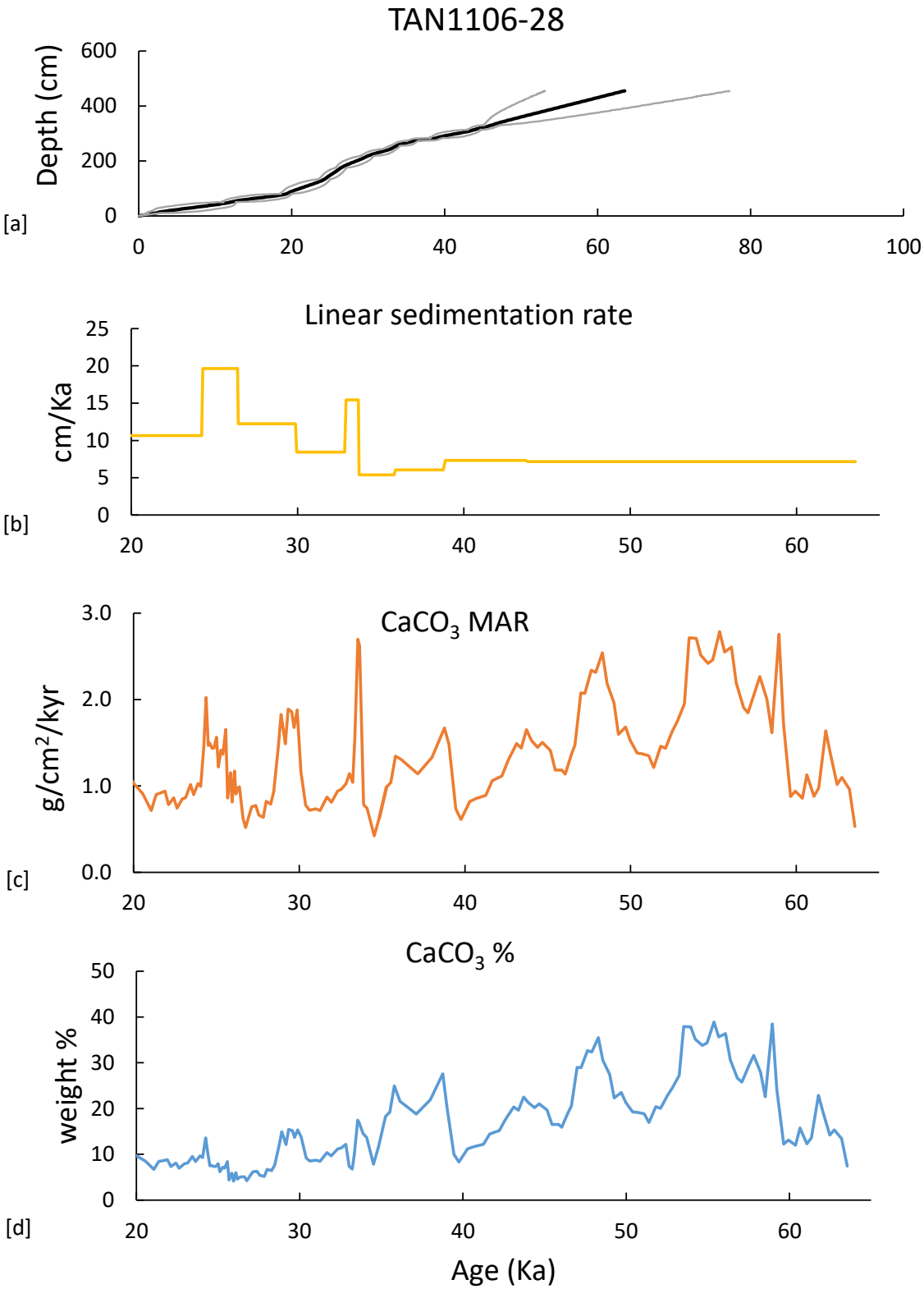

Figure 5.7.2: TAN1106-28 sedimentation and MAR. [a] = age depth model, the black profile shows the OxCal generated median age and the grey lines annotate 95% confidence interval [b] = linear sedimentation rate, [c] = $CaCO_3$ MAR, [d] = $CaCO_3$ %

MD97-2121

The OxCal model output was adjusted to calculate age estimates for every 50 cm of core and at the depths which contained cryptotephra deposits (see appendicx 2). Tephra 1, at 1434 cm, gave a median calibrated age of 42.47±0.31 ka which places it within the age constraints of the Rotoehu tephra (45.1±4 ka (Danisik et al., 2012)). As glass shards analysed at this depth had the closest major element composition to the Rotoehu tephra (Figure 5.5.4,) this strongly suggests that tephra 1 is the Rotoehu cryptotephra. Tephra 2, at 1345 cm, gave a median calibrated age of 35.9±1.25 ka which places it within the age range of the Tahuna (39.3±2.4 ka), the Hauparu (38.5±2.5 ka) and the Maketu tephras (36.3±1.2 ka (Froggatt and Lowe 1990 as modified by Holt et al. 2014). As major element composition of both the Maketu and Hauparu tephra are distinct from glass shard major element compositions found within MD97-2121 (see Section 5.5.2), it is likely that tephra 2 is the Tahuna tephra, although the age of tephra 2 is at the limit of the age uncertainty for the Tahuna tephra.

The OxCal model was then rerun using the Gregorian calibrated age of the Rotoehu tephra, -43150±4000 yrs (modified from Danisik et al. 2012), and Tahuna tephra, -37350±2400 yrs (modified from Holt et al. 2014) at 1434 and 1345 cm, respectively (Figure 5.7.3). The addition of these tephra tie points helped better constrain the age model in a section of core that had considerable uncertainty as it reaches the limit of radiocarbon dating (see appendix 2 for outlier model). Tephra 4 had been identified as the Kawakawa tephra by Carter et al. (2008) and was included as such throughout the model runs.

There is considerable uncertainty in the older section of MIS3, from 1490-1800 cm, as it is not as well constrained as younger sections of core. This is because ages at these depths are beyond the limits of radiocarbon dating ($\approx$ 50 ka) and, excluding the drop in isotopes at MIS4, there are no distinct δ^{18}O peaks within MD97-2121 which can be correlated to the benthic LR04 stack (Lisiecki and Raymo, 2005) or the CAICR (Pedro pers comm.) to provide additional tie points.

The sedimentation rate was relatively constant through the upper 1850 cm of MD97-2121 (<60 ka) with the only deviation being an increase in sedimentation rate between 37.5-33.7 ka (Figure 5.7.4a). During MIS3 linear sedimentation rates range from 134.0-6.7 cm^2/kyr with a sharp peak at 35.83 ka (Figure 5.7.4b) This peak overwhelms the $CaCO_3$ MAR signal and it is therefore difficult to pick out any millennial scale trends (Figure 5.7.4). $CaCO_3$ MAR are moderate to low, ranging from 15.9 cm^2/kyr to 0.9 cm^2/kyr (Figure 5.7.4c), and do not show the millennial scale events found in TAN1106-28, and have very little correlation with $CaCO_3$ % (Figure 5.7.4d).

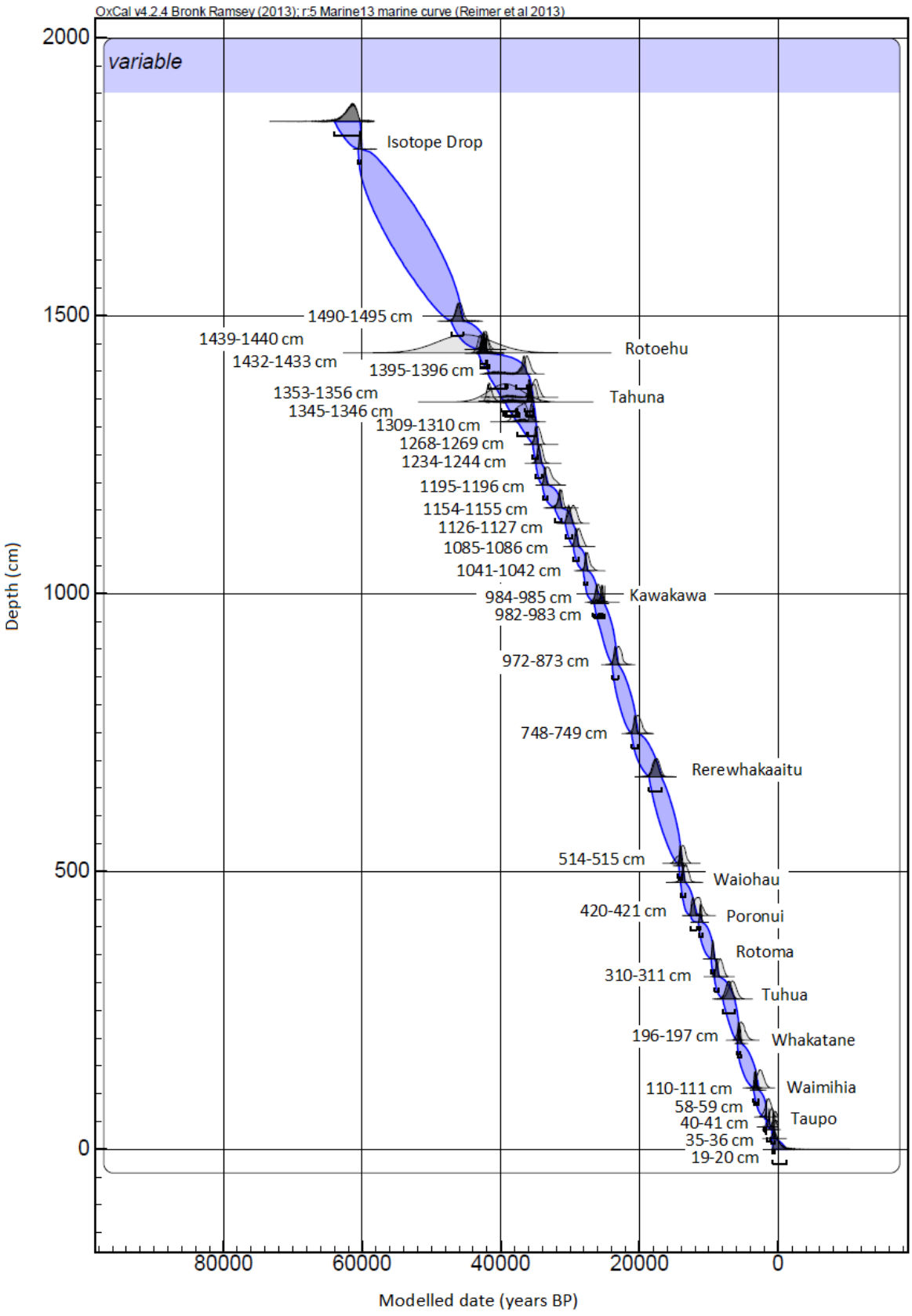

Figure 5.7.3: Oxcal age model for MD97-2121 developed using radiocarbon dates and tephra depths taken from Carter et al. (2008). Calibrated tephra dates were developed by Lowe et al. (2013) for all tephra bar the Kawakawa which was dated by Vandergoes et al. (2013). The shaded blue area shows a 95% confidence interval, the dark distribution curve shows the modelled calibrated age and the light grey distribution curve shows the original calibrated date.

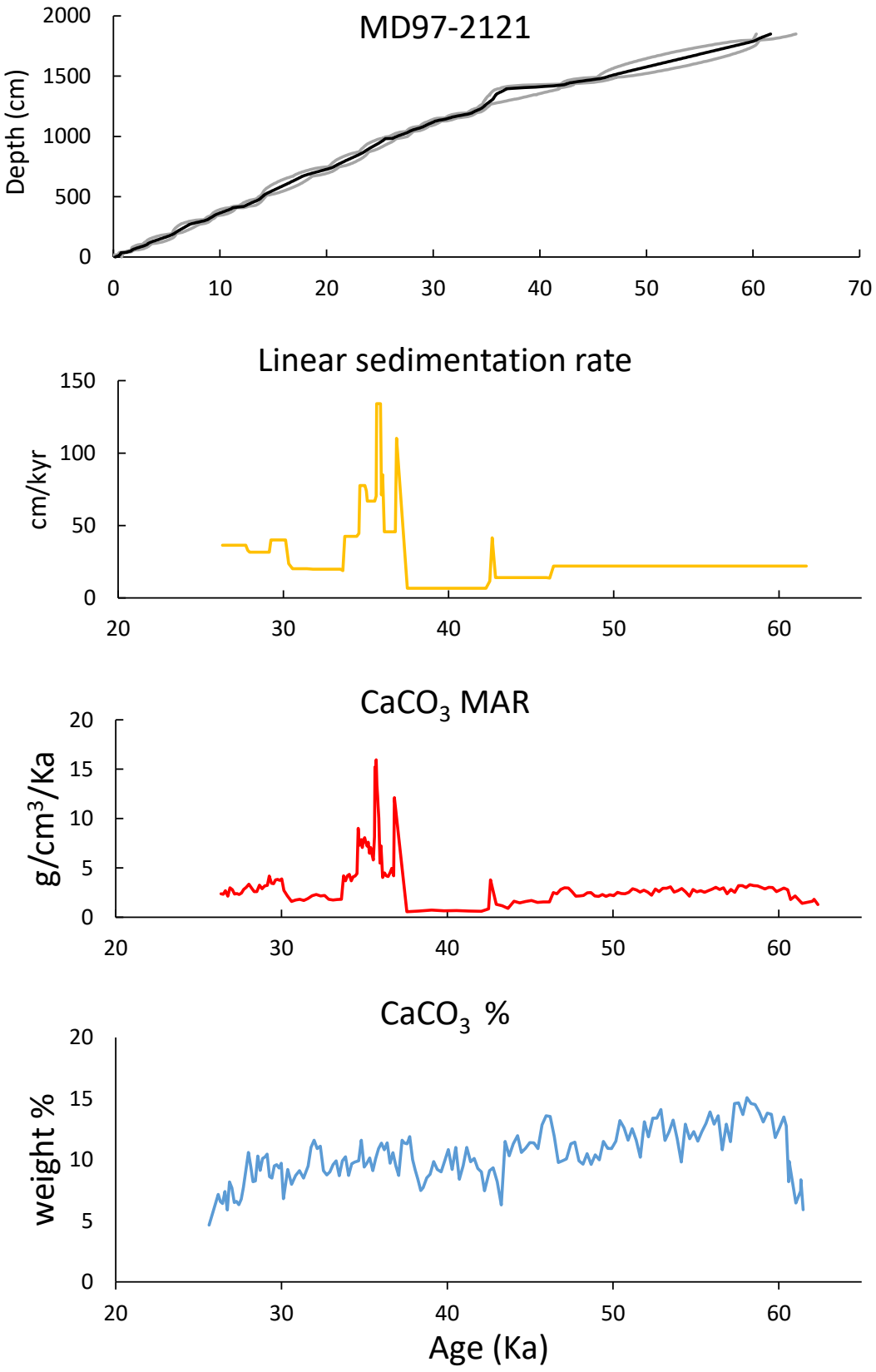

Figure 5.7.4: MD97-2121 sedimentation and MARs. [a] = age depth model, the black profile shows the OxCal generated median age and the grey lines annotate 95% confidence interval [b] = linear sedimentation rate, [c] = $CaCO_3$ MAR, [d] = $CaCO_3$ %

6 Discussion

While a few marine data sets of suitable resolution exist for this region, little has been published about MIS3 in the SW Pacific. Using data from Section 5, a high-resolution ocean/climate record has been reconstructed for MIS3 in the New Zealand region of the SW Pacific. These results are used to investigate the primary aim of this thesis, which is to find evidence for millennial scale events in both productivity and terrigenous variability across the STF. To extract the millennial scale signal, high-resolution marine sediment core data from TAN1106-28 and MD97-2121 will be analysed. This will enable the investigation into the processes influencing MIS3 climate variability at the two sites including variations in ocean current systems, nutrient and light availability, SST and sea level change. These two ocean/climate records will then be compared and contrasted with each other to assess the influence of Antarctic millennial scale events across the STF. This understanding of SW Pacific climate variability will then be compared with Southern Ocean marine sediment records to develop a better understanding of the broader processes and mechanisms potentially driving millennial scale variation during MIS3 in the Southern Hemisphere.

6.1 Sediment core TAN1106-28

6.1.1 Millennial scale events

To develop the resolution needed to investigate millennial scale climate variability, considerable effort has been put into developing an age model for TAN1106-28 during MIS3. Nine radiocarbon samples were used for the construction of this age model however, due to a lack of tie points between 330-455cm, this section of core is still poorly constrained (Figure 5.7.1). Tie points could be obtained through the association of peaks in TAN1106-28 with AIM events in the CAICR (Pedro pers comm.) however, as one of the primary aims of this thesis is to identify AIM events in TAN1106-28, this would limit the legitimacy of any AIM events identified in this section of core. This could, however, be used to constrain the age model for this core in additional studies unrelated to the investigation of Antarctic millennial scale events.

MIS3 millennial scale events can be identified in TAN1106-28 through variations in $CaCO_3$, grain-size, and ITRAX XRF elements (Figure 5.4.6). These events show the most marked change at the MIS4-MIS3 transition, and decrease in magnitude towards the MIS2 glacial. The millennial scale events within TAN1106-28 also show a strong correlation with the timing of AIM events in the CAICR. This can be identified through similarities in the shape, duration and timing of TAN1106-28 proxies in comparison to the CAICR $\delta^{18}O$ values (Figure 5.4.6). The identification of AIM events across multiple proxies shows that the AIM signal is recorded at the site of TAN1106-28.

The time period covered by MIS3 also contains Heinrich events 5a, 5, 4 and 3 (Rasmussen et al., 2016), which coincide with the timing of AIM events 14, 12, 8 and 4 respectively (Figure 6.1.3) and show periods of increased productivity at the site of TAN1106-28. Increased productivity during Heinrich events is also found at the site of MD97-2120 which shows increased alkenone abundances during the Younger Dryas and Heinrich events 1-6 (Sachs and Anderson, 2005). However, it is

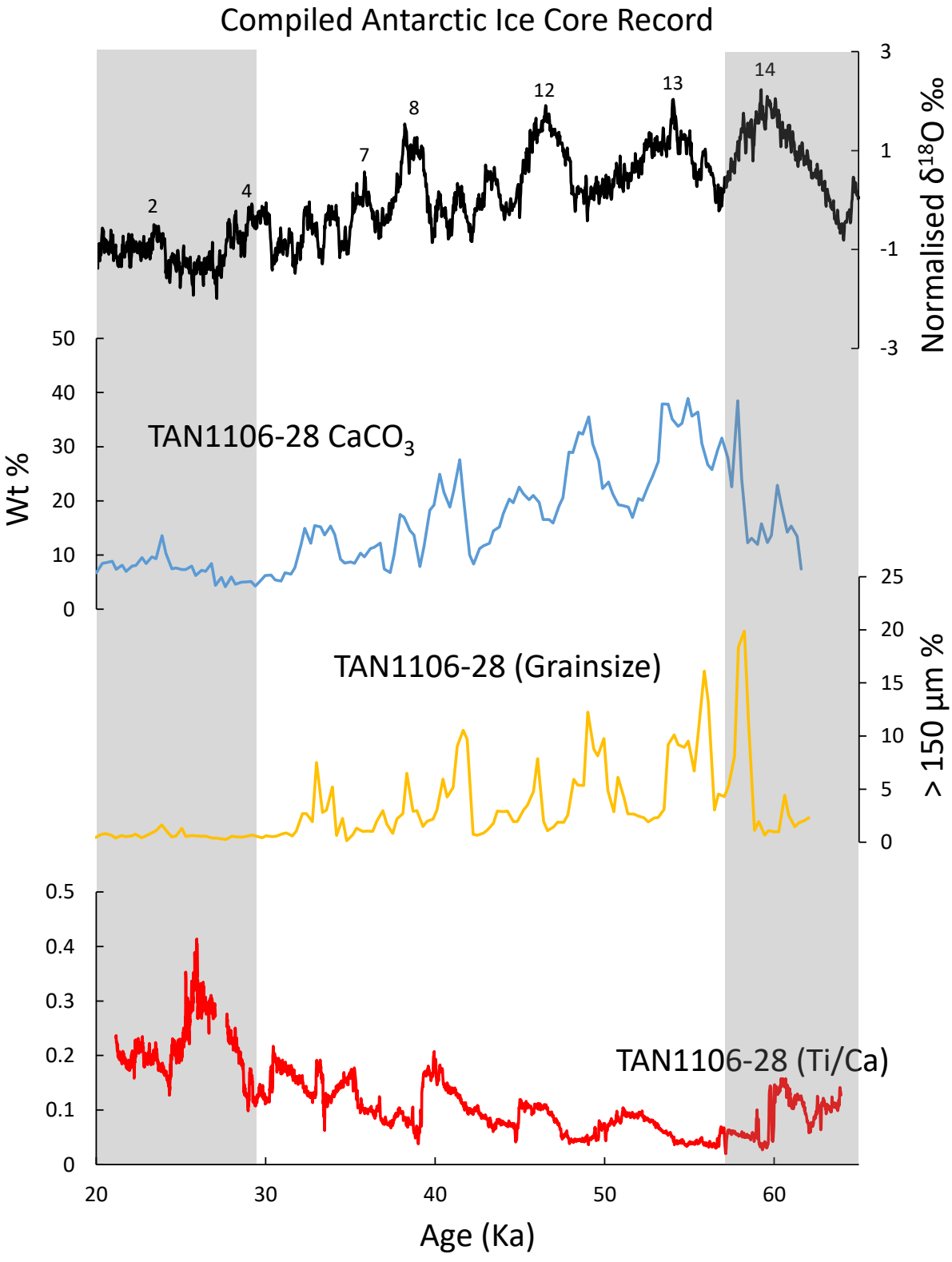

Figure 6.1.1: Multiproxy millennial scale events recorded in TAN1106-28. Black shows the CAICR (Pedro pers comm.), Blue shows $CaCO_3$ % and due to the close correlation with Ca (Section 5.4), also reflects Ca variations, yellow shows grainsize variations, red shows ITRAX terrigenous variability and the non shaded area shows MIS3

difficult to separate the Heinrich signal from the Antarctic signal within TAN1106-28 as AIM events 13, 7, 6, 5 and 2 may also be recorded in the productivity signal (Figure 6.1.3). This suggests that TAN1106-28 is predominantly influenced by Antarctic climate variation, rather then Northern Atlantic Heinrich events.

6.1.2 Sedimentation rate and terrigenous input variation

Sedimentation rates in TAN1106-28 increase towards the end of MIS3 and peak between 24.37-26.39 ka (Figure 5.7.2b). As the LGM occurred 23-18 ka (Bostock et al., 2013), it is likely that this increase in sedimentation rate reflects the transition into a cooler climate and may be a response to harsher climate conditions and/or glacio-eustatic sea level change.

In the New Zealand region sedimentation rates increased during the LGM (Carter and Manighetti, 2006). This was the result of enhanced erosion due to reduced vegetation cover, stronger winds, increased glacial erosion, and a reduction of sediment trapped in glacial lakes and streams (Carter et al., 2000; Griggs et al., 1983; Kowalski and Meyers, 1997). Eustatic sea levels were 120 m lower during the LGM. This increased the area of erodible land along the continental margin, and enabled major river systems to flow across the emergent shelf and discharge sediment at the shelf edge which resulted in a greater transport of terrigenous sediment to the deep ocean (Carter et al., 2000; Carter and Manighetti, 2006; Griggs et al., 1983; Kowalski and Meyers, 1997).

Glacial-eustatic sea level fluctuations during the last 140 ka have been tied to MAR variability within MD97-2121 (Carter and Manighetti, 2006). This record shows that during the MIS2 low stand, MARs increased. However, the increase in terrigenous supply to offshore marine sediment cores is not consistent across all glacials, and MARs during MIS2 were significantly higher than MIS4 (Carter and Manighetti, 2006). This was attributed to variations in sea levels between the two glacial periods. During MIS4 sea levels were 45 m below present, 75 m higher then the LGM. It is theorised that this variation in sea level allowed the development of along shelf currents which transported sediment along the east coast, restricting supply to the deep ocean (Carter and Manighetti, 2006). Although the response to sea level fluctuations varies regionally, it is likely that similar processes may have influenced terrigenous accumulation at core site TAN1106-28.

The MIS2 glacial resulted in increased discharge off the southern South Island, and through the Solander Trough to the site of TAN1106-28 (Carter et al., 2000). During the cool climate conditions of MIS3, it is likely that a similar, but less dynamic, process worked to bring sediment to the site of TAN1106-28 and this may be one of the mechanisms behind increased sedimentation during MIS3 in comparison to the warmer Holocene (Figure 5.7.1). However, the eustatic sea level during MIS3 was 60-80 m below present, and 60-40 m higher than the Last Glacial Maximum (LGM) (Siddall et al., 2008), which means sediment may have remained trapped on the shelf by along shore currents in a similar mechanism to that theorised by Carter and Manighetti (2006) to account for reduced MARs during MIS4.

The variations in the sedimentation rate of TAN1106-28 are reproduced in the terrigenous MAR which contains the same peak accumulation event at 24.37-25.39 ka (Figure 5.7.2b). As this variation deviates significantly from $CaCO_3$ MARs, this suggests that terrigenous MARs are the dominant control on the linear sedimentation rate within TAN1106-28. Superimposed on the trend of increasing terrigenous accumulation towards the end of MIS3, is a series of small, millennial scale

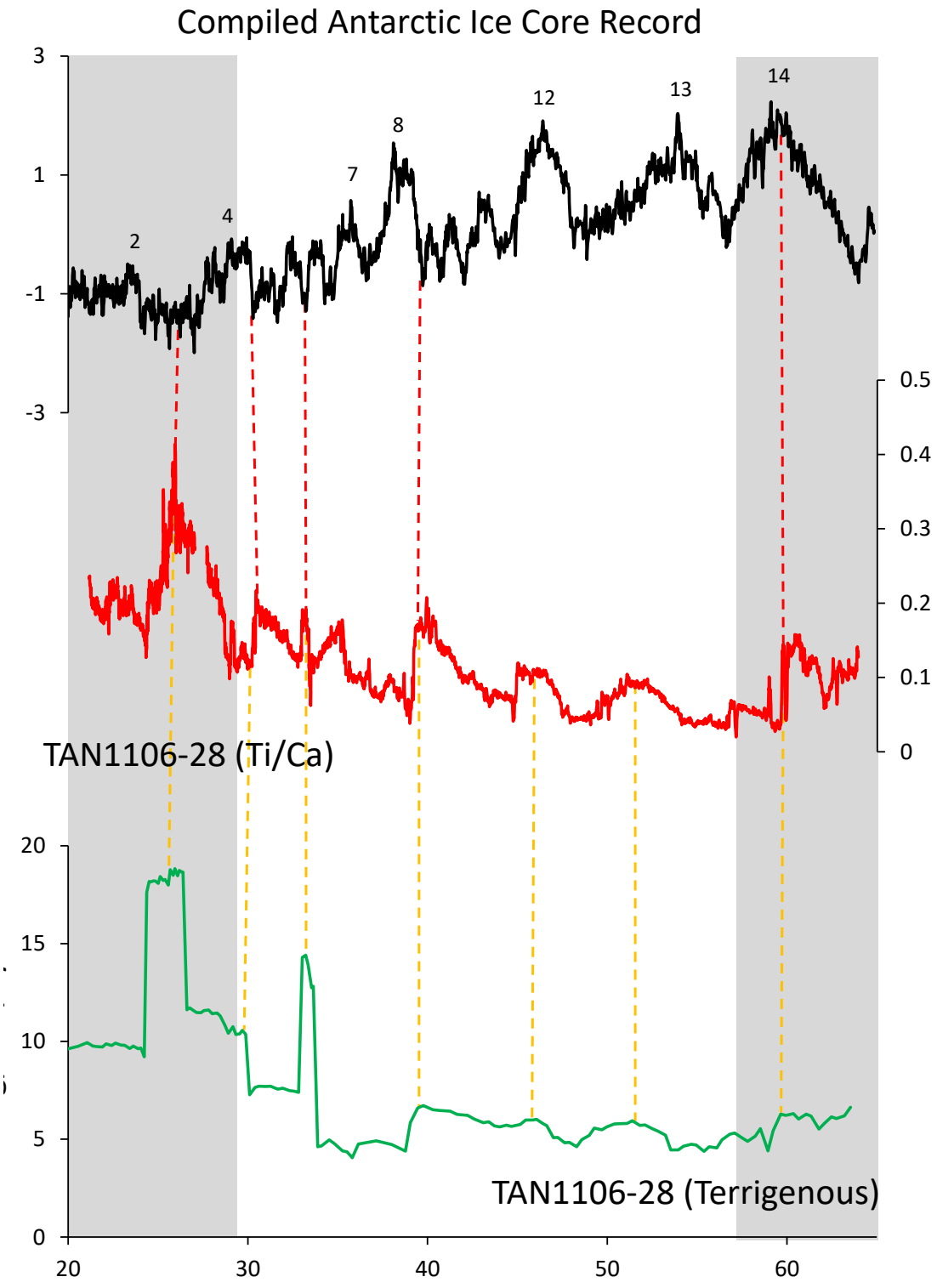

Figure 6.1.2: AIM events and terrigenous fluxes in TAN1106-28. The black profile shows δ^{18}O variations in the CAICR (Pedro pers comm.), the red profile shows the ITRAX Ti/Ca ratio in TAN1106-28, and the green profile shows terrigenous MARs in TAN1106-28. AIM events are numbered according to (Rasmussen et al., 2016). The dashed red line links AIM events to anti-phased events in the ITRAX terrigenous data, the dashed yellow line shows the correlation between the ITRAX terrigenous record and the MAR record and the non shaded area shows MIS3

fluctuations with an anomalously large fluctuation at ≈ 33 ka, likely an age model artefact (Figure 5.7.2b). These fluctuations are recorded in both terrigenous MAR and ITRAX terrigenous proxies (Figure 6.1.2), however, discounting the ≈ 33 ka peak, they are more pronounced in ITRAX terrigenous proxies (Fe, Ti and Ti/Ca), which might be due to the higher resolution of the ITRAX data (Figure 6.1.2).

Millennial scale peaks in Ti/Ca show a saw tooth pattern that appears to oppose the shape of AIM events recorded in the CAICR (Pedro pers comm.). However, although the timing of these peaks is anti-phased in the later half of MIS3, this signal is more muted in early MIS3 in both the ITRAX proxies and terrigenous MARs (AIM events 12 and 13)(Figure 6.1.2). The dampening of terrigenous millennial scale events may be a response to sea level variations. Eustatic sea level reconstructions for MIS3 shows that sea levels drop from 60 m below present, to 80 m below present in the later half of MIS3 (Siddall et al., 2008). Therefore, the strengthening of the anti-phased relationship between terrigenous accumulation and AIM events could be a function of lowered sea levels. As sea levels lowered they could reach a threshold where sediment stored on the shelf is released into the deep ocean which may have contributed to the ≈ 33 ka peak in terrigenous MAR and resulted in increased discharge to the site of TAN1106-28 in the later half of MIS3. However, peaks in terrigenous MAR are influenced by the linear sedimentation rate. Therefore, the lack of tie points in early MIS3 may hide fluctuations in the linear sedimentation rate, which in turn may obscure variations in the terrigenous MARs. Thus, the muted terrigenous MAR signal in the early half of MIS3 may simply be a function of a lack of age constraints, and other peaks of the same magnitude as the ≈ 33 ka peak may be concealed by this lack of tie points. However, as this signal is also damped in early MIS3 ITRAX terrigenous proxies, this suggests sea level variations may have also contributed to the amplitude of millennial scale, terrigenous accumulation events during MIS3.

Variations in erosion rates may have also influenced terrigenous fluctuations during MIS3. The location of the Southern Alps between subpolar and polar air masses (with a small contribution from tropical atmospheric circulation), and its close proximity to major ocean fronts and currents, such as the STF, has resulted in a climate system that is vulnerable to change (Carter and Gammon, 2004). Millennial scale climate variability has been recorded in both Southern Alps erosion rates and glacial advance and retreat, and can be seen in the response of this climate system to the Younger Dryas (Doughty et al., 2013; Hajdas et al., 2006; Kaplan et al., 2010). The Younger Dryas is a Northern Hemisphere cooling event which is initiated in the NGRIP and GRIP Greenland ice-core records at ≈ 12.84 ka (Rasmussen et al., 2016). It has a duration of 1193 years (Rasmussen et al., 2016) and is expressed as a warming event in Antarctica. The bipolar response of the high latitudes, combined with the millennial scale duration of this event, makes the Younger Dryas a good analogy for the New Zealand terrestrial response to AIM events during MIS3. During the Younger Dryas, Kaipo Bog (Hajdas et al., 2006) in eastern North Island, and glacial moraines (Doughty et al., 2013; Kaplan et al., 2010) from the Irishman Basin in the central South Island (Figure 6.1.7), show warming events analogous with Antarctic and Southern Ocean climate records. This reflects the tight coupling between Antarctic climate variations and mid-latitude responses over New Zealand (Kaplan et al., 2010) and suggests that the terrigenous record might show similar millennial scale responses to AIM events during MIS3.

The terrigenous response to short term Antarctic climate variation is supported by the reconstruction of gamma ray emissions from ODP site 1119. Natural gamma radiation is interpreted to reflect fluctuations in clay content as a response to the waxing and waning of the South Island Ice

Cap, within the limitations of the age model (Carter and Gammon, 2004). Natural gamma radiation in core 1119 shows a strong correlation to the Vostok deuterium record in Antarctica, and, during MIS3, millennial scale events appear to occur in phase with deuterium fluctuations, though the resolution in this record is too low to correlate these fluctuations to specific AIM events. Thus, terrigenous variation during MIS3 is likely the response of both sea level variations, and glacial advance and retreat, the former affecting delivery of sediment to the middle shelf and beyond, and the latter affecting rates of erosion and fluvial delivery through the glacial overriding of lacustrine sediment traps.

6.1.3 Biological productivity during MIS3

Peaks in $CaCO_3$ % and ITRAX Ca, and Si/Ti are in phase (Figure 5.4.6), and reflect periods of increased biological productivity at the site of TAN1106-28. Biological productivity in ocean sediment is a measure of the abundance of both carbonate and biosiliceous organisms. Opal % (biogenic silica) was small for the upper (LGM to Holocene) section of TAN1106-28 (M. Kienast 2016 pers comm.) and was considered insignificant for MIS3. Therefore, we focus on $CaCO_3$ MARs to reconstruct productivity.

$CaCO_3$ reflects a combination of foraminifera and coccolithophore production, and as $CaCO_3$% is strongly correlated to $> 63\mu$m grainsize (Section 5.1.1), changes in $CaCO_3$% likely reflect variations in foraminifera rather than coccolithophore production (Broecker and Clark, 2009). Variations in $CaCO_3$ % can reflect changes in productivity, fluctuations in incoming terrigenous sediment, and/or $CaCO_3$ dissolution (Volat et al., 1980). Therefore, to extract the productivity signal both dilution and dissolution first need to be discounted. Incoming fluxes of terrigenous sediment dilute the $CaCO_3$ signal, lowering the $CaCO_3$ % without reflecting changes in productivity. To remove this dilution effect, $CaCO_3$ MARs were calculated. As the $CaCO_3$ MAR accounts for changes in linear sedimentation rates, they accurately represent $CaCO_3$ accumulation at the site of TAN1106-28. There is minimal variability between the $CaCO_3$ MAR and $CaCO_3$ % within TAN1106-28 which suggests that dilution had little influence on $CaCO_3$ % at the site of TAN1106-28 (Figure 5.7.2).

Dissolution within marine sediment cores can also distort the productivity signal. This can be measured using the fragmentation index (Le and Shackleton, 1992) however, this analysis was outside the scope of this study. TAN1106-28 was collected at 2798 m water depth. This is above the contemporary depth of both the foraminiferal lysocline, $\approx$ 3600 m water depth, and Calcium Compensation Depth (CCD), $\approx$ 4400 m depth (Bostock et al., 2011; Crundwell et al., 2008; Hayward et al., 2007). Both the CCD and the foraminiferal lysocline were likely shallower during MIS3. However, it has been suggested that the lysocline rose by $\approx$ 600 m during the last glacial Howard and Prell (1994), and the MIS3 lysocline is unlikely to have risen by more than this amount. Therefore, during MIS3 sediment at the site of TAN1106-28 would have been deposited above both the foraminiferal lysocline and the CCD. Numerous studies from SAW in the New Zealand region have shown that dissolution occurs above the foraminiferal lysocline, ($\approx$ 3600 m water depth) (Crundwell et al., 2008; Hayward et al., 2007; Kowalski and Meyers, 1997; Schaefer et al., 2005), at times of high productivity where the breakdown of organic carbon is hypothesised to have reduced the pH of the sea floor (Crundwell et al. 2008 and references therein).

$CaCO_3$ dissolution is also influenced by the presence of overlying oceanic current systems and, as TAN1106-28 sits in upper Circumpolar Deep Water (Bostock et al., 2011; Cobianchi et al.,

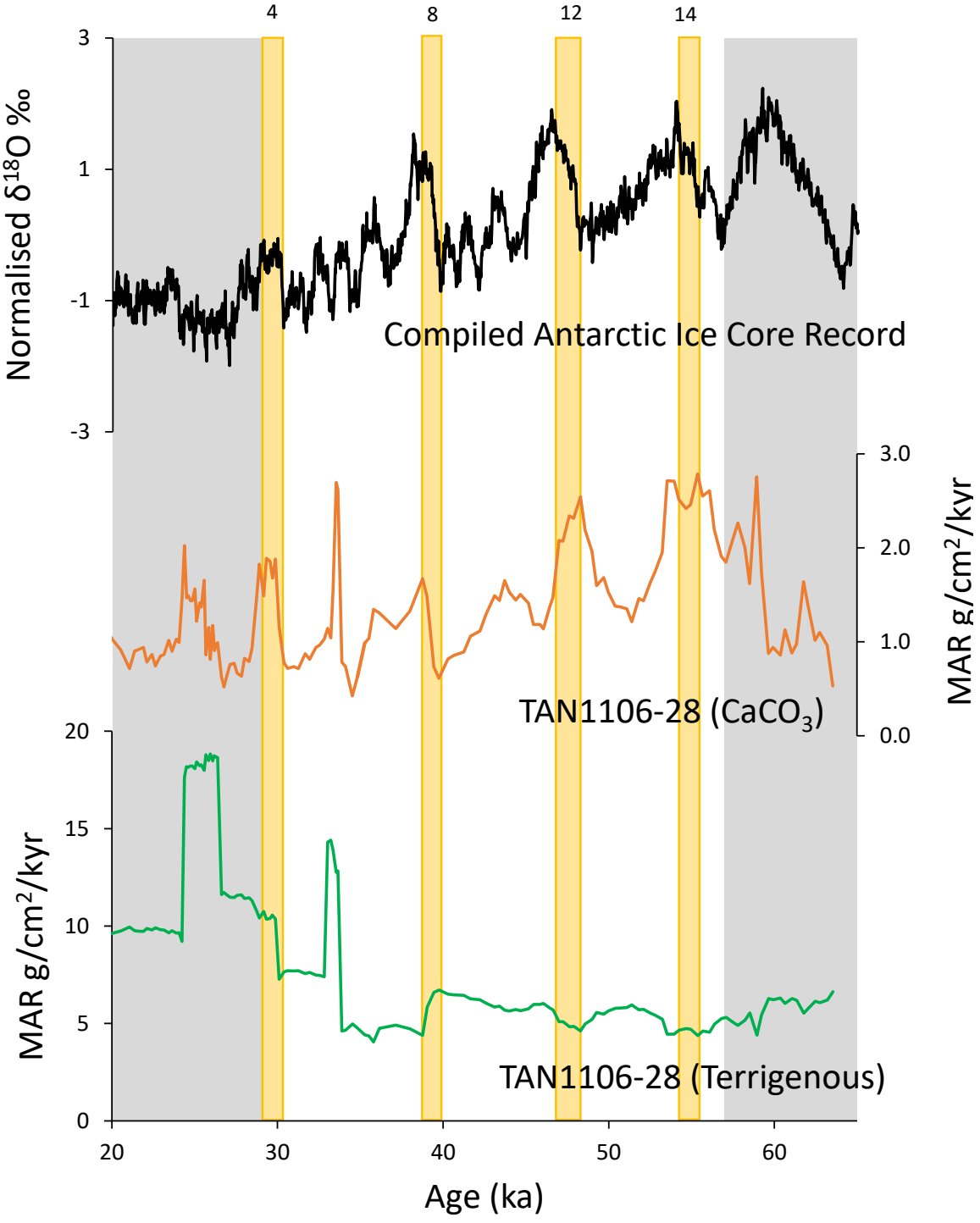

Figure 6.1.3: Comparison between MIS3 millennial scale events in the CAICR (Pedro pers comm.) and TAN1106-28 MARs. The black profile shows $\delta^{18}O$ variations in the CAICR (Pedro pers comm.), the red profile shows $CaCO_3$ variation in TAN1106-28, and the green profile shows terrigenous variations in TAN1106-28. The yellow shaded bars mark AIM events which are labelled at the top of each bar, and the non shaded area shows MIS3

2015), which, due to its older age contains more CO_2 and is slightly more corrosive than other deeper waters it is possible that dissolution was experienced at this site. However, reproducibility in the timing and scale of high productivity events between TAN1106-28 and other marine sediment records from SW New Zealand (Barrows et al., 2007), and south of the Campbell Plateau (Barrows et al., 2007; Kowalski and Meyers, 1997; Nelson et al., 1993) (Figure 6.1.4) suggests that the productivity signal during MIS3 is widespread and the result of ocean/climate events. This implies that the TAN1106-28 $CaCO_3$ signal is not likely to be a manifestation of dissolution variability at this site.

Within the constraints of the age model (see Section 6.1.1) many $CaCO_3$ MAR peaks show a similar timing to AIM events (Figure 6.1.3). Unlike terrigenous MARs, they show no significant variation heading into the MIS2 glacial and, aside from an anomalous peak at $\approx$ 33 ka, millennial scale events are of a similar magnitude throughout MIS3. The close correlation between the timing of AIM events and productivity peaks in TAN1106-28 suggests that during the millennial scale warming events in Antarctica, productivity increased in the SAW of the Solander Trough. As productivity is typically low in SAW, there must be a change in oceanic conditions to result in these periods of increased productivity.

The $\approx$ 33 ka peak is in phase with the corresponding terrigenous accumulation and linear sedimentation peak. This suggests this peak may be the result of a sudden accumulation of sediment. Radiograph images (see appendix 3) and grainsize analysis suggest this is unlikely to be a turbidite (Figure 5.1.1), and the OxCal outlier model (see appendix 2) shows no major outliers in TAN1106-28 radiocarbon dates suggesting this sudden change in linear sedimentation rate is not an age model artefact. However, the influx of sediment to the site of TAN1106-28 could be the result of sea level change. As sea levels are lowered heading into the MIS2 glaciation, a threshold may have been reached which allowed sediment previously trapped on the shelf to be deposited to the site of TAN1106-28, increasing both terrigenous and $CaCO_3$ MARs which may explain why this event does not appear to correspond to the $\delta^{18}O$ in the CAICR (Figure 6.1.3).

Productivity in SAW is primarily limited by the availability of iron, ocean temperatures and light (Graham et al., 2015; Maldonado et al., 2005; Martin, 1990). To overcome iron limitation during AIM events, iron may have been introduced to SAW via dust input, terrigenous fluxes (assuming the iron is in a bioavailable form and there is a proximal terrigenous source), or oceanic processes, such as interaction with trace element bearing STW, upwelling, or resuspension of sediment (Boyd et al. 2004 and references therein) by ocean front systems and boundary currents.

Increased glacial dust due to drier and winder climate conditions has been suggested as a driver of productivity in glacial SAW in the South Atlantic. This is enabled through the proximity of Southern Hemisphere continents which are an important source of iron rich terrigenous dust to SAW (Jaccard et al., 2013; Martínez-Garcia et al., 2011). Similar processes may have occurred in the SW Pacific to result in the millennial scale fluctuations of enhanced productivity at the site of TAN1106-28. However, in our ITRAX data, the dust proxies Fe and Ti (Rothwell and Croudace, 2015) show a negative correlation with the biogenic proxy Ca suggesting productivity at the site of TAN1106-28 was not driven by dust influxes (Figure 5.4.4). This is supported by dust measurements from ice core records in Antarctica which show low levels of dust within MIS3, and limited evidence for millennial scale variability (Figure 6.1.5). The lack of correlation between AIM events and dust influx in these cores suggests that productivity in SAW increases during MIS3

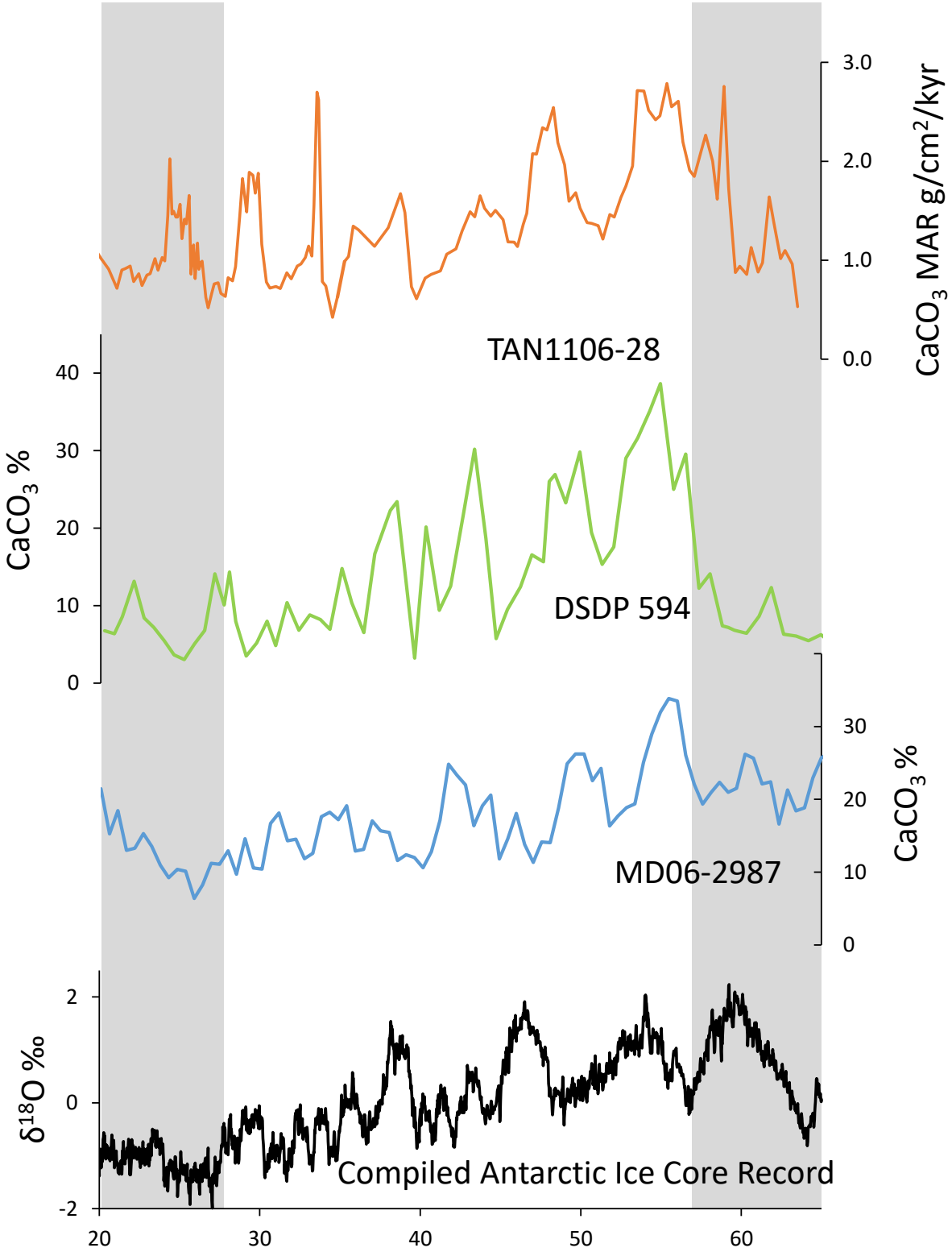

Figure 6.1.4: Comparison between productivity in southern New Zealand cores during MIS3 compared to AIM events. Red = $CaCO_3$ MAR from this study, green = $CaCO_3$ % in DSDP 594 (Nelson et al., 1993), blue = $CaCO_3$ % in MD06-2987 (NIWA), Black = $\delta^{18}O$ variation in the CAICR (Pedro pers comm.), and the non shaded area shows MIS3. The age models for these cores have been compiled using different timescales which may account for some of the variation in the timing of productivity peaks however, this could also be due to regional variations in oceanography influencing the availability of SAW, STW and nutrients between the different sites

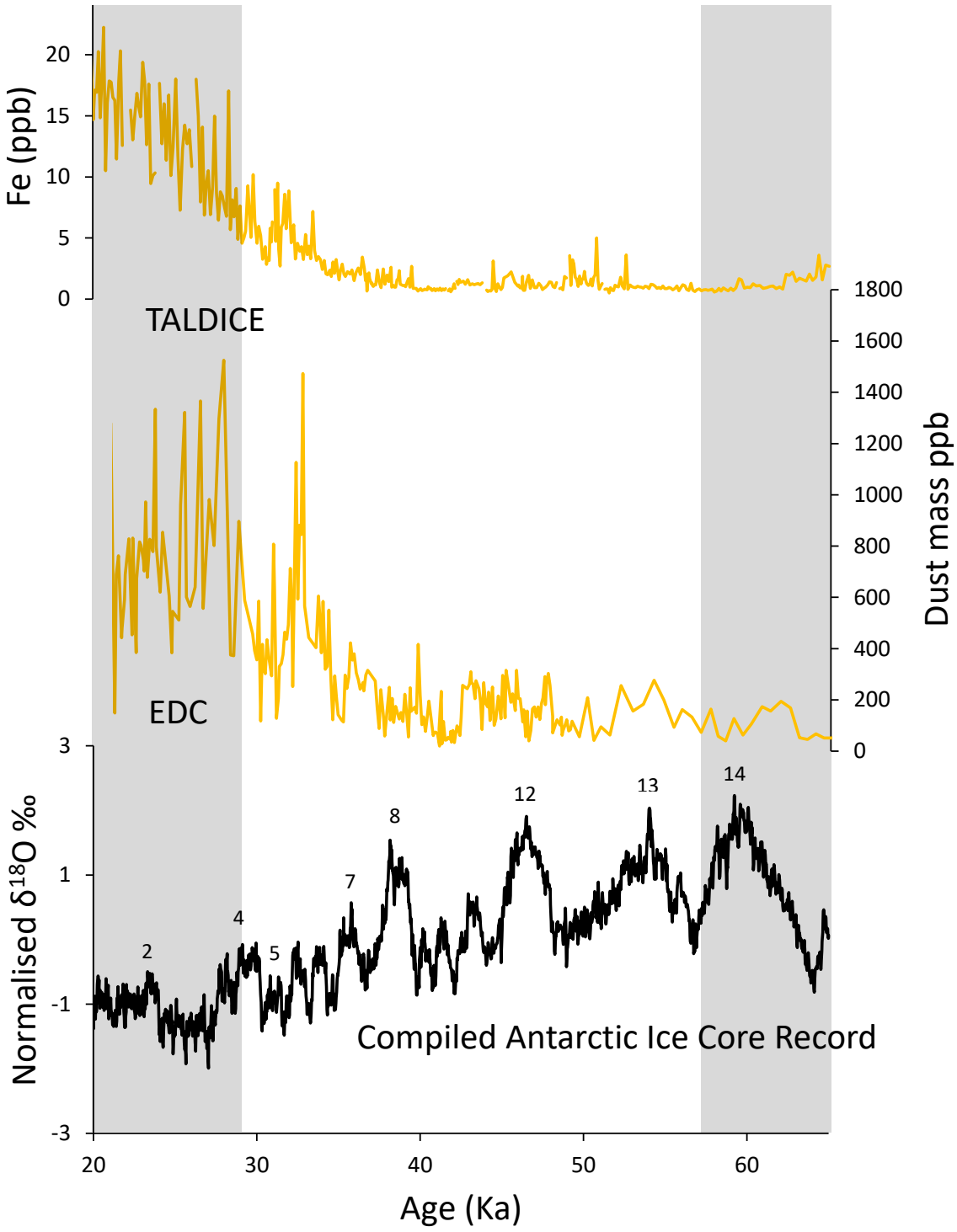

Figure 6.1.5: Antarctic MIS3 dust record and AIM events. The TALDICE (Vallelonga et al., 2013) and EDC normalised $\delta^{18}O$ (EPICA community members, 2006) ice core dust records, in yellow, show no correlation with the CAICR (Pedro pers comm.) in black. EDC core chronology was tuned to the AICC2012 timescale which is the timescale of both the TALDICE and CAICR ice core records. The non shaded area shows MIS3

AIM events are not driven by dust. The antiphased relationship between ITRAX Fe and Ca also suggests that incoming Fe to the site of TAN1106-28 was not in a bioavailable form, and therefore, productivity at this site cannot be driven by iron fertilisation, but must instead be controlled by temperature and/or light variability.

Increased upwelling brings nutrient and iron-rich deep water to the surface and can relieve light limitations (Graham et al., 2015), potentially resulting in the periods of enhanced productivity seen in TAN1106-28 during AIM events. This mixing is often a product of wind driven upwelling, and can result in reduced ocean stratification (Sigman et al., 2004). During AIM events, the westerly wind belt likely moved north (d'Orgeville et al., 2010; Lamy et al., 2004; Toggweiler et al., 2006), increasing wind driven upwelling in the mid-latitudes (Gottschalk et al., 2015). This may therefore be one of the mechanisms driving millennial scale productivity at the site of TAN1106-28 during MIS3.

Increased upwelling during MIS3 has also been used to explain the parallels between atmospheric CO_2 increases and AIM events in Antarctic ice cores as it has been attributed to increased ventilation of the Southern Ocean (Ahn and Brook, 2014; d'Orgeville et al., 2010; Gottschalk et al., 2015; Toggweiler et al., 2006). This gives additional evidence for periods of heightened upwelling during MIS3. However, productivity may have also been influenced by changes in sediment resuspension, due to variations in the position of the STF during MIS3 millennial scale events (Graham et al., 2015; Gottschalk et al., 2015), or temperature increases during Antarctic warm periods.

High-resolution analysis of *G. bulloides* $\delta^{18}O$ does not show any evidence for millennial scale events during MIS3 and has no correlation with $CaCO_3$ MAR in TAN1106-28 (Figure 6.1.6). As $\delta^{18}O$ fluctuates with temperature, this suggests that SSTs may not have varied during AIM events and therefore, that productivity at the site of TAN1106-28 is not driven by changes in temperature. However, $\delta^{18}O$ is also impacted by ice volume effects and salinity. As temperature reconstructions from marine sediment cores SO136-GC3 (Barrows et al., 2007) and DSDP 594 (Barrows et al., 2007; Kowalski and Meyers, 1997; Nelson et al., 1993), south of the STF in the SW Pacific (Figure 6.1.7), show SST increases that appear to coincide with periods of increased productivity (within the constraints of the age model), this suggests that SST variation during AIM events may play a role in driving productivity increases. However, although SST reconstructions show millennial scale events during MIS3, these are not at a high enough resolution to be definitively attributed to specific AIM events given the limitations imposed by the resolution of the different age models. Development of a high-resolution SST record in TAN1106-28, on the same timescale as the CAICR (AICC2012), will reveal if the *G. bulloides* $\delta^{18}O$ signal accurately reflects SST variations at this site, and will help with definitively matching SST increases in SAW to AIM events. The location of TAN1106-28 will also provide better coverage for New Zealand SST variation during MIS3 by contributing a southern counterpart to the eastern (DSDP 594) and western (SO136-GC3) SST reconstructions (Figure 6.1.7).

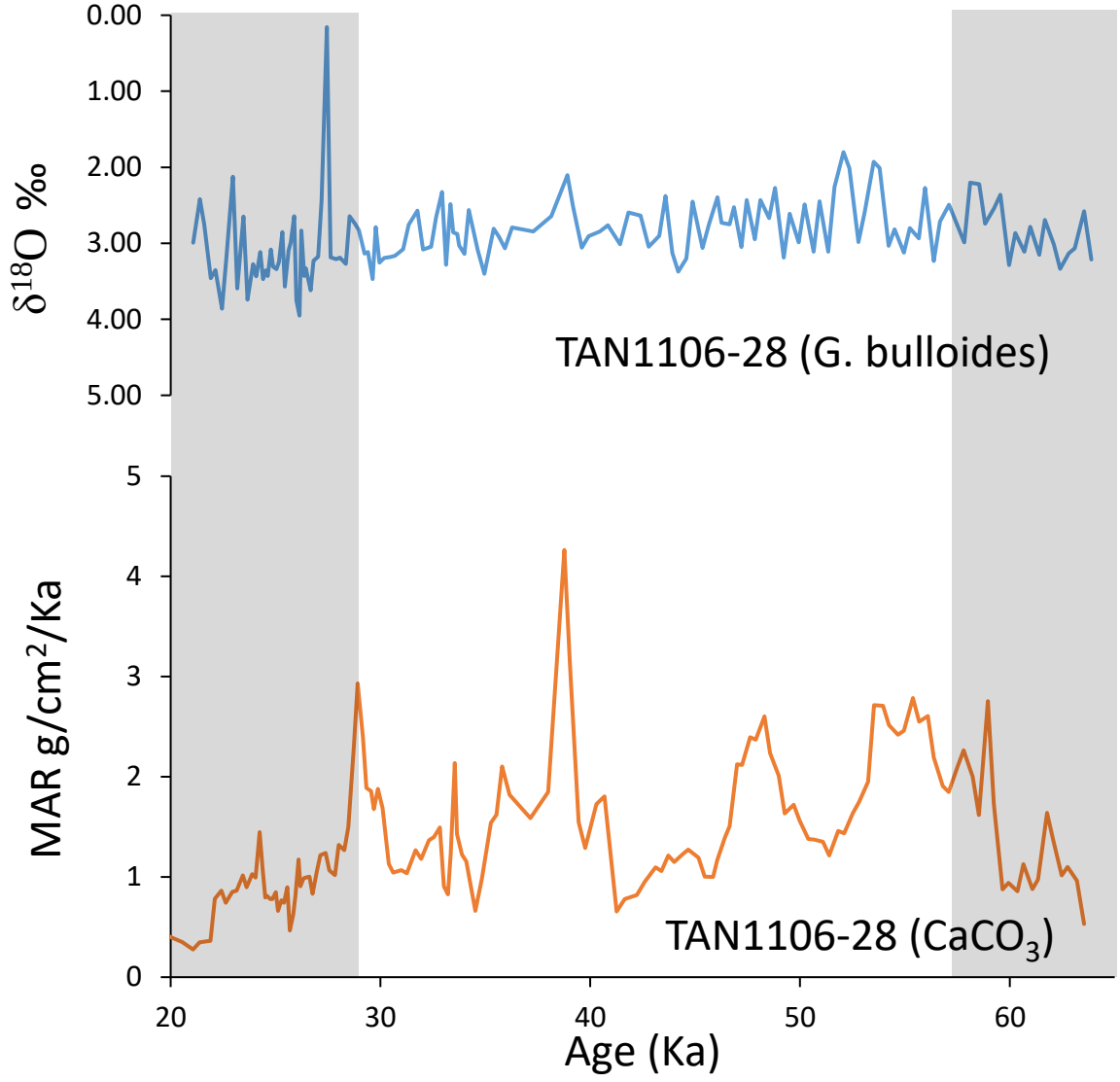

Figure 6.1.6: *G. bulloides* δ^{18}O and $CaCO_3$ MAR in TAN1106-28. The non-shaded area shows MIS3

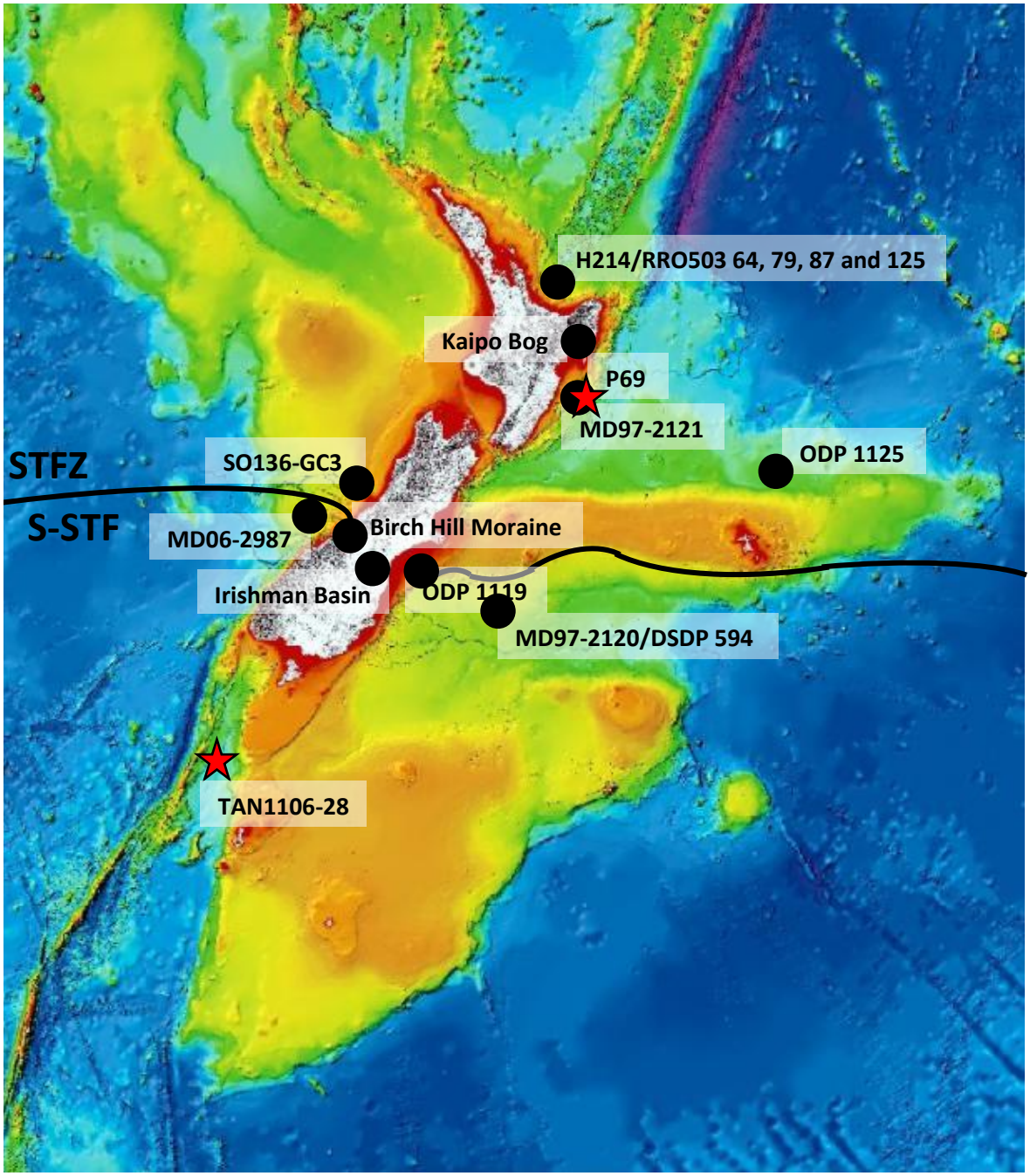

Figure 6.1.7: Location of sites used to discuss MIS3 climate variability. The bathymetric picture was revised from Mitchell et al. (2012) using the likely position of the STF-STFZ boundary, during MIS3 inferred from Bostock et al. (2015) (Section 3.1.1) and shown as a black line. The red stars show the cores analysed in this study and the black dots mark the location of cores whose climate reconstructions of MIS3 are compared to within this study. TAN1106-28 = this study and Bostock et al. (2015), Irishman Basin = (Doughty et al., 2013; Kaplan et al., 2010), ODP 1119 = Carter and Gammon (2004), MD97-2120 = Pahnke and Sachs (2006), DSDP 594 = Barrows et al. (2007); Kowalski and Meyers (1997); Nelson et al. (1993), SO136-GC3 = Barrows et al. (2007), Birch Hill Moraine = (Putnam et al., 2010), ODP 1125 = Schaefer et al. (2005), P69 = Nelson et al. (2000) MD97-2121 = this study and Carter et al. (2000); Carter and Manighetti (2006); Carter et al. (2008) H214 = Samson et al. (2005) and RR0503 64, 79, 87 and 125 = (Schiraldi et al., 2014)

6.2 Sediment core MD97-2121

6.2.1 Age Model

To constrain MIS3, chronology for MD97-2121 was analysed from the Kawakawa tephra at 982 cm (25.4 ±0.16 ka (Vandergoes et al., 2013)), to the bottom of the isotope drop at the start of the MIS4 at 1850 cm (61.62 ±0.83 ka (Epica Community Members, 2010)). Identification of the Kawakawa tephra was provided by (Carter et al., 2002). This was visually confirmed through the identification of increased concentration of glass shards under the binocular microscope and a peak in ITRAX Zr (Figure 6.2.3). The initiation of the isotope drop at the MIS4/3 boundary is apparent in the low resolution *G. bulloides* δ^{18}O (Carter and Manighetti, 2006) at 1800 cm (Figure 5.3.2b) and corroborated through higher resolution $CaCO_3$ analysis, which confirmed a decrease in $CaCO_3$% suggesting a descent into the cooler climate conditions of MIS4 (Figure 5.2.3b).

Between these end points, the age model for MIS3 was constructed using radiocarbon and tephra dates. However, the oldest tephra erupted during MIS3 is the Rotoehu tephra at 45.1 ±4 ka (Danisik et al., 2012) (modelled at 42.46 ±0.31 ka by OxCal in this study), and the oldest radiocarbon date is modelled at 46.19 ±0.45 ka (1490-1491cm), as this is near the limit of radiocarbon dating. This leaves the section of MD97-2121 between 61.65 ±1 ka and 46.19 ±0.41 ka unconstrained by age tie points. As there is a lack of obvious δ^{18} peaks within MD97-2121, this proportion of the core cannot be correlated to LR04 (Lisiecki and Raymo, 2005) or the CAICR (Pedro pers comm.) resulting in greater age uncertainty for this older section of core.

6.2.2 Linear sedimentation rates

Linear sedimentation rates average 35.21 cm/kyr and show an anomalous drop to ≈ 6.67 cm/kyr between 41.8 to 37.5 ka (Figure 6.2.1) which encompasses the ≈ 41.10 ±0.35 ka B.P. Laschamp excursion (Lascu et al., 2016). The Laschamp excursion is a ≈ 2.5 ka long magnetic reversal event which causes variations in atmospheric ^{14}C making accurate radiocarbon dating during this period difficult. Thus, the anomalous linear sedimentation rates between 41.8 to 37.5 ka are likely influenced by Laschamp excursion and therefore are unlikely to reflect changing sedimentation patterns.

Immediately following the Laschamp excursion there is a rapid increase in sediment accumulation, with linear sedimentation rates reaching 134.01 cm/kyr at 35.83 ka (Figure 6.2.1). This sudden jump in sedimentation rate could be the result of a turbidite, though both radiograph images and grainsize analysis suggest this is unlikely, or variations in paleomagnetic intensity. ^{10}Be and ^{9}Be isotopic concentrations in the western Equatorial Pacific show a reduction in geomagnetic relative paleointensity at 32 and 37 ka (Leduc et al., 2006) and this may have resulted in imprecise radiocarbon calibration during this time in a similar fashion to the Laschamp excursion.

Therefore, as these events may be a product of disturbances in radiocarbon ages, or a rapid accumulation event, dates which produced anomalous signals were removed from the age model (Figure 6.2.1). This will allow the identification of millennial scale events within core MD97-2121.

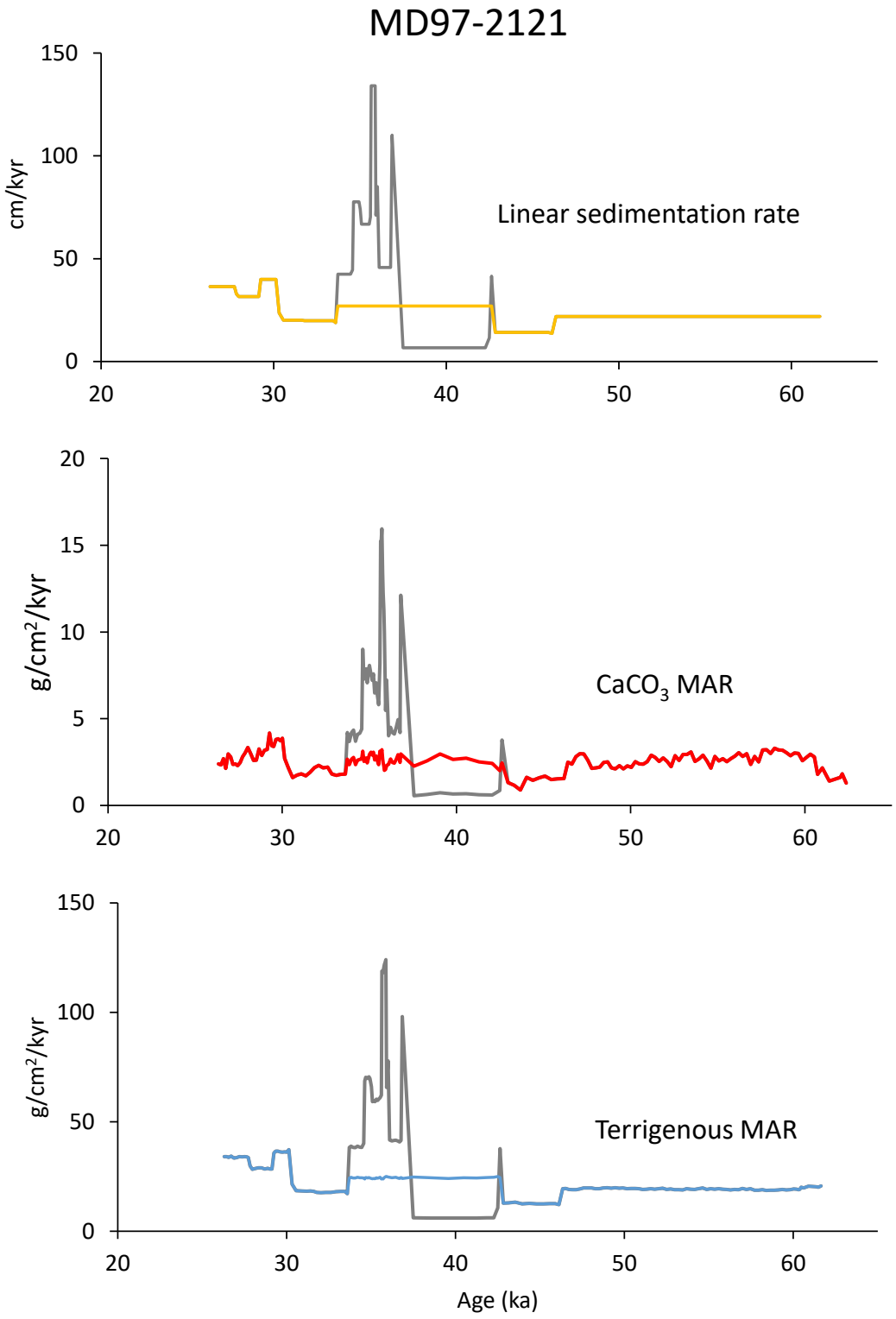

Figure 6.2.1: Sedimentation events in MD97-2121. The grey profile shows the original sedimentation rates and the coloured profile shows sedimentation rates when radiocarbon dates potentially altered by magnetic reversal events are removed (Section 6.2.2)

6.2.3 Millennial scale events

As high-resolution stable isotopes are not available for this core, peaks in $CaCO_3$ MAR were used for the identification of AIM events. It is difficult to extract AIM events from the marine sediment record in MD97-2121 as $CaCO_3$ MAR fluctuations do not correspond to the shape or magnitude of $\delta^{18}O$ in the CAICR (Pedro pers comm) (Figure 6.2.2). This suggests that $CaCO_3$ at the site of MD97-2121 is not solely impacted by the Antarctic climate, and, due to the close proximity of MD97-2121 to the tropics, that the Antarctic signal is likely buffered by a subtropical component.

Peaks in MD97-2121 $CaCO_3$ MARs were compared with $\delta^{18}O$ in the speleothem record from the Hulu Cave in China (Wang et al., 2001) in an attempt to extract the tropical signal (Figure 6.2.2). There is a modest correlation between $CaCO_3$ MAR peaks in MD97-2121 and $\delta^{18}O$ ‰ variations in the Hulu Cave speleothem record during MIS3, which is thought to show a strong correlation with the timing of Northern Hemisphere D-O, and North Atlantic Heinrich events (Wang et al., 2001). However, such correlations are tentative given the uncertainties with the MD97-2121 age model for MIS3.

Millennial scale climate variations synchronous to those observed in Antarctica have been recorded in the New Zealand terrigenous record (Carter and Gammon, 2004; Hajdas et al., 2006; Kaplan et al., 2010) suggesting this climate system may respond to AIM events during MIS3. The Kaipo Bog is a North Island terrestrial record proximal to MD97-2121 and contains pollen evidence for the Antarctic Cold Reversal (ACR) (Hajdas et al., 2006). The ACR is a millennial scale event (running from 13-14.7 ka) (Pedro et al., 2015), and evidence of this event in the North Island of New Zealand suggests that this region responds to Antarctic millennial scale events. Therefore, AIM events during MIS3 could be recorded at the site of MD97-2121 and might be identified in, yet unavailable, high resolution stable isotope data.

6.2.4 Cryptotephra

The use of ITRAX to identify depths containing cryptotephra was moderately successful, locating the depth at which the Kawakawa, Tahuna and Rotoehu tephra were deposited. Identification of these tephra was enabled through the analysis of multiple elements which varied between tephra, suggesting a multi element approach needs to be taken when using ITRAX XRF to identify rhyolitic cryptotephra (Figure 6.2.3). As ITRAX tephra proxies do not respond uniformly to cryptotephra deposition, the Omataroa, Mangaone, Maketu and Hauparu tephras, which were not found in MD97-2121, may have gone unidentified by ITRAX analysis. However, due to localised variations in wind and ocean current systems, it is also possible that these tephra were not deposited at the site of MD97-2121. Tephra also may have gone unidentified in the microscope analysis as it is hard to identify small increases in tephra over and above background levels in this core. Quantitative analysis of all depths where the ITRAX XRF identified possible cryptotephra deposits, and major element analysis of any glass shards found at those depths, would help with either locating these tephra, or definitively stating that they do not occur within MD97-2121. This analysis would also be helpful in understanding the potential of ITRAX for identifying rhyolitic cryptotephra (Rothwell and Croudace, 2015).

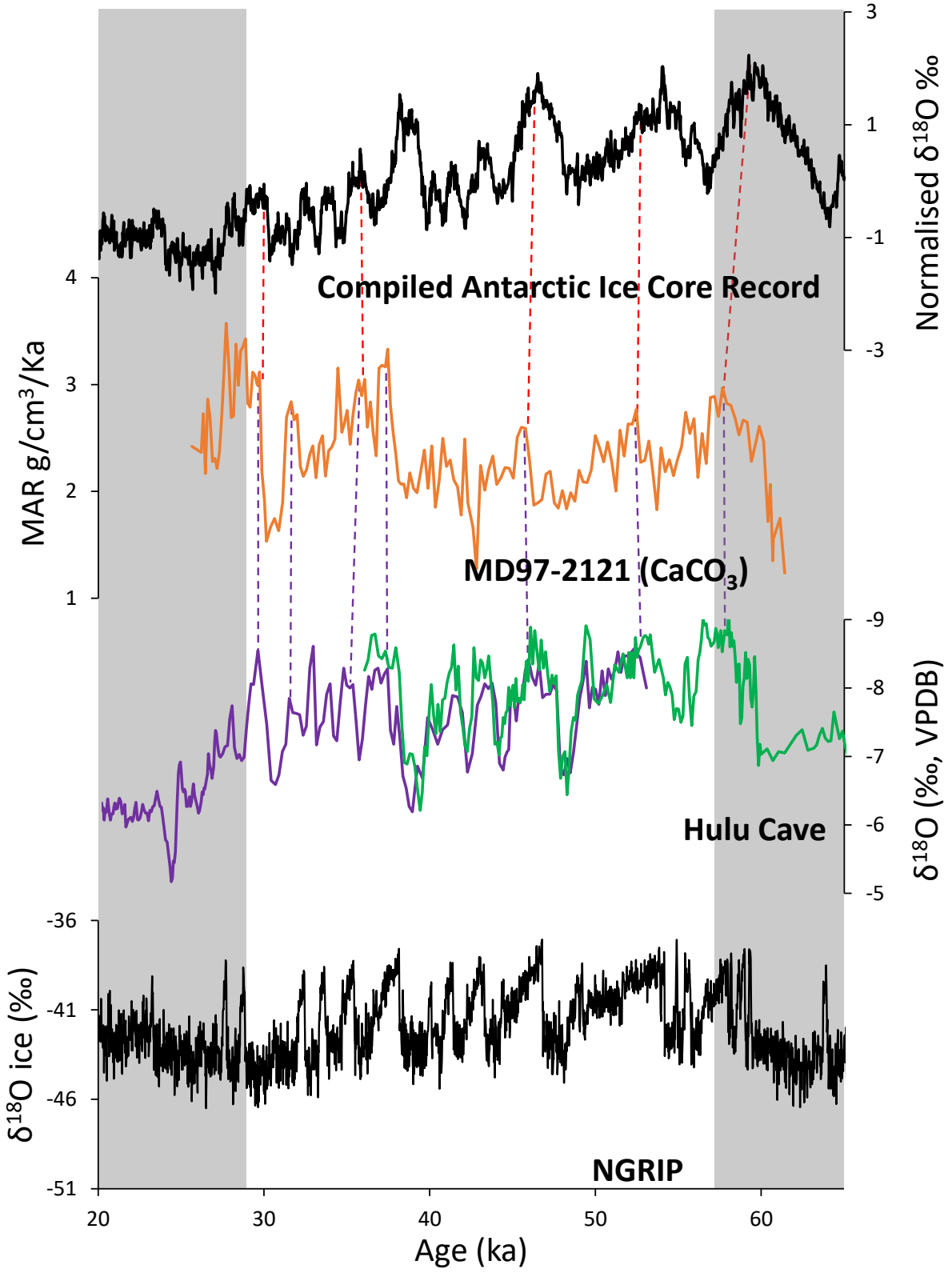

Figure 6.2.2: MD97-2121 $CaCO_3$ MAR compared with tropical and polar signals. The black profiles show $\delta^{18}O$ variations in the CAICR (Pedro pers comm.) in the upper graph, and $\delta^{18}O$ variations from NGRIP (NorthGRIP Community Members, 2004) in the lower graph. The red profile shows MD97-2121 $CaCO_3$ MAR and the purple and green profiles show $\delta^{18}O$ from stalagmites in the Hulu Cave, China (Wang et al., 2001). Red dashed lines show *possible* correlations between $\delta^{18}O$ AIM event in the CAICR and peaks in $CaCO_3$ MAR, purple dashed lines show *possible* correlations between the $\delta^{18}O$ Hulu cave speleothem record and $CaCO_3$ MAR and the non shaded area shows MIS3

To better constrain the radiocarbon marine reservoir age during MIS3, and reduce uncertainty associated with the age of tephra in MD97-2121, radiocarbon dates were selected either side of both the Tahuna and Rotoehu tephra.

Tephra	Calibrated ages	modelled ages
Above Rotoehu	42.78-41.44 ka	43.05-42.03 ka
Rotoehu	-	43.05-42.89 ka
Below Rotoehu	43.82-42.32 ka	43.09-41.63 ka
Above Tahuna	42.33-40.77 ka	39.45-35.33 ka
Tahuna	-	39.53-35.33 ka
Below Tahuna	36.13-34.48 ka	39.35-35.32 ka

Table 6.1: Calibrated and modelled ages for the Tahuna and Rotoehu tephras

Although the tephra dates calibrated for the Tahuna and Rotoehu tephra lie within the uncertainty constraints provided by Danisik et al. (2012) and Holt et al. (2014) (modified from Froggatt and Lowe 1990) respectively (Table 6.1), they both appear significantly later in the OxCal age model (Figure 6.2.3). The length of this delay is not uniform between the tephra, but it could reflect an underestimation of the marine reservoir age in the age model, as the outlier model gives greater weighting to dates which correlate with each other and there are significantly more radiocarbon dates than calibrated tephra dates. However, these variations could also reflect a later deposition of both tephra to the site of MD97-2121 due to errors in the age model, or a younger eruptive age for the tephra than the literature suggests. As the Tahuna tephra lies within the Laschamp excursion, ^{14}C may also be unreliable for radiocarbon dating in these samples. This could account for the anomalously low calibrated age immediately below the Tahuna tephra (Table 6.1) which may have also lowered the modelled age for the Tahuna tephra.

The Hauparu, Maketu, Mangaone, and Omataroa tephra were all erupted during MIS3 and are not identified in MD97-2121. Within the uncertainty bounds of the Hauparu tephra, the only significant variation is a spike in Zr at 40.2 ka (Figure 6.2.3). This sample has been analysed under a binocular microscope and shows no significant deviations in glass shard fragments from background levels suggesting the Hauparu Tephra may not have been deposited or preserved at the site of MD97-2121.

The Maketu tephra is in close proximity to the OxCal calibrated age of the Tahuna tephra (Figure 6.2.3). However, the distinct separation between the major element composition of the Maketu tephra and the Tahuna tephra (Figure 5.5.3) means glass shards deposited at 38.3 ± 0.8 ka cannot originate from the Maketu tephra. There is also an event at 30.8 ka, which lies within the age uncertinites of the Maketu tephra (Jurado-Chichay and Walker, 2000), and shows variation in several ITRAX tephra elements (Figure 6.2.3). This cryptotephra signal guided selection of a sample (tephra 2) for geochemical analysis in spite of a lack of visible evidence for glass shards above background levels. However, major element analysis did not reveal a distinct tephra at this site. Glass shards within this sample showed similar major element characteristics to the Tahuna, Rotoehu and Kawakawa tephra (Figure 5.5.2).

ITRAX tephra proxies show a possible cryptotephra signal within the tightly constrained bounds of the Mangaone age range (Jurado-Chichay and Walker, 2000). Sediment deposited in this age

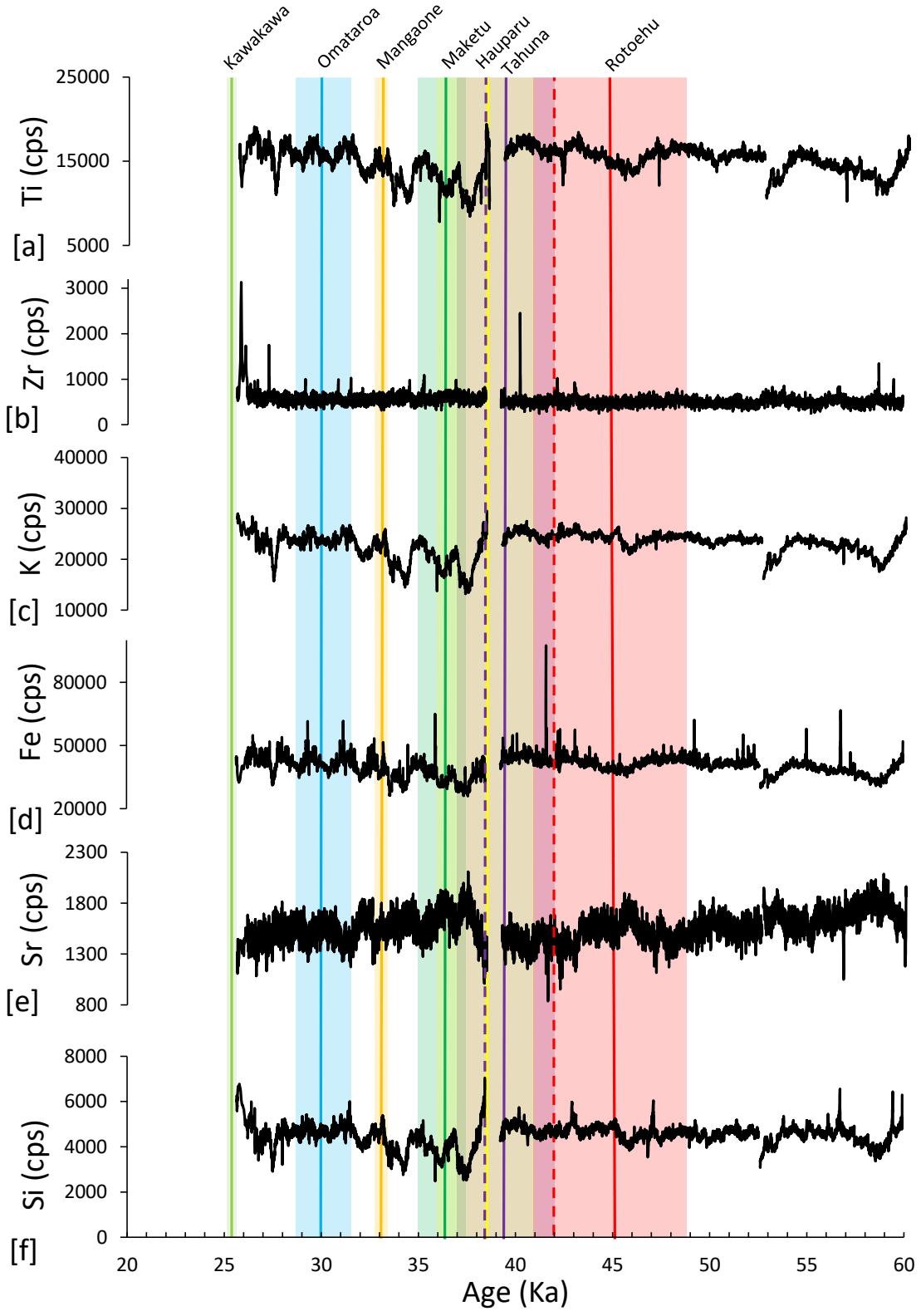

Figure 6.2.3: ITRAX tephra proxies and MIS3 tephra. The coloured lines show the age of the tephra, the shaded area marks $\sigma 1$ and the dashed line marks where the MD97-2121 age model locates the tephra. Red = the Rotoehu at 45.1±4 ka (Danisik et al., 2012), Purple = the Tahuna at 39.3±2.4 Ka, Yellow = the Hauparu at 38.5±2.5 ka (Froggatt and Lowe 1990 modified by Holt et al. 2014), Light Green = the Maketu at 36.3±1.2 ka (Jurado-Chichay and Walker, 2000), Orange = the Mangaone at 33±0.3 ka (Jurado-Chichay and Walker, 2000), Blue = the Omataroa at 30.4±1.5 ka (Froggatt and Lowe 1990 modified by Holt et al. 2014) and Dark Green = the Kawakawa at 25.4±0.16 ka (Vandergoes et al., 2013)

range has not been examined under the microscope so it is conceivable that a cryptotephra layer from the large eruptive volume (19.9km^3 (Holt et al., 2014)) of the Mangaone tephra made it to the site of MD97-2121. However, it is likely that the Mangaone tephra would appear in tephra 2 as part of the background signal. As this does not occur (Figure 5.5.2), the Mangaone tephra may not have been deposited at the site of MD97-2121.

The Omataroa tephra is either not present in the sediment of MD97-2121, or is not recorded in the ITRAX data as there is no significant variation between any of the ITRAX tephra proxies (Ti, Zr, K, Fe, Sr and Si) during the Omataroa age bracket (Froggatt and Lowe 1990 modified by Holt et al. 2014).

Analysis of cryptotephra deposits within MD97-2121 shows there is no way to identify rhyolitic cryptotephra solely through the use of ITRAX. The Rotoehu, Tahuna and Kawakawa tephra all show deviations in different ITRAX elements and, as reflected in the misidentification of the Maketu tephra, there are other ocean/climate processes which can impact ITRAX data in a similar manner to cryptotephra deposits. However, when used in conjunction with other methods, such as visual identification through a binocular microscope and geochemical analysis using an EMP, ITRAX can help identify samples which may contain cryptotephra deposits.

Electron microprobe analysis was used to distinguish the tephra found in MIS3 on the basis of their major element composition. This was moderately successful as 3 distinct tephra compositions were identified (Figure 5.5.2). However, there are slight variations between the major element composition of the analysed glass shards and the published major element compositions of the Rotoehu, Tahuna and Kawakawa tephra, and the Kawakawa and Omataroa tephra cannot be distinguished by major element analysis alone (Allan et al., 2008). A greater glass shard sample size for EMP analysis could help better constrain the major element compositions. Trace element analysis could also be used to fingerprint the cryptotephra layers and give greater certainty in the identification of the origin of these deposits (Allan et al., 2008).

6.2.5 Terrigenous accumulation

During MIS3 linear sedimentation rates in MD97-2121 are high due to the close proximity of this site to the high discharge rivers of the eastern North Island (Carter et al., 2002; Carter and Manighetti, 2006). Fluvial discharge is the primary source of sediment to the continental shelf, and as a consequence, sediment deposited at MD97-2121 is predominately terrigenous in composition. The eastern North Island also receives a portion of volcanic sediment due to its close proximity to the TVZ, as evident from the high background levels of tephra throughout the core (Section 6.2.4), although this does not drastically impact sedimentation rates.

Investigation into the variation of terrigenous sediment supply to the site of MD97-2121, has shown that glacial-eustatic sea level fluctuations exert a strong control over the amount of sediment discharged to the shelf edge (Carter and Manighetti, 2006). During the LGM, sea levels were 120 m lower then the present. This enabled river systems to transport sediment over the exposed continental shelf and deposit it directly into the deep ocean (Carter et al., 2000; Carter and Manighetti, 2006; Griggs et al., 1983; Kowalski and Meyers, 1997), resulting in the highest terrigenous MAR rates recorded in MD97-2121 (Carter and Manighetti, 2006). When sea levels were higher, such as during MIS3 (60-80 m below present), some sediment remained trapped on

the continental shelf, by along shore currents such as an ancestral Wairarapa coastal current, and at the palaeoshoreline, by longshore drift currents, assuming that a dominantly southerly wind regime operated in MIS3 as it does today (Carter et al., 2008).

Terrigenous sediment is also transported to the site of MD97-2121 by the coastal currents including the WCC from the south, and ECC from the north. Under the cool climate conditions of MIS3, it is likely that the transport of the ECC was limited due to a reduction in the Tasman Front inflow as highlighted in foraminiferal assemblages for MIS2 (Carter et al., 2008). However, the ECC may still have carried sediment to MD97-2121 sourced from the Waiapu and Waipaoa rivers.

During MIS3, terrigenous MARs increase exponentially heading into the MIS2 glaciation (Figure 6.2.4). This likely reflects a gradual lowering of eustatic sea levels as the climate system transitions towards the MIS2 glacial. In MIS4, sea levels were 50 m below the present, and 70 m higher than they were during the LGM, and this has been proposed as the mechanism limiting terrigenous MAR during MIS4 (Carter and Manighetti, 2006). The gradual increase in terrigenous MAR during the late MIS3 therefore, likely reflects a lowering of sea level from 80 m below present to 120 m below present.

Terrigenous MARs during MIS3 are high (>15g/cm^2/ka), and dominate $CaCO_3$ MARs which are nonetheless significant as shown in Figure 6.2.4, and by Carter et al. (2000). Short term variations in terrigenous sediment supply do not coincide with AIM events and are therefore unlikely to be the result of millennial scale forcing from the south (Figure 6.2.4). Instead they may have resulted from short term fluctuations in sea level (Siddall et al., 2008), or variations in the ECC either by subtropical forcing and/or changes in the gateways for the Tasman Front which would have resided north of its modern position (Carter and Manighetti, 2006; Carter et al., 2008).

6.2.6 Biological productivity

High-resolution biogenic silica was not analysed in MD97-2121. As the concentration of biogenic silica averages only 2.9% (0.3-1.5 g/cm^2/kyr) during MIS3 in MD97-2121 (Carter and Manighetti, 2006), it was assumed that $CaCO_3$ MARs better reflect variations in biological productivity. Dissolution was not directly measured in this core, however, as MD97-2121 sits at a water depth of 2314 m, it is well above both the foraminiferal lysocline, $\approx$ 3600 m water depth, and Calcium Compensation Depth (CCD), $\approx$ 4400 m depth (Bostock et al., 2011; Crundwell et al., 2008; Hayward et al., 2007). As the neighbouring P69 core (Figure 6.1.7) shows no evidence for cold period carbonate dissolution (Nelson et al., 2000), it was assumed that there was also minimal dissolution at MD97-2121 (Carter and Manighetti, 2006).

Foraminifera assemblages and SST reconstructions show an influx of cooler SAW to the site of MD97-2121 (Carter et al., 2008) and the neighbouring P69 (Nelson et al., 2000) during MIS2. This SAW was forced northward through the Mernoo Saddle by a strengthened SC (Carter et al., 2002; Nelson et al., 2000; Schaefer et al., 2005), with possible contributions from the east around the Chatham Rise (Carter et al., 2008; Schiraldi et al., 2014). A strengthened SC and SAF is proposed to be the response of an enhanced westerly wind system, lowered sea levels and more compressed SAW mass during the glacial (Carter et al., 2002; Nelson et al., 2000; Schiraldi et al., 2014). As MIS3 was characterised by similar, but less severe ocean/climate conditions to MIS2,

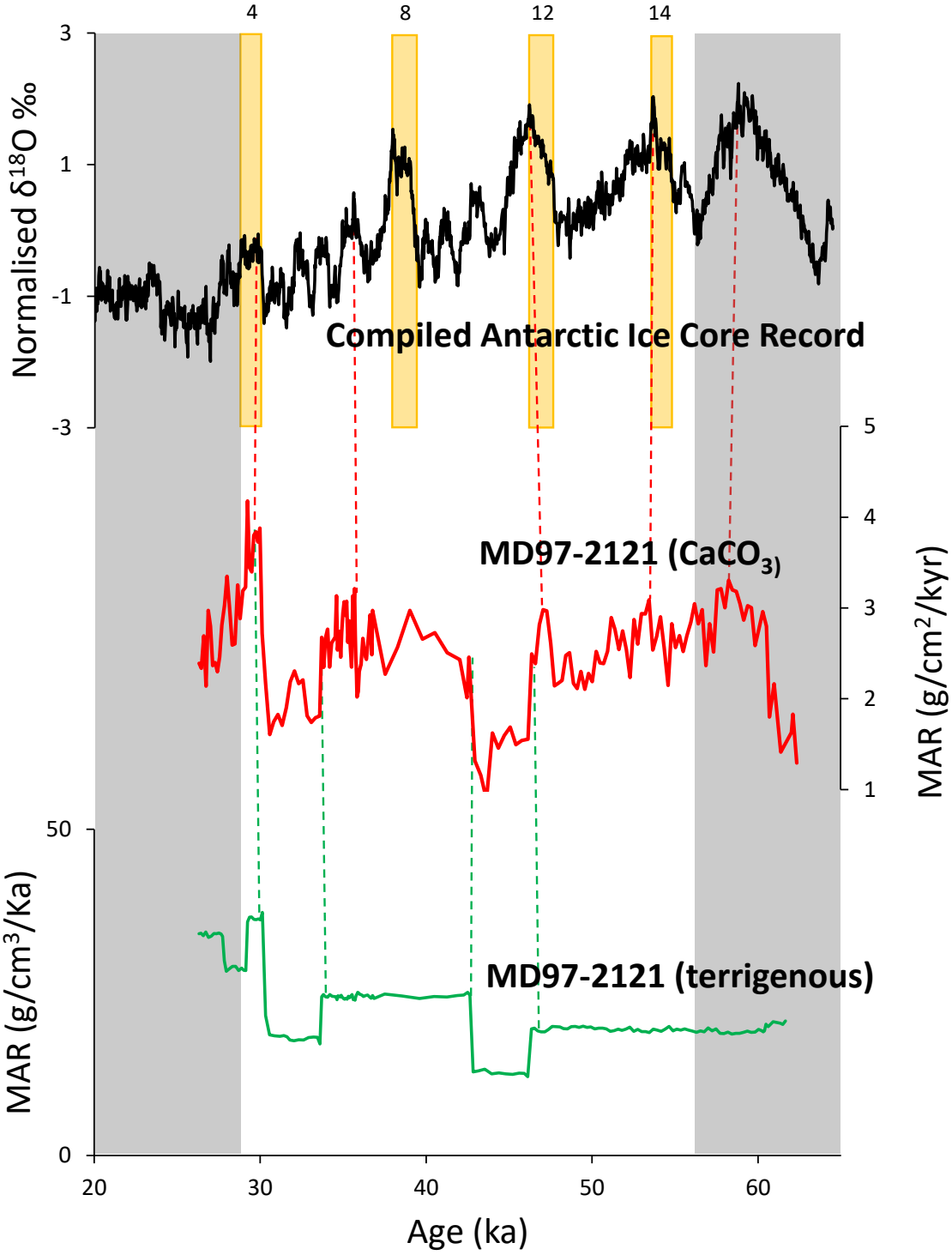

Figure 6.2.4: Terrigenous and $CaCO_3$ MAR in MD97-2121 and $\delta^{18}O$ AIM events in the CAICR (Pedro pers comm.) during MIS3. The black profile shows $\delta^{18}O$ variations in the CAICR (Pedro pers comm.), the red profile shows $CaCO_3$ variation in MD97-2121, and the green profile shows terrigenous MAR in MD97-2121. The yellow shaded bars mark AIM events found in TAN1106-28 which are labelled at the top of each bar. The yellow dashed line indicates possible tie points between $CaCO_3$ MAR in MD97-2121 and AIM events in the CAICR (Pedro pers comm.), the green dashed line shows variations in terrigenous MARs and the non shaded area shows MIS3

it is reasonable to assume that SAW may have also been present at the site of MD97-2121 during MIS3. After all, SAW reaches the site in modern times especially under strong meteorological forcing from the south. It is also likely that SAW may have transferred the AIM signal to the site of MD97-2121. This may have resulted in the MIS3 SST fluctuations at this site from Pahnke and Sachs (2006).

There may be some correlation between MD97-2121 $CaCO_3$ MAR, Pahnke and Sachs (2006) SST reconstructions, low resolution smoothed SST reconstructions from core site SO136-GC3 (Barrows et al., 2007) (Figure 6.1.7), and MIS3 AIM events. This suggests that during MIS3 a modulated Antarctic signal may be experienced in surface waters to the north of the STF. However, due to the low resolution of core SO136-GC3 (Barrows et al., 2007), it is difficult to extract short term climate variations and therefore inferences must be made using reconstructions of how this climate system responded to the the millennial scale ACR.

The ACR can be seen in the benthic $\delta^{18}O$ record from MD97-2121. However, it does not appear in alkenone SST reconstructions (Pahnke and Sachs, 2006), or planktonic $\delta^{18}O$ (Carter and Manighetti, 2006) until the peak of the ACR, when Antarctic temperatures are at their coldest. This suggests subtropical modification of the surface waters occurred at the site of MD97-2121 during this time (Carter et al., 2008)

Marine sediment cores in the Bay of Plenty (BOP) region have been suggested to record the ACR in foraminfera based SST reconstructions (Samson et al., 2005). This response to the ACR is attributed to incoming subsurface SAW, which flows around the Chatham Rise, as well as through Mernoo Saddle and then northeast to the Bay of Plenty region (Samson et al., 2005; Schiraldi et al., 2014). The duality of the expression of the ACR in surface waters between the BOP and MD97-2121 is likely to be the result of variable subsurface SAW. However, as MIS3 is cooler than the deglacial climate setting which contains the ACR, there is likely a greater component of SAW at the site of MD97-2121 and this may have resulted in a greater recording of MIS3 Antarctic millennial scale events in the productivity signal of MD97-2121, although this signal is still buffered by a subtropical component (Figure 6.2.4).

During warm events, planktonic foraminifera assemblages and SST reconstructions show that subtropical inflow as represented by STW, increased to the site of MD97-2121 via a strengthened ECC which may have also brought increased terrigenous material to this site during warm AIM events (Carter and Manighetti, 2006). The mixing of STW with SAW likely increased productivity and may be the cause of increased $CaCO_3$ MARs during AIM events. However, in the absence of water mass reconstructions for MIS3 based on foraminiferal assemblages, any change in the subtropical inflow to the site of MD97-2121 cannot be confirmed.

6.3 MIS3 at sites TAN1106-28 and MD97-2121 - ocean/climate reconstructions

Comparisons between the productivity and terrigenous signals in TAN1106-28 and MD97-2121, give an indication of how AIM events were expressed across the STF in the SW Pacific during MIS3. This reconstruction will help with the identification of how this signal is transferred via atmospheric and oceanic circulation patterns, and its likely effect on productivity and terrigenous variations.

6.3.1 Millennial events during MIS3 in the New Zealand region

During MIS3 proxy records in TAN1106-28 to the south of the STF are approximately synchronous to the climate variability observed in Antarctic records. In this core productivity and terrigenous sediment supply show an antiphased relationship, with productivity peaks developing during AIM interstadial in the CAICR (Pedro pers comm.), and terrigenous peaks occurring during Antarctic stadial events (Figure 6.1.3)(Carter and Manighetti, 2006). Increased productivity during AIM events is inferred to be a response to increased SST and/or light availability at the site of TAN1106-28, while terrigenous MAR variation was attributed to sea level fluctuations and variable onshore erosion rates due to glacial advance and retreat.

The New Zealand terrestrial record appears to show a similar millennial scale response to TAN1106-28 during MIS3 AIM events. This is inferred from Younger Dryas and Antarctic Cold Reversal reconstructions, which show that millennial scale glacial (Doughty et al., 2013; Kaplan et al., 2010; Carter and Gammon, 2004) and temperature fluctuations (Putnam et al., 2010) vary in phase with Antarctic climate records. For these variations to be expressed in terrestrial New Zealand, an atmospheric transfer of Antarctic surface temperatures to the New Zealand region may have been enabled via the northward movement of the STF during MIS3. However, modulation of this signal by a changing ocean cannot be discounted.

During MIS3 the STF off the west coast of New Zealand was likely located further north than its contemporary position, under similar mechanisms to those driving northward movement of this front during the LGM (Bostock et al., 2015). This places the South Island adjacent to cool SAW, which may result in a greater susceptibility to Antarctic influences. When the erosional vulnerability of the Southern Alps to climate variations (Carter and Gammon, 2004) is combined with temperature fluctuations (Putnam et al., 2010), and a shifting position of the westerly winds (Kohfeld et al., 2013), it is feasible that AIM events during MIS3 are recorded in the New Zealand glacial record. However, a lack of high-resolution MIS3 terrestrial records, means that it is difficult to extract the magnitude of this Antarctic signal and how it is expressed in onshore New Zealand. Development of these records may help establish the extent (if any), to which the Antarctic signal is buffered by climate signals from the tropics in onshore New Zealand.

Terrigenous MARs at MD97-2121 show no obvious correlation with Antarctic induced climate change events, and are distinct from the TAN1106-28 terrigenous signal (Figure 6.3.1). The Kaipo Bog shows evidence for the ACR in its pollen record (Hajdas et al., 2006), and as this site is in close proximity to MD97-2121, this suggests Antarctic millennial scale temperature fluctuations can be recorded in this region. There is no evidence for AIM events in terrigenous MARs at the

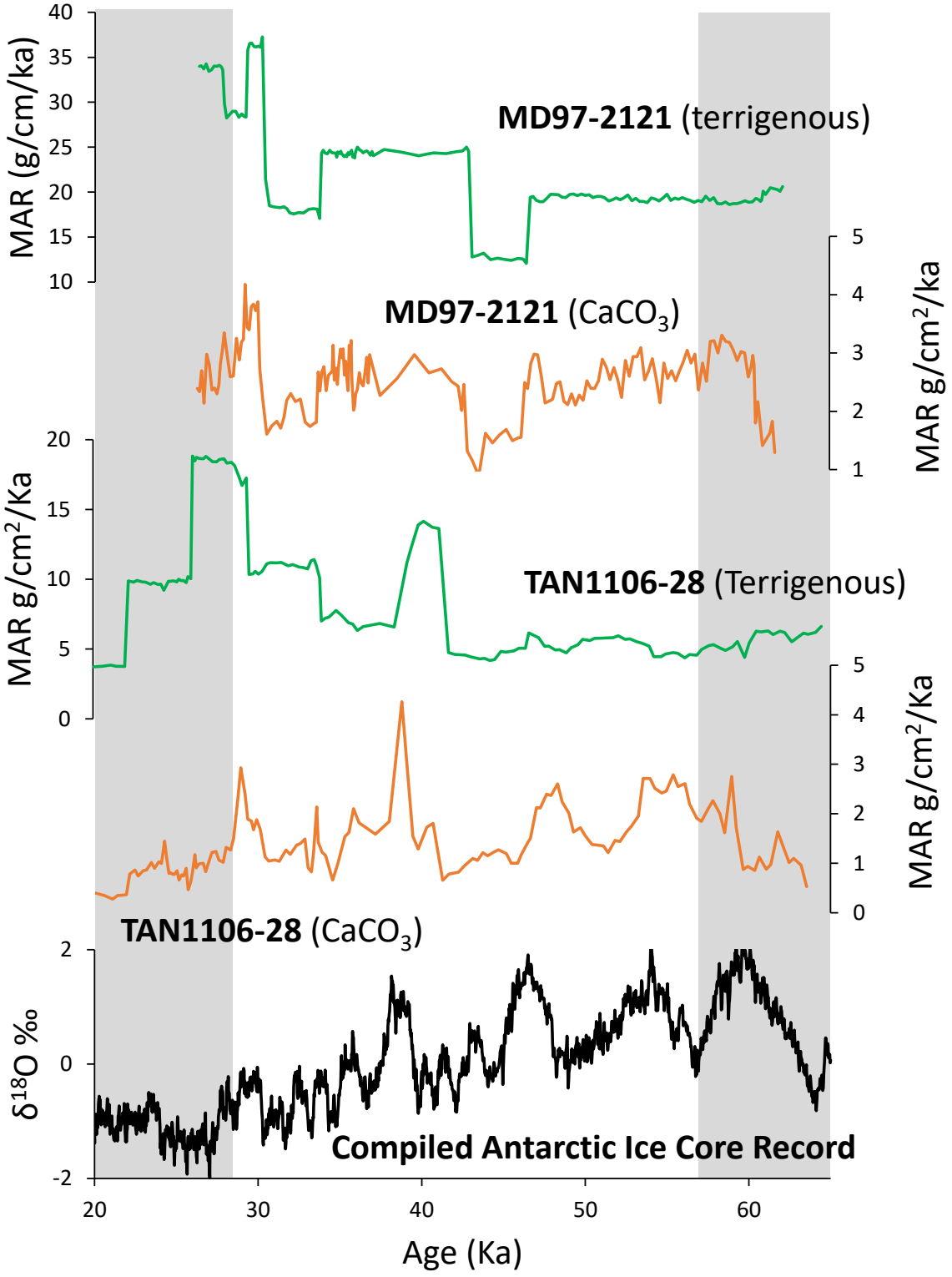

Figure 6.3.1: Productivity and terrigenous accumulation in TAN1106-28 and MD97-2121. Red = $CaCO_3$ variability, green = terrigenous variation, black = $\delta^{18}O$ variations in the CAICR (Pedro pers comm.) and the non shaded area shows MIS3

site of MD97-2121 and terrigenous accumulation must instead be a function of eustatic sea level change, and variations in the strength of the ECC. The ECC transports STW containing terrigenous sediment from the northern Waipaoa and Waiapu rivers to the site of MD97-2121.

MD97-2121 also shows a muted AIM signal in comparison to TAN1106-28 (Figure 6.3.1). As Antarctic millennial scale events are recorded in the productivity signal of TAN1106-28 and SST records in marine sediment cores south of the STF (Barrows et al., 2007; Kowalski and Meyers, 1997; Nelson et al., 1993; Pahnke and Sachs, 2006), but are distorted in surface water records from marine sediment cores to the north of the STF (Barrows et al., 2007; Nelson et al., 2000; Samson et al., 2005; Schaefer et al., 2005; Schiraldi et al., 2014), this suggests that the STF acts as a boundary to surface waters containing Antarctic millennial scale events during MIS3. A strengthening of the SC and the SAF during MIS3 likely forced some SAW, containing the AIM signal, north, through the Mernoo Saddle, and west, along the Chatham Rise, to MD97-2121 where mixing with STW produced the muted Antarctic signal found in this marine sediment core.

Unlike planktonic $\delta^{18}O$, the benthic signal at MD97-2121 shows a close correlation to the ACR. This suggests that an Antarctic climate signal was transferred to mid latitudes by deep water circulation circulation at this time. However, low resolution isotope analysis from *U. peregina*(Carter and Manighetti, 2006) does not show any evidence for millennial scale fluctuations during MIS3 suggesting AIM events (i) did not impact deep water circulation, (ii) somehow the signal was blocked prior to reaching the site of MD97-2121, or (iii) the sample resolution is too coarse.

6.3.2 The SW Pacific and global climate variations during MIS3

The data from core site TAN116-28 supports previous work from around the Southern Ocean which has found evidence of AIM events in the South Atlantic (Gottschalk et al., 2015; Barker et al., 2009), South Indian (Sicre et al., 2005), and SE Pacific (Caniupán et al., 2011) Oceans. This suggests that the Antarctic climate signal extends into the mid latitudes in the Southern Hemisphere and that the ocean circulation and atmospheric processes which transfer the AIM signal to the site of TAN1106-28, are likely to operate throughout the Southern Ocean. These records show distinct warming during Heinrich events, in phase with Antarctic climate records, and this has been associated with a southward movement of the STF in the South Atlantic during Heinrich events (Barker et al., 2009; Barker and Diz, 2014). Similar fluctuations in the position of oceanic front systems around New Zealand may have resulted in a reduction of SAW and increased ECC transport during Heinrich events at the site of MD97-2121. This could have resulted in the increase in both biological productivity and terrigenous accumulation seen during Heinrich event 3 and 5 (Figure 6.3.2). As there are no age tie points during Heinrich event 4 (due to radiocarbon uncertainty associated with the Laschamp excursion), this event is not recorded in terrigenous or $CaCO_3$ MAR.

The biological productivity signal in TAN1106-28 aligns with the timing of ventilation and upwelling events in the Southern Ocean and may have therefore been influenced by similar processes driving these mechanisms. During AIM events, increased ventilation of the Southern Ocean resulted in atmospheric CO_2 increases (by 20-30 ppmv) which occurred in phase with Antarctic temperature records (Fischer et al., 2010; Martinez-Garcia et al., 2009; Toggweiler et al., 2006). Enhanced ventilation during AIM events may have resulted from a reduction in sea ice extent, a weakening of ocean stratification, small changes in Southern Ocean productivity, and/or a strengthening of the westerly wind belt (d'Orgeville et al., 2010; Fischer et al., 2010; Martinez-Garcia et al.,

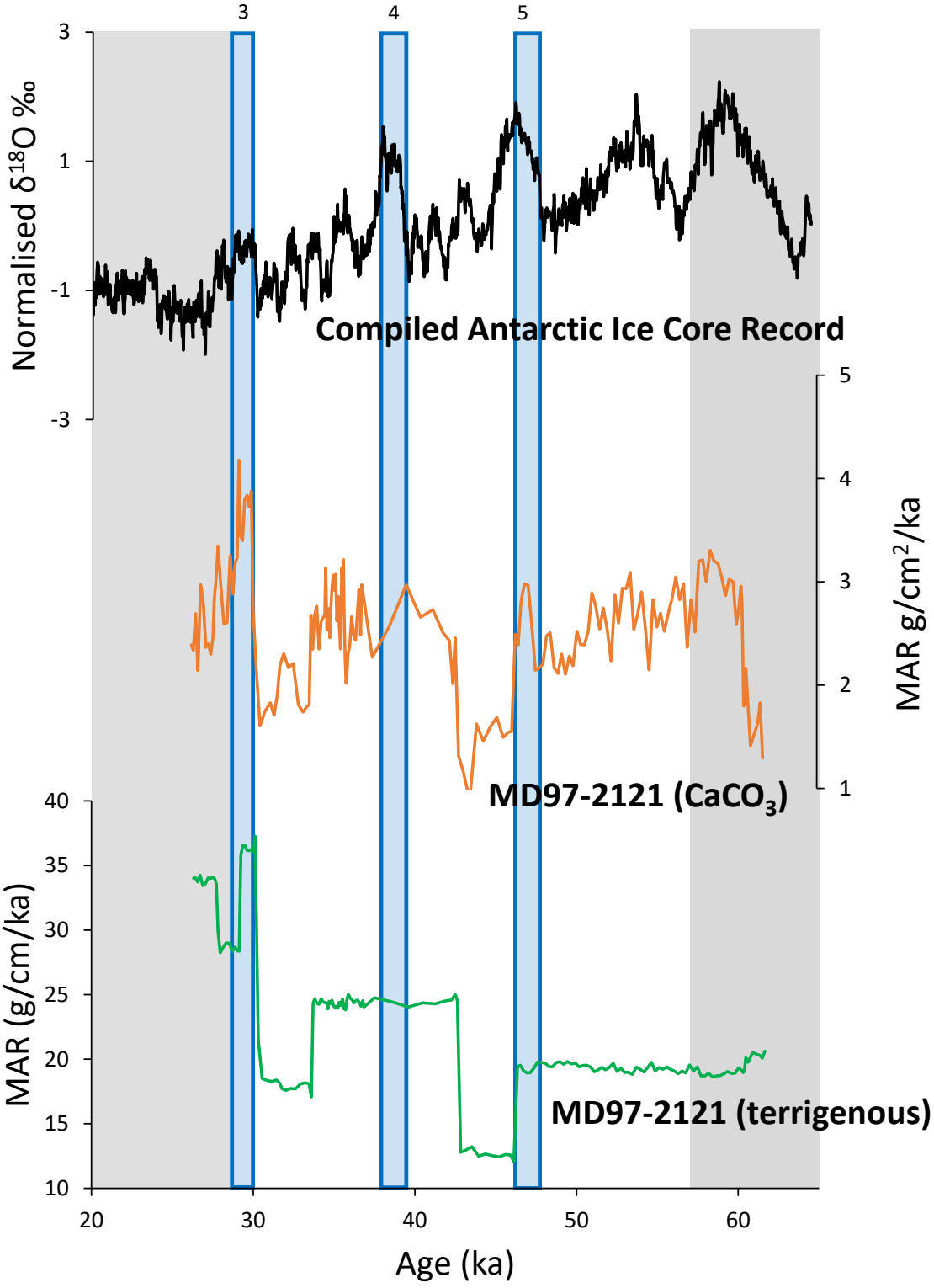

Figure 6.3.2: Heinrich events in MD97-2121. Heinrich events are shaded blue boxes and numbered as in Ahn and Brook (2014). Black = CAICR (Pedro pers comm), red = $CaCO_3$ MAR in MD97-2121, and green = terrigenous MAR in MD97-2121

2009; Gildor et al., 2002). Some of these processes may have been working concurrently to increase productivity in the southern mid-latitude ocean basins.

Reduced sea ice extent, weaker ocean stratification and enhanced westerly winds over the Southern Ocean, are likely a response to the southward migration of warmer waters due to a weakening of the AMOC in the North Atlantic (d'Orgeville et al., 2010; Lamy et al., 2004; Toggweiler et al., 2006; Ziegler et al., 2013). Breakdown of the AMOC results in warming over Antarctica and cooling over Greenland and is generally accepted within the literature as the driving mechanism behind the bi-polar response of the Antarctic and Greenland ice core records (Barker et al., 2009; Gottschalk et al., 2015). There is less consensus however, surrounding the mechanisms which drive this millennial scale AMOC variability. Intermediate complexity global climate models suggest enhanced bottom water transportation influences millennial scale variability, contributing to increased surface warming and ventilation in the Southern Ocean, and may help drive Southern Ocean meridional heat transport (Menviel et al., 2015; Shin et al., 2003). Enhanced bottom water formation is used to account for the magnitude of AIM events 12 and 18 which cannot be explained by AMOC variability alone (Menviel et al., 2015). A good understanding of these large scale ocean/climate processes will help further interpretations about how the global ocean/climate system responds to rapid climate events. When combined with reconstructions about how local climate systems respond to these large scale events, this may help with projections of how local climates vary during rapid climate change events.

7 Future research

- Productivity was the key variable used to analyse the extent (if any) to which the STF blocks Antarctic millennial scale events from propagating further north. To validate the interpretation of productivity variability in both TAN1106-28 and MD97-2121, the fragmentation index (Le and Shackleton, 1992) and/or organic carbon reconstruction (Crundwell et al., 2008) could be developed to confirm the interpretation of minimal dissolution in both cores. Organic carbon reconstruction could also be used to determine productivity (Cartapanis et al., 2016).

- Once the productivity signal is verified, high resolution SST and water mass reconstructions using foraminiferal assemblages should also be undertaken. This will help with (i) the interpretation of the mechanisms driving the millennial scale oscillations in productivity during MIS3 at the site of TAN1106-28, (ii) identification of source water variation to the site of MD97-2121, and (iii) contribute to productivity analysis.

- ^{10}Be could be used to examine geomagnetic reversals, such as the Laschamp excursion, which may occur in both cores during MIS3, although convergence in the outlier age model of TAN1106-28 suggests there was little error with these radiocarbon dates. This would assess the accuracy of radiocarbon dates and associated linear sedimentation rates around $\approx$ 40 ka.

- Continued analysis of MD97-2121 should also include increased investigation into the cryptotephra deposits. Although radiocarbon dates and major element compositions have allowed the identification of the Tahuna and Rotoehu tephra within MD97-2121, further analysis of glass shards may help better constrain major element weight %. This could then be combined with trace element analysis to finger-print cryptotephra signatures within MIS3. Samples containing glass shards within the uncertainty range of any MIS3 tephra should also undergo geochemical analysis to develop a better understanding of the use of ITRAX in identifying rhyolitic cryptotephra.

- To understand the wider regional processes driving ocean/climate variability in the SW Pacific during MIS3, additional high-resolution records are required. The terrestrial record of New Zealand covers MIS3 however, this is not at a high enough resolution to identify and recognise millennial scale events, although the ACR and Younger Dryas have been recorded at multiple sites. Ideally, high-resolution terrestrial records for MIS3 would be developed in both a North and South Island site, to give a latitudinal transect which will help in the comparison between both oceanic and atmospheric climate variability in the New Zealand region.

- Further analysis should also be done on the high-resolution records DSDP 594, MD97-2120 and MD06-2987 to allow a better correlation with TAN1106-28 and AIM events in the Antarctic record. The continued development of these records could include ITRAX analysis and high-resolution SST reconstructions, though this has been done for MD97-2121 Pahnke and Sachs (2006), and at a lower resolution for DSDP 594 (Barrows et al., 2007). The former could help develop a better understanding of how ITRAX element proxies respond to ocean/climate

variability. As the Kawakawa tephra has been identified in MD06-2991 in close proximity to MD06-2987 (Ryan et al., 2016), this will enable further examination of the response of ITRAX element profiles to rhyolitic tephra in marine sediment cores.

- To improve knowledge of the processes and mechanisms driving millennial scale events and how they are represented in New Zealand, high-resolution records from marine sediment cores should also be developed to the south and north of TAN1106-28 and MDD97-2121 respectively. A more northern core would be a tropical end member and may better constrain changes and causes of subtropical inflow and its extension as the ECC. A more southern core would show processes which occur in both the SW Pacific and the Southern Ocean, and may allow the separation between local processes and larger scale climate signals. This future research would provide insights into the processes and mechanisms influencing rapid climate changes events, which are likely to have implications for better projecting the response of New Zealand's ocean and climate to future warming.

8 Conclusions

Marine Isotope Stage 3 (MIS3) is an important period in the Earth's climate history as it contains the periodic occurrence of millennial scale events. These can be reconstructed to help interpret the response of Earths ocean/climate system to rapid climate events and this may have important connotations for the Earth's system response under anthropogenic induced climate change. In the Southern Ocean AIM events are recorded in the South Atlantic (Gottschalk et al., 2015; Barker et al., 2009), South Indian (Sicre et al., 2005), and SE Pacific (Caniupán et al., 2011) Oceans showing the extent of the Antarctic climate signal. This study helped contribute to mid-latitude marine sediment reconstructions by developing two high-resolution marine sediment core records either side of the STF in the New Zealand region of the SW Pacific. Comparison of the extent to which AIM events were recorded in these cores helped with the reconstruction of regional influences at both core sites, and showed the STF to block the expression of AIM events north of this frontal system.

To extract the Antarctic signal, $CaCO_3$ %, stable oxygen isotopes and ITRAX XRF analysis were used to reconstruct productivity variability and terrestrial accumulation at both core sites. ITRAX XRF is a relatively new type of analysis that has been sparsely used in Southern Hemisphere marine sediment cores. However, close correlations between ITRAX Ca and $CaCO_3$ % calculated using the vacuum gasometic procedure suggests ITRAX analysis successfully captures changes in carbonate production. Likewise, similarities in terrestrial MARs and ITRAX Ti/Ca ratios in TAN1106-28 suggests that terrestrial variation may also be recorded. ITRAX was also used to identify the Rotoehu, Tahuna and Kawakawa rhyolitic cryptotephra in MD97-2121. This analysis was only moderately successful as the ITRAX cryptotephra elemental proxies showed multiple cryptotephra events, and cryptotephra deposits then had to be recognised using a binocular microscope, and identified through EMP analysis, suggesting further research needs to be done to better refine the use of ITRAX for identifying cryptotephra.

At the site of TAN1106-28 millennial scale fluctuations in both productivity and terrestrial proxies appear to be driven by AIM events. Productivity increased during AIM events, and as ITRAX Fe and Ti profiles show an antiphased relationship with Ca and $CaCO_3$, this suggests that heightened productivity in the SAW (the main water mass at the TAN1106-28 core site) was not driven by the introduction of iron but must instead be a response to increased temperature and/or light availability. *G. bulloides* $\delta^{18}O$ showed no variation at the site of TAN1106-28 during AIM events suggesting a lack of SST variation, or alternatively, the limited reliability of this stable isotope record as an SST proxy at this location. However, SST reconstructions from the marine sediment cores SO136-GC3 (Barrows et al., 2007) and DSDP 594 (Barrows et al., 2007; Kowalski and Meyers, 1997; Nelson et al., 1993) in the SW Pacific, show SSTs that appear to vary in phase with $CaCO_3$ % and AIM events (within the constraints of the age model). As $\delta^{18}O$ is also a function of salinity and ice volume, this suggests that SST may contribute to increased productivity in the SW Pacific during MIS3 AIM events. Similar records have been reconstructed in the South Atlantic (Barker et al., 2009), South Indian (Sicre et al., 2005), and SE Pacific (Caniupán et al., 2011) suggesting changes in surface water temperatures during AIM events occur throughout the

Southern Ocean and may help drive increases in productivity during MIS3.

Terrigenous accumulation at the site of TAN1106-28 also varies with AIM events. Terrigenous accumulation is the primary contributor of sediment to the site of TAN1106-28, and therefore controls the linear sedimentation rate. During MIS3, glacio-eustatic sea level change strongly influenced Terrigenous accumulation at the site of TAN1106-28. During the LGM sea levels were 120 m lower than the present and this allowed rivers to transport sediment over the exposed continental shelf to the deep ocean. A lowering of sea levels heading into the MIS2 glaciation therefore likely contributed to the increase in terrigenous accumulation towards the end of MIS3. Superimposed on this sea level trend in ITRAX terrestrial proxies, is a series of millennial scale fluctuations which are lower in amplitude during AIM events. As the terrestrial record shows Southern Alps glaciers responded to the Younger Dryas (Doughty et al., 2013; Hajdas et al., 2006; Kaplan et al., 2010), it is likely that there was a similar glacial response to AIM events during MIS3. Therefore, millennial scale variation in terrigenous proxies during MIS3 was likely also a response to erosion variability associated with glacial advance and retreat which occurred out of phase with AIM events.

Like TAN1106-28, the dominant control on terrigenous accumulation at the site of MD97-2121 was sea level, and accumulation rates increased rapidly heading into the MIS2 glaciation. However, MD97-2121 shows very little of the millennial scale variability seen in the productivity and terrigenous proxies of TAN1106-28. This was inferred to be a reflection of the role played by the STF, which acted as a boundary to the SAW surface waters containing Antarctic signal, and buffering by subtropical influences. The ACR has been recorded in the Kaipo Bog pollen record (Hajdas et al., 2006) in close proximity to the site of MD97-2121. This suggests that atmospheric temperature variability in the region may have responded to MIS3 AIM events, and therefore, the muting of AIM events in MD97-2121 must be due to a restriction of SAW in this region by the STF. Some SAW likely made it to the site of MD97-2121 through the Mernoo Saddle, due to an enhanced SC (Carter et al., 2002; Nelson et al., 2000; Schaefer et al., 2005), and west along the Chatham Rise, due to a strengthened SAF (Carter et al., 2008; Schiraldi et al., 2014), however this inflow was not significant enough to overwhelm the tropical signal which is likely introduced to this site by the ECC. A strengthening of the ECC during warmer climates likely brought STW containing sediment from the high discharge Waiapu, and Waipaoa fluvial systems south to the site of MD97-2121 further diluting the Antarctic signal.

By analysing these high-resolution marine sediment records in the SW Pacific, interpretations can be made about how this system may respond to millennial scale events. It is apparent that the STF acts as a boundary to the Antarctic signal but, future research should look at developing a high-resolution record north of MD97-2121, to better extract the subtropical signal, and south of TAN1106-28, to develop a better understanding about the Southern Ocean response to AIM events. This would contribute to a better understanding about the mechanisms which drive millennial scale climate variability in the SW Pacific.

References

Agnihotri, R., Altabet, M. A., Herbert, T. D., and Tierney, J. E. (2008). Subdecadally resolved paleoceanography of the Peru margin during the last two millennia. *Geochemistry, Geophysics, Geosystems*, 9(5):n/a–n/a. Q05013.

Ahn, J. and Brook, Edward, J. (2014). Siple dome ice reveals two modes of millennial CO^2 change during the last ice age. *Nature Communications*, 5(3723).

Allan, A. S., Baker, J. A., Carter, L., and Wysoczanksi, R. J. (2008). Reconstructing the Quaternary evolution of the world's most active silicic volcanic system: insights from an 1.65 Ma deep ocean tephra record sourced from Taupo Volcanic Zone, New Zealand . *Quaternary Science Reviews*, 27(2526):2341 – 2360.

Alloway, B., Lowe, D., Chan, R., Eden, D., and Froggatt, P. (1994). Stratigraphy and chronology of the Stent tephra, a c. 4000 year old distal silicictephra from Taupo Volcanic Centre, New Zealand. *New Zealand Journal of Geology and Geophysics*, 37(1):37–47.

Álvarez-Solas, J., Montoya, M., Ritz, C., Ramstein, G., Charbit, S., Dumas, C., Nisancioglu, K., Dokken, T., and Ganopolski, A. (2011). Heinrich event 1: an example of dynamical ice-sheet reaction to oceanic changes. *Climate of the Past*, 7(4):1297–1306.

Andersen, K. K., Azuma, N., Barnola, J.-M., Bigler, M., Biscaye, P., Caillon, N., Chappellaz, J., Clausen, H. B., Dahl-Jensen, D., Fischer, H., et al. (2004). High-resolution record of northern hemisphere climate extending into the last interglacial period. *Nature*, 431(7005):147–151.

Andersen, K. K., Svensson, A., Johnsen, S. J., Rasmussen, S. O., Bigler, M., Röthlisberger, R., Ruth, U., Siggaard-Andersen, M.-L., Steffensen, J. P., Dahl-Jensen, D., et al. (2006). The greenland ice core chronology 2005, 15–42ka. part 1: Constructing the time scale. *Quaternary Science Reviews*, 25(23):3246–3257.

Balascio, L. N., Francus, P., Bradley, S. R., Schupack, B. B., Miller, H. G., Kvisvik, C. B., Bakke, J., and Thordarson, T. (2015). *Micro-XRF Studies of Sediment Cores: Applications of a non-destructive tool for the environmental sciences*, chapter Investigating the Use of Scanning X-Ray Fluorescence to Locate Cryptotephra in Minerogenic Lacustrine Sediment: Experimental Results, pages 305–324. Springer Netherlands, Dordrecht.

Barker, S. and Diz, P. (2014). Timing of the descent into the last Ice Age determined by the bipolar seesaw. *Paleoceanography*, 29(6):489–507.

Barker, S., Diz, P., Vautravers, M. J., Pike, J., Knorr, G., Hall, I. R., and Broecker, W. S. (2009). Interhemispheric Atlantic seesaw response during the last deglaciation. *Nature*, 457(7233).

Barrows, T. T., Juggins, S., De Deckker, P., Calvo, E., and Pelejero, C. (2007). Long-term sea surface temperature and climate change in the Australian-New Zealand region. *Paleoceanography*, 22(2).

Belkin, I. M. and Gordon, A. L. (1996). Southern Ocean fronts from the Greenwich meridian to Tasmania. *Journal of Geophysical Research: Oceans*, 101(C2):3675–3696.

Bereiter, B., Lüthi, D., Siegrist, M., Schüpbach, S., Stocker, T. F., and Fischer, H. (2012). Mode change of millennial CO^2 variability during the last glacial cycle associated with a bipolar marine carbon seesaw. *Proceedings of the National Academy of Sciences*, 109(25):9755–9760.

Blunier, T. and Brook, E. J. (2001). Timing of Millennial-Scale Climate Change in Antarctica and Greenland During the Last Glacial Period. *Science*, 291(5501):109–112.

Blunier, T., Chappellaz, J., Schwander, J., Dallenbach, A., Stauffer, B., Stocker, T. F., Raynaud, D., Jouzel, J., Clausen, H. B., Hammer, C. U., and Johnsen, S. J. (1998). Asynchrony of Antarctic and Greenland climate change during the last glacial period. *Nature*, pages 739–743.

Bond, G., Heinrich, H., Broecker, W., Labeyrie, L., McManus, J., Andrews, J., Huon, S., Jantschik, R., Clasen, S., Simet, C., Tedesco, K., Klas, M., Bonani, G., and Ivy, S. (1992). Evidence for massive discharges of icebergs into the North Atlantic ocean during the last glacial period. *Nature*, 360:245–249.

Bostock, H. C. (2011). RV Tangaroa voyage report: TAN1106-Solander Trough 10th April1st May 2011. Technical report, Unpublished The National Institute of Water and Atmospheric Research (NIWA) voyage report.

Bostock, H. C., Barrows, T. T., Carter, L., Chase, Z., Cortese, G., Dunbar, G., Ellwood, M., Hayward, B., Howard, W., Neil, H., et al. (2013). A review of the Australian-New Zealand sector of the Southern Ocean over the last 30 ka (Aus-INTIMATE project). *Quaternary Science Reviews*, 74:35–57.

Bostock, H. C., Hayward, B. W., Neil, H. L., Currie, K. I., and Dunbar, G. B. (2011). Deep-water carbonate concentrations in the southwest Pacific. *Deep Sea Research Part I: Oceanographic Research Papers*, 58(1):72 – 85.

Bostock, H. C., Hayward, B. W., Neil, H. L., Sabaa, A. T., and Scott, G. H. (2015). Changes in the position of the Subtropical Front south of New Zealand since the last glacial period. *Paleoceanography*, 30(7):824–844. 2014PA002652.

Boyd, P. W., McTainsh, G., Sherlock, V., Richardson, K., Nichol, S., Ellwood, M., and Frew, R. (2004). Episodic enhancement of phytoplankton stocks in New Zealand subantarctic waters: Contribution of atmospheric and oceanic iron supply. *Global Biogeochemical Cycles*, 18(1):n/a–n/a. GB1029.

Boyd, P. W., Watson, A. J., Law, C. S., Abraham, E. R., Trull, T., Murdoch, R., Bakker, D. C. E., Bowie, A. R., Buesseler, K. O., Chang, H., Charette, M., Croot, P., Downing, K., Frew, R., Gall, M., Hadfield, M., Hall, J., Harvey, M., Jameson, G., LaRoche, J., Liddicoat, M., Ling, R., Maldonado, M. T., McKay, R. M., Nodder, S., Pickmere, S., Pridmore, R., Rintoul, S., Safi, K., Sutton, P., Strzepek, R., Tanneberger, K., Turner, S., Waite, A., and Zeldis, J. (2000). A mesoscale phytoplankton bloom in the polar Southern Ocean stimulated by iron fertilization. *Nature*, 407():695–702.

Braun, H., Ditlevsen, P., and Chialvo, D. R. (2008). Solar forced Dansgaard-Oeschger events and their phase relation with solar proxies. *Geophysical Research Letters*, 35(6):n/a–n/a. L06703.

Broecker, W. and Clark, E. (2009). Ratio of coccolith $CaCO_3$ to foraminifera $CaCO_3$ in late Holocene deep sea sediments. *Paleoceanography*, 24(3):n/a–n/a. PA3205.

Broecker, W. S. (1998). Paleocean circulation during the last deglaciation: A bipolar seesaw? *Paleoceanography*, 13(2):119–121.

Bronk Ramsey, C. (2009). Dealing with outliers and offsets in radiocarbon dating. *Radiocarbon*, 51(3).

Bronk Ramsey, C. and Lee, S. (2013). Recent and planned developments of the program OxCal. *Radiocarbon*, 55():720–730.

Buizert, C. and Schmittner, A. (2015). Southern Ocean control of glacial AMOC stability and Dansgaard-Oeschger interstadial duration. *Paleoceanography*, 30(12):1595–1612.

Caniupán, M., Lamy, F., Lange, C. B., Kaiser, J., Arz, H., Kilian, R., Baeza Urrea, O., Aracena, C., Hebbeln, D., Kissel, C., Laj, C., Mollenhauer, G., and Tiedemann, R. (2011). Millennial-scale sea surface temperature and Patagonian Ice Sheet changes off southernmost Chile (53°S) over the past ≈60 kyr. *Paleoceanography*, 26(3):n/a–n/a.

Cartapanis, O., Bianchi, D., Jaccard, S. L., and Galbraith, E. D. (2016). Global pulses of organic carbon burial in deep-sea sediments during glacial maxima. *Nature communications*, 7.

Cartapanis, O., Tachikawa, K., and Bard, E. (2012). Latitudinal variations in intermediate depth ventilation and biological production over northeastern Pacific Oxygen Minimum Zones during the last 60 ka. *Quaternary Science Reviews*, 53:24 – 38.

Carter, L. and Manighetti, B. (2006). Glacial/interglacial control of terrigenous and biogenic fluxes in the deep ocean off a high input, collisional margin: A 139 kyr-record from New Zealand. *Marine Geology*, 226(34):307 – 322.

Carter, L., Manighetti, B., Elliot, M., Trustrum, N., and Gomez, B. (2002). Source, sea level and circulation effects on the sediment flux to the deep ocean over the past 15 ka off eastern New Zealand . *Global and Planetary Change*, 33(34):339 – 355.

Carter, L., Manighetti, B., Ganssen, G., and Northcote, L. (2008). Southwest Pacific modulation of abrupt climate change during the Antarctic Cold ReversalYounger Dryas. *Palaeogeography, Palaeoclimatology, Palaeoecology*, 260(12):284 – 298.

Carter, L., Neil, H., and McCave, I. (2000). Glacial to interglacial changes in non-carbonate and carbonate accumulation in the SW Pacific Ocean, New Zealand. *Palaeogeography, Palaeoclimatology, Palaeoecology*, 162(34):333 – 356.

Carter, R. M. and Gammon, P. (2004). New Zealand maritime glaciation: millennial-scale southern climate change since 3.9 Ma. *Science*, 304(5677):1659–1662.

Chiswell, S. M. (2000). The Wairarapa Coastal Current. *New Zealand Journal of Marine and Freshwater Research*, 34(2):303–315.

Chiswell, S. M., Bostock, H. C., Sutton, P. J., and Williams, M. J. (2015). Physical oceanography of the deep seas around New Zealand: a review. *New Zealand Journal of Marine and Freshwater Research*, 49(2):286–317.

Chiswell, S. M., Bradford-Grieve, J., Hadfield, M. G., and Kennan, S. C. (2013). Climatology of surface chlorophyll a, autumn-winter and spring blooms in the southwest Pacific Ocean. *Journal of Geophysical Research: Oceans*, 118(2):1003–1018.

Cobianchi, M., Mancin, N., Lupi, C., Bordiga, M., and Bostock, H. (2015). Effects of oceanic circulation and volcanic ash-fall on calcite dissolution in bathyal sediments from the SW Pacific Ocean over the last 550 ka. *Palaeogeography, Palaeoclimatology, Palaeoecology*, 429:72 – 82.

Crundwell, M., Scott, G., Naish, T., and Carter, L. (2008). Glacialinterglacial ocean climate variability from planktonic foraminifera during the Mid-Pleistocene transition in the temperate Southwest Pacific, ODP Site 1123 . *Palaeogeography, Palaeoclimatology, Palaeoecology*, 260(12):202 – 229. Antarctic cryosphere and Southern Ocean climate evolution (Cenozoic-Holocene)1) {EGU} Meeting, 2) {XXIX} {SCAR} Meeting.

Danisik, M., Shane, P., Schmitt, A. K., Hogg, A., Santos, G. M., Storm, S., Evans, N. J., Fifield, L. K., and Lindsay, J. M. (2012). Re-anchoring the late Pleistocene tephrochronology of New Zealand based on concordant radiocarbon ages and combined 238U/230Th disequilibrium and (UTh)/He zircon ages. *Earth and Planetary Science Letters*, 349350:240 – 250.

Dannenmann, S., Linsley, B. K., Oppo, D. W., Rosenthal, Y., and Beaufort, L. (2003). East Asian monsoon forcing of suborbital variability in the Sulu Sea during Marine Isotope Stage 3: Link to Northern Hemisphere climate. *Geochemistry, Geophysics, Geosystems*, 4(1):1–13.

Dansgaard, W., Oeschger, H., and Langway, C. C. (1983). *Palaeoclimatic Research and Models: Report and Proceedings of the Workshop held in Brussels, December 15–17, 1982*, chapter ICE Core Indications of Abrupt Climatic Changes, pages 72–73. Springer Netherlands, Dordrecht.

d'Orgeville, M., Sijp, W. P., England, M. H., and Meissner, K. J. (2010). On the control of glacial-interglacial atmospheric CO_2 variations by the Southern Hemisphere westerlies. *Geophysical Research Letters*, 37(21):n/a–n/a. L21703.

Doughty, A. M., Anderson, B. M., Mackintosh, A. N., Kaplan, M. R., Vandergoes, M. J., Barrell, D. J., Denton, G. H., Schaefer, J. M., Chinn, T. J., and Putnam, A. E. (2013). Evaluation of Lateglacial temperatures in the Southern Alps of New Zealand based on glacier modelling at Irishman Stream, Ben Ohau Range. *Quaternary Science Reviews*, 74:160–169.

Dowdeswell, J. A. (2009). *Encyclopedia of Paleoclimatology and Ancient Environments*, chapter Ice-Rafted Debris (IRD), pages 471–473. Springer Netherlands, Dordrecht.

Dürkop, A., Holbourn, A., Kuhnt, W., Zuraida, R., Andersen, N., and Grootes, P. M. (2008). Centennial-scale climate variability in the Timor Sea during Marine Isotope Stage 3. *Marine Micropaleontology*, 66(34):208 – 221.

EPICA community members (2006). One-to-one coupling of glacial climate variability in Greenland and Antarctica. *Nature*, 444:195–198.

Epica Community Members (2010). Stable oxygen isotopes of ice core edml. *PANGAEA*.

Fischer, H., Schmitt, J., Lüthi, D., Stocker, T. F., Tschumi, T., Parekh, P., Joos, F., Khler, P., Vlker, C., Gersonde, R., Barbante, C., Floch, M. L., Raynaud, D., and Wolff, E. (2010). The role of Southern Ocean processes in orbital and millennial CO^2 variations - A synthesis. *Quaternary Science Reviews*, 29(12):193 – 205. Climate of the Last Million Years: New Insights from {EPICA} and Other Records.

Froggatt, P. and Lowe, D. (1990). A review of late Quaternary silicic and some other tephra formations from New Zealand: Their stratigraphy, nomenclature, distribution, volume, and age. *New Zealand Journal of Geology and Geophysics*, 33(1):89–109.

Funk, J. A., Dobeneck, T., and Reitz, A. (2004a). *The South Atlantic in the Late Quaternary: Reconstruction of Material Budgets and Current Systems*, chapter Integrated Rock Magnetic and Geochemical Quantification of Redoxomorphic Iron Mineral Diagenesis in Late Quaternary Sediments from the Equatorial Atlantic, pages 237–260. Springer Berlin Heidelberg, Berlin, Heidelberg.

Funk, J. A., Dobeneck, T., Wagner, T., and Kasten, S. (2004b). *The South Atlantic in the Late Quaternary: Reconstruction of Material Budgets and Current Systems*, chapter Late Quaternary Sedimentation and Early Diagenesis in the Equatorial Atlantic Ocean: Patterns, Trends and Processes Deduced from Rock Magnetic and Geochemical Records, pages 461–497. Springer Berlin Heidelberg, Berlin, Heidelberg.

Gehrels, M. J., Newnham, R. M., Lowe, D. J., Wynne, S., Hazell, Z. J., and Caseldine, C. (2008). Towards rapid assay of cryptotephra in peat cores: review and evaluation of selected methods. *Quaternary International*, 178(1):68–84.

Gildor, H., Tziperman, E., and Toggweiler, J. R. (2002). Sea ice switch mechanism and glacial-interglacial CO^2 variations. *Global Biogeochemical Cycles*, 16(3):6–1–6–14.

Gottschalk, J., Skinner, L. C., and Waelbroeck, C. (2015). Contribution of seasonal sub-Antarctic surface water variability to millennial-scale changes in atmospheric CO_2 over the last deglaciation and Marine Isotope Stage 3. *Earth and Planetary Science Letters*, 411:87 – 99.

Graham, R. M., Boer, A. M. D., van Sebille, E., Kohfeld, K. E., and Schlosser, C. (2015). Inferring source regions and supply mechanisms of iron in the Southern Ocean from satellite chlorophyll data. *Deep Sea Research Part I: Oceanographic Research Papers*, 104:9 – 25.

Griggs, G. B., Carter, L., Kennett, J. P., and Carter, R. V. (1983). Late Quaternary marine stratigraphy southeast of New Zealand. *GSA Bulletin*, 94(6):791–797.

Hajdas, I., Lowe, D. J., Newnham, R. M., and Bonani, G. (2006). Timing of the late-glacial climate reversal in the Southern Hemisphere using high-resolution radiocarbon chronology for Kaipo bog, New Zealand. *Quaternary Research*, 65(2):340 – 345.

Hamilton, L. (2006). Structure of the Subtropical Front in the Tasman Sea . *Deep Sea Research Part I: Oceanographic Research Papers*, 53(12):1989 – 2009.

Hayward, B. W., Grenfell, H. R., Sabaa, A. T., and Neil, H. L. (2007). Factors influencing the distribution of Subantarctic deep-sea benthic foraminifera, Campbell and Bounty Plateaux, New Zealand. *Marine Micropaleontology*, 62(3):141 – 166.

Heath, R. (1981). Oceanic fronts around southern New Zealand. *Deep Sea Research Part A. Oceanographic Research Papers*, 28(6):547 – 560.

Heinrich, H. (1988). Origin and consequences of cyclic ice rafting in the Northeast Atlantic Ocean during the past 130,000 years. *Quaternary Research*, 29(2):142 – 152.

Hemming, S. R. (2004). Heinrich events: Massive late pleistocene detritus layers of the north atlantic and their global climate imprint. *Reviews of Geophysics*, 42(1):n/a–n/a.

Holt, K., Lowe, D., Cronin, S., Shane, P., Danisik, M., and Hogg, A. (2014). Developing a New Zealand tephrochronological framework for the SHAPE timeframe. *Annual conference of the Geoscience Society of New Zealand*, page 52.

Horrocks, M., Ogden, J., Nichol, S. L., Alloway, B. V., and Sutton, D. G. (2000). Palynology, sedimentology and environmental significance of Holocene swamps at northern Kaitoke, Great Barrier Island, New Zealand. *Journal of the Royal Society of New Zealand*, 30(1):27–47.

Howard, W. R. and Prell, W. L. (1994). Late Quaternary $CaCO_3$ production and preservation in the Southern Ocean: Implications for oceanic and atmospheric carbon cycling. *Paleoceanography*, 9(3):453–482.

Huang, E. and Tian, J. (2012). Sea-level rises at Heinrich stadials of early Marine Isotope Stage 3: Evidence of terrigenous n-alkane input in the southern South China Sea. *Global and Planetary Change*, 9495:1 – 12.

Huber, C., Leuenberger, M., Spahni, R., Flückiger, J., Schwander, J., Stocker, T. F., Johnsen, S., Landais, A., and Jouzel, J. (2006). Isotope calibrated Greenland temperature record over Marine Isotope Stage 3 and its relation to CH^4. *Earth and Planetary Science Letters*, 243(34):504 – 519.

Hulbe, C. L., MacAyeal, D. R., Denton, G. H., Kleman, J., and Lowell, T. V. (2004). Catastrophic ice shelf breakup as the source of Heinrich event icebergs. *Paleoceanography*, 19(1):n/a–n/a.

Jaccard, S., Hayes, C. T., Martínez-García, A., Hodell, D., Anderson, R. F., Sigman, D., and Haug, G. (2013). Two modes of change in Southern Ocean productivity over the past million years. *Science*, 339(6126):1419–1423.

Jeromson, M. R. (2016). The distribution and characteristics of turbidites in the Solander Trough, south of New Zealand. Master's thesis, University of Auckland.

Jones, G. A. and Kaiteris, P. (1983). A Vacuum-Gasometric Technique for Rapid and Precise Analysis of Calcium-Carbonate in Sediments and Soils. *Journal Of Sedimentary Petrology*, 53(2):655–660.

Jurado-Chichay, Z. and Walker, G. (2000). Stratigraphy and dispersal of the Mangaone Subgroup pyroclastic deposits, Okataina Volcanic Centre, New Zealand. *Journal of Volcanology and Geothermal Research*, 104(14):319 – 380.

Kaplan, M. R., Schaefer, J. M., Denton, G. H., Barrell, D. J., Chinn, T. J., Putnam, A. E., Andersen, B. G., Finkel, R. C., Schwartz, R., and Doughty, A. M. (2010). Glacier retreat in New Zealand during the Younger Dryas stadial. *Nature*, 467(7312):194–197.

Kindler, P., Guillevic, M., Baumgartner, M., Schwander, J., Landais, A., and Leuenberger, M. (2014). Temperature reconstruction from 10 to 120 kyr from the NGRIP ice core. *Climate of the Past*, 10(2):887–902.

Kohfeld, K., Graham, R., de Boer, A., Sime, L., Wolff, E., Qur, C. L., and Bopp, L. (2013). Southern Hemisphere westerly wind changes during the Last Glacial Maximum: paleo-data synthesis . *Quaternary Science Reviews*, 68:76 – 95.

Kohfeld, K. E., Quéré, C. L., Harrison, S. P., and Anderson, R. F. (2005). Role of Marine Biology in Glacial-Interglacial CO_2 Cycles. *Science*, 308(5718):74–78.

Kowalski, E. A. and Meyers, P. A. (1997). Glacialinterglacial variations in Quaternary production of marine organic matter at DSDP Site 594, Chatham Rise, southeastern New Zealand margin. *Marine Geology*, 140(34):249 – 263.

Kylander, M. E., Lind, E. M., Wastegrd, S., and Lwemark, L. (2012). Recommendations for using XRF core scanning as a tool in tephrochronology. *The Holocene*, 22(3):371–375.

Lamy, F., Gersonde, R., Winckler, G., Esper, O., Jaeschke, A., Kuhn, G., Ullermann, J., Martinez-Garcia, A., Lambert, F., and Kilian, R. (2014). Increased Dust Deposition in the Pacific Southern Ocean During Glacial Periods. *Science*, 343(6169):403–407.

Lamy, F., Kaiser, J., Ninnemann, U., Hebbeln, D., Arz, H. W., and Stoner, J. (2004). Antarctic Timing of Surface Water Changes off Chile and Patagonian Ice Sheet Response. *Science*, 304(5679):1959–1962.

Lascu, I., Feinberg, J. M., Dorale, J. A., Cheng, H., and Edwards, R. L. (2016). Age of the Laschamp excursion determined by U-Th dating of a speleothem geomagnetic record from North America. *Geology*, 44(2):139–142.

Le, J. and Shackleton, N. J. (1992). Carbonate Dissolution Fluctuations in the Western Equatorial Pacific During the Late Quaternary. *Paleoceanography*, 7(1):21–42.

Leduc, G., Thouveny, N., Bourlès, D., Blanchet, C., and Carcaillet, J. (2006). Authigenic 10 Be/9 Be signature of the Laschamp excursion: A tool for global synchronisation of paleoclimatic archives. *Earth and Planetary Science Letters*, 245(1):19–28.

Leduc, G., Vidal, L., Tachikawa, K., and Bard, E. (2009). ITCZ rather than ENSO signature for abrupt climate changes across the tropical Pacific? . *Quaternary Research*, 72(1):123 – 131.

Li, C., Battisti, D. S., Schrag, D. P., and Tziperman, E. (2005). Abrupt climate shifts in Greenland due to displacements of the sea ice edge. *Geophysical Research Letters*, 32(19):n/a–n/a. L19702.

Lisiecki, L. E. and Raymo, M. E. (2005). A Pliocene-Pleistocene stack of 57 globally distributed benthic d18O records. *Paleoceanography*, 20.

Lowe, D. J. (2011). Tephrochronology and its application: A review. *Quaternary Geochronology*, 6(2):107 – 153.

Lowe, D. J., Blaauw, M., Hogg, A. G., and Newnham, R. M. (2013). Ages of 24 widespread tephras erupted since 30,000 years ago in New Zealand, with re-evaluation of the timing and palaeoclimatic implications of the Lateglacial cool episode recorded at Kaipo bog. *Quaternary Science Reviews*, 74:170–194.

Maldonado, M. T., Strzepek, R. F., Sander, S., and Boyd, P. W. (2005). Acquisition of iron bound to strong organic complexes, with different Fe binding groups and photochemical reactivities, by plankton communities in Fe-limited subantarctic waters. *Global Biogeochemical Cycles*, 19(4):n/a–n/a. GB4S23.

Martin, J. H. (1990). Glacial-interglacial CO_2 change: The Iron Hypothesis. *Paleoceanography*, 5(1):1–13.

Martinez-Garcia, A., Rosell-Mele, A., Geibert, W., Gersonde, R., Masque, P., Gaspari, V., and Barbante, C. (2009). Links between iron supply, marine productivity, sea surface temperature, and CO_2 over the last 1.1 Ma. *Paleoceanography*, 24(1):n/a–n/a.

Martínez-Garcia, A., Rosell-Melé, A., Jaccard, S. L., Geibert, W., Sigman, D. M., and Haug, G. H. (2011). Southern Ocean dust-climate coupling over the past four million years. *Nature*, 476(7360):312–315.

Menviel, L., Spence, P., and England, M. (2015). Contribution of enhanced Antarctic Bottom Water formation to Antarctic warm events and millennial-scale atmospheric CO_2 increase. *Earth and Planetary Science Letters*, 413:37 – 50.

Mitchell, J., Mackay, K., Neil, H., Mackay, E., Pallentin, A., and P., N. (2012). Undersea New Zealand. NIWA Chart, Miscellaneous Series No. 92. 1:5,000,000.

Neil, H. L., Carter, L., and Morris, M. Y. (2004). Thermal isolation of Campbell Plateau, New Zealand, by the Antarctic Circumpolar Current over the past 130 kyr. *Paleoceanography*, 19(4):n/a–n/a.

Nelson, C., Hendy, I., Neil, H., Hendy, C., and Weaver, P. (2000). Last glacial jetting of cold waters through the Subtropical Convergence zone in the Southwest Pacific off eastern New Zealand, and some geological implications. *Palaeogeography, Palaeoclimatology, Palaeoecology*, 156(12):103 – 121.

Nelson, C. S., Cooke, P. J., Hendy, C. H., and Cuthbertson, A. M. (1993). Oceanographic and climatic changes over the past 160,000 years at Deep Sea Drilling Project Site 594 off southeastern New Zealand, southwest Pacific Ocean. *Paleoceanography*, 8(4):435–458.

NorthGRIP Community Members (2004). High-resolution record of Northern Hemisphere climate extending into the last interglacial period. *Nature*, 431(7005):147–151.

Orsi, A. H., III, T. W., and Jr., W. D. N. (1995). On the meridional extent and fronts of the Antarctic Circumpolar Current. *Deep Sea Research Part I: Oceanographic Research Papers*, 42(5):641 – 673.

Pahnke, K. and Sachs, J. P. (2006). Sea surface temperatures of southern midlatitudes 0-160 kyr b.p. *Paleoceanography*, 21(2):n/a–n/a.

Pedro, J. B., Bostock, H. C., Bitz, C. M., He, F., Vandergoes, M. J., Steig, E. J., Chase, B. M., Krause, C. E., Rasmussen, S. O., Markle, B. R., et al. (2015). The spatial extent and dynamics of the Antarctic Cold Reversal. *Nature Geoscience*.

Pickering, K. and Hiscott, R. (2015). *Deep Marine Systems: Processes, Deposits, Enivronments, Tectonics, and Sedimentation*. American Geophysical Union and Wiley, Chichester (West Sussex, UK).

Putnam, A. E., Denton, G. H., Schaefer, J. M., Barrell, D. J., Andersen, B. G., Finkel, R. C., Schwartz, R., Doughty, A. M., Kaplan, M. R., and Schlüchter, C. (2010). Glacier advance in southern middle-latitudes during the Antarctic Cold Reversal. *Nature Geoscience*, 3(10):700–704.

Rahmstorf, S. (2003). Timing of abrupt climate change: A precise clock. *Geophysical Research Letters*, 30(10):n/a–n/a.

Rasmussen, T. L., Thomsen, E., and Moros, M. (2016). North Atlantic warming during Dansgaard-Oeschger events synchronous with Antarctic warming and out-of-phase with Greenland climate. *Scientific Reports*, 6(20535).

Reimer, P., Bard, E., Bayliss, A., Beck, J., Blackwell, P., Ramsey, C. B., Buck, C., Cheng, H., Edwards, R. L., Friedrich, M., Grootes, P., Guilderson, T., Haflidason, H., Hajdas, I., Hatt, C., Heaton, T., Hoffmann, D., Hogg, A., Hughen, K., Kaiser, K., Kromer, B., Manning, S., Niu,

M., Reimer, R., Richards, D., Scott, E., Southon, J., Staff, R., Turney, C., and van der Plicht, J. (2013). IntCal13 and Marine13 Radiocarbon Age Calibration Curves 0-50,000 Years cal BP. *Radiocarbon*, 55(4).

Rothwell, R. G. and Croudace, I. W. (2015). *Micro-XRF Studies of Sediment Cores: Applications of a non-destructive tool for the environmental sciences*, chapter 2, Twenty Years of XRF Core Scanning Marine Sediments: What do Geochemical Proxies Tell Us? Developments in Paleoenvironmental Research. Springer Netherlands.

Ryan, M., Dunbar, G., Vandergoes, M., Neil, H., Hannah, M., Newnham, R., Bostock, H., and Alloway, B. (2012). Vegetation and climate in Southern Hemisphere mid-latitudes since 210 ka: new insights from marine and terrestrial pollen records from New Zealand. *Quaternary Science Reviews*, 48:80 – 98.

Ryan, M. T., Newnham, R. M., Dunbar, G. B., Vandergoes, M. J., Rees, A. B., Neil, H., Callard, S. L., Alloway, B. V., Bostock, H., Hua, Q., et al. (2016). Exploring the source-to-sink residence time of terrestrial pollen deposited offshore Westland, New Zealand. *Review of Palaeobotany and Palynology*, 230:37–46.

Sachs, J. P. and Anderson, R. F. (2005). Increased productivity in the subantarctic ocean during Heinrich events. *Nature*, 434(7037).

Saikku, R., Stott, L., and Thunell, R. (2009). A bi-polar signal recorded in the western tropical Pacific: Northern and Southern Hemisphere climate records from the Pacific warm pool during the last Ice Age. *Quaternary Science Reviews*, 28(2324):2374 – 2385.

Samson, C. R., Sikes, E. L., and Howard, W. R. (2005). Deglacial paleoceanographic history of the Bay of Plenty, New Zealand. *Paleoceanography*, 20(4).

Schaefer, G., Rodger, J. S., Hayward, B. W., Kennett, J. P., Sabaa, A. T., and Scott, G. H. (2005). Planktic foraminiferal and sea surface temperature record during the last 1 Myr across the Subtropical Front, Southwest Pacific. *Marine Micropaleontology*, 54(34):191 – 212.

Schiraldi, B., Sikes, E. L., Elmore, A. C., Cook, M. S., and Rose, K. A. (2014). Southwest Pacific subtropics responded to last deglacial warming with changes in shallow water sources. *Paleoceanography*, 29(6):595–611. 2013PA002584.

Schulz, M. (2002). On the 1470-year pacing of Dansgaard-Oeschger warm events. *Paleoceanography*, 17(2):.

Shackleton, N. J., Hall, M. A., and Vincent, E. (2000). Phase relationships between millennial-scale events 64,00024,000 years ago. *Paleoceanography*, 15(6):565–569.

Shane, P., Sikes, E., and Guilderson, T. (2006). Tephra beds in deep-sea cores off northern New Zealand: implications for the history of Taupo Volcanic Zone, Mayor Island and White Island volcanoes. *Journal of Volcanology and Geothermal Research*, 154(34):276 – 290.

Shin, S.-I., Liu, Z., Otto-Bliesner, B. L., Kutzbach, J. E., and Vavrus, S. J. (2003). Southern Ocean sea-ice control of the glacial North Atlantic thermohaline circulation. *Geophysical Research Letters*, 30(2).

Sicre, M. A., Labeyrie, L., Ezat, U., Duprat, J., Turon, J. L., Schmidt, S., Michel, E., and Mazaud, A. (2005). Mid-latitude Southern Indian Ocean response to Northern Hemisphere Heinrich events. *Earth and Planetary Science Letters*, 240(34):724 – 731.

Siddall, M., Rohling, E. J., Thompson, W. G., and Waelbroeck, C. (2008). Marine isotope stage 3 sea level fluctuations: Data synthesis and new outlook. *Reviews of Geophysics*, 46(4):n/a–n/a. RG4003.

Sigman, D. M., Hain, M. P., and Haug, G. H. (2010). The polar ocean and glacial cycles in atmospheric CO_2 concentration. *Nature*, 466(7302):47–55.

Sigman, D. M., Jaccard, S. L., and Haug, G. H. (2004). Polar ocean stratification in a cold climate. *Nature*, 428(6978):59–63.

Sikes, E. L. and Guilderson, T. P. (2016). Southwest Pacific Ocean surface reservoir ages since the last glaciation: Circulation insights from multiple-core studies. *Paleoceanography*, 31(2):298–310.

Sikes, E. L., Howard, W. R., Neil, H. L., and Volkman, J. K. (2002a). Glacial-interglacial sea surface temperature changes across the subtropical front east of New Zealand based on alkenone unsaturation ratios and foraminiferal assemblages. *Paleoceanography*, 17(2):2–1–2–13.

Sikes, E. L., Howard, W. R., Neil, H. L., and Volkman, J. K. (2002b). Glacial-interglacial sea surface temperature changes across the subtropical front east of New Zealand based on alkenone unsaturation ratios and foraminiferal assemblages. *Paleoceanography*, 17(2):2–1–2–13.

Sikes, E. L., Samson, C. R., Guilderson, T. P., and Howard, W. R. (2000). Old radiocarbon ages in the southwest Pacific Ocean during the last glacial period and deglaciation. *Nature*, 405.

Skinner, L., McCave, I., Carter, L., Fallon, S., Scrivner, A., and Primeau, F. (2015). Reduced ventilation and enhanced magnitude of the deep Pacific carbon pool during the last glacial period. *Earth and Planetary Science Letters*, 411:45 – 52.

Smith, R. O., Vennell, R., Bostock, H. C., and Williams, M. J. (2013). Interaction of the subtropical front with topography around southern New Zealand. *Deep Sea Research Part I: Oceanographic Research Papers*, 76:13 – 26.

Smith, V. and Shane, P. (2002). Geochemical characteristics of the widespread Tahuna Tephra. *New Zealand Journal of Geology and Geophysics*, 45(1):103–107.

Smith, V. C., Shane, P., and Smith, I. (2002). Tephrostratigrapy and geochemical fingerprinting of the Mangaone Subgroup tephra beds, Okataina Volcanic Centre, New Zealand. *New Zealand Journal of Geology and Geophysics*, 45(2):207–219.

Stanton, B. R. and Morris, M. Y. (2004). Direct velocity measurements in the Subantarctic Front and over Campbell Plateau, southeast of New Zealand. *Journal of Geophysical Research: Oceans*, 109(C1):n/a–n/a.

Stocker, T. F. and Johnsen, S. J. (2003). A minimum thermodynamic model for the bipolar seesaw. *Paleoceanography*, 18(4):n/a–n/a.

Stott, L., Poulsen, C., Lund, S., and Thunell, R. (2002). Super ENSO and Global Climate Oscillations at Millennial Time Scales. *Science*, 297(5579):222–226.

Sutton, P. J. H. (2003). The Southland Current: A subantarctic current. *New Zealand Journal of Marine and Freshwater Research*, 37(3):645–652.

Sutton, P. J. H. and Bowen, M. (2014). Flows in the Tasman Front south of Norfolk Island. *Journal of Geophysical Research: Oceans*, 119(5):3041–3053.

Talley, L. (2013). Closure of the global overturning circulation through the Indian, Pacic, and Southern Oceans: Schematics and transports. *Oceanography*.

Tilburg, C. E., Hurlburt, H. E., O'Brien, J. J., and Shriver, J. F. (2001). The Dynamics of the East Australian Current System: The Tasman Front, the East Auckland Current, and the East Cape Current. *Journal of Physical Oceanography*, 31(10):2917–2943.

Timmermann, A., Gildor, H., Schulz, M., and Tziperman, E. (2003). Coherent resonant millennial-scale climate oscillations triggered by massive meltwater pulses. *Journal of Climate*, 16(2569-2585).

Toggweiler, J. R., Russell, J. L., and Carson, S. R. (2006). Midlatitude westerlies, atmospheric CO_2, and climate change during the ice ages. *Paleoceanography*, 21(2):n/a–n/a. PA2005.

Vallelonga, P., Barbante, C., Cozzi, G., Gabrieli, J., Schüpbach, S., Spolaor, A., and Turetta, C. (2013). Iron fluxes to Talos Dome, Antarctica, over the past 200 kyr. *Climate of the Past*, 9(2):597–604.

Vandergoes, M. J., Hogg, A. G., Lowe, D. J., Newnham, R. M., Denton, G. H., Southon, J., Barrell, D. J., Wilson, C. J., McGlone, M. S., Allan, A. S., Almond, P. C., Petchey, F., Dabell, K., Dieffenbacher-Krall, A. C., and Blaauw, M. (2013). A revised age for the Kawakawa/Oruanui tephra, a key marker for the Last Glacial Maximum in New Zealand. *Quaternary Science Reviews*, 74:195 – 201.

Vogel, H., Zanchetta, G., Sulpizio, R., Wagner, B., and Nowaczyk, N. (2010). A tephrostratigraphic record for the last glacialinterglacial cycle from Lake Ohrid, Albania and Macedonia. *Journal of Quaternary Science*, 25(3):320–338.

Volat, J.-L., Pastouret, L., and Vergnaud-Grazzini, C. (1980). Dissolution and carbonate fluctuations in Pleistocene deep-sea cores: A review. *Marine Geology*, 34(1):1 – 28.

Wang, Y. J., Cheng, H., Edwards, R. L., An, Z. S., Wu, J. Y., Shen, C.-C., and Dorale, J. A. (2001). A High-Resolution Absolute-Dated Late Pleistocene Monsoon Record from Hulu Cave, China. *Science*, 294(5550):2345–2348.

Watanabe, O., Jouzel, J., Johnsen, S., Parrenin, F., Shoji, H., and Yoshida, N. (2003). Homogeneous climate variability across East Antarctica over the past three glacial cycles. *Nature*, 422(6931):509–512.

Weaver, P. P. E., Carter, L., and Neil, H. L. (1998). Response of surface water masses and circulation to Late Quaternary climate change east of New Zealand. *Paleoceanography*, 13(1):70–83.

Weltje, G. J. and Tjallingii, R. (2008). Calibration of XRF core scanners for quantitative geochemical logging of sediment cores: Theory and application. *Earth and Planetary Science Letters*, 274(34):423 – 438.

Westerhold, T., Rhl, U., McCarren, H. K., and Zachos, J. C. (2009). Latest on the absolute age of the Paleocene-Eocene Thermal Maximum (PETM): New insights from exact stratigraphic position of key ash layers + 19 and 17. *Earth and Planetary Science Letters*, 287(34):412 – 419.

Zhang, X., Prange, M., Merkel, U., and Schulz, M. (2014). Instability of the Atlantic overturning circulation during Marine Isotope Stage 3. *Geophysical Research Letters*, 41(12):4285–4293.

Ziegler, M., Diz, P., Hall, I. R., and Zahn, R. (2013). Millennial-scale changes in atmospheric CO_2 levels linked to the Southern Ocean carbon isotope gradient and dust flux. *Nature Geoscience*, 6(6):457–461.

Ziegler, M., Lourens, L. J., Tuenter, E., and Reichart, G.-J. (2010). High Arabian Sea productivity conditions during MIS 13 - odd monsoon event or intensified overturning circulation at the end of the Mid-Pleistocene transition? *Climate of the Past*, 6(1):63–76.

Appendix 1: Tephra analysis

Depth (cm)	SiO_2	TiO_2	Al_2O_3	FeO	MnO	MgO	CaO	Na_2O	K_2O	Cr_2O_3	n
1434	78.20	0.13	12.58	1.20	0.04	0.08	0.78	3.49	3.49	0.01	25
	0.41	0.02	0.1	0.19	0.02	0.01	0.02	0.16	0.27	0.01	
1345	78.23	0.16	12.50	0.98	0.03	0.11	0.96	3.36	3.66	0.01	16
	0.30	0.02	0.13	0.06	0.03	0.02	0.03	0.12	0.24	0.01	
982	77.96	0.17	12.73	1.17	0.06	0.12	1.11	3.62	3.05	0.02	6
	0.05	0.03	0.08	0.08	0.01	0.02	0.03	0.07	0.07	0.03	

Table 1: Major element oxide % from tephra within MD97-2121

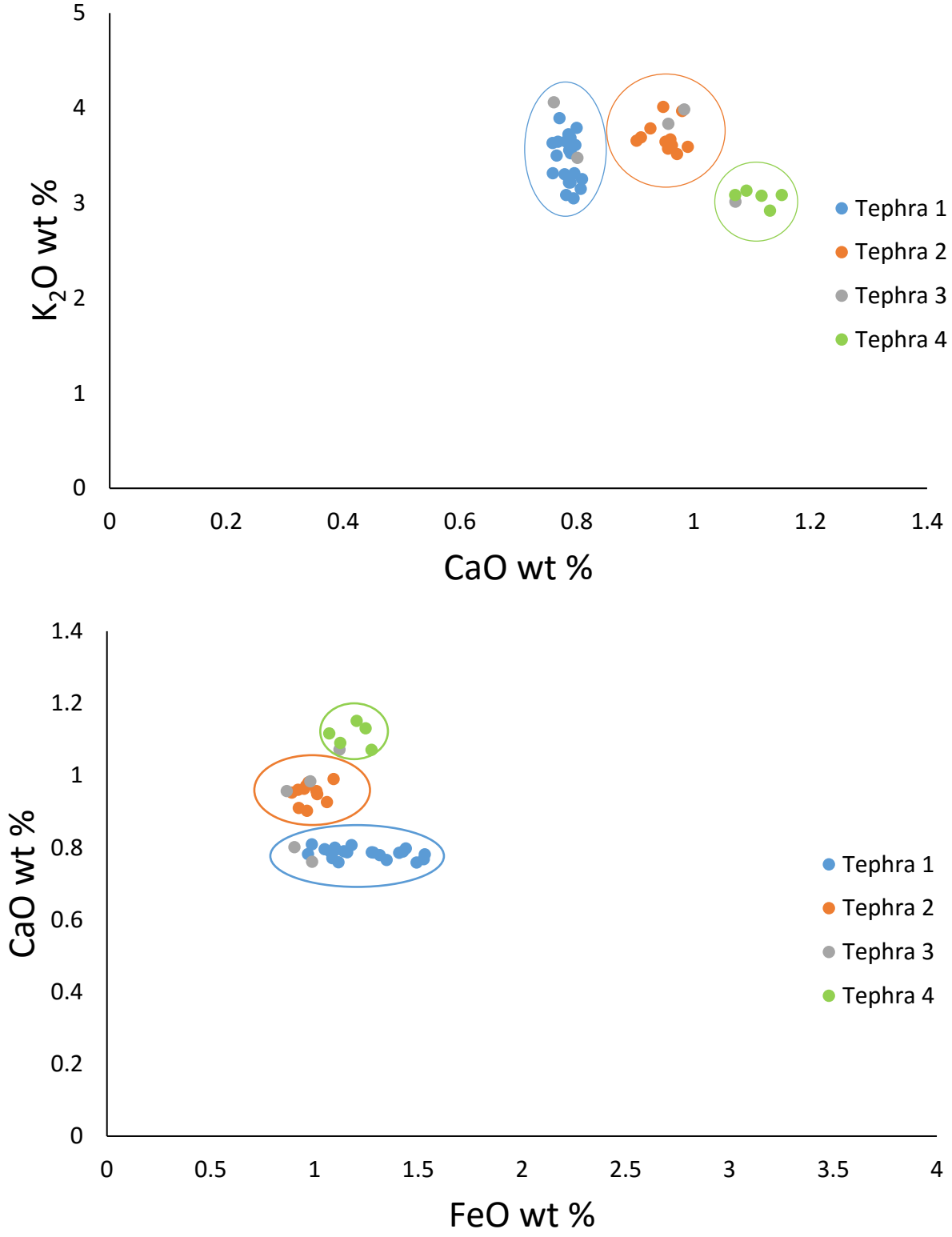

Figure .0.1: EMP FeO and CaO percentages from glass shards. Tephra 1 = blue, tephra 2 = red, tephra 3 = green, and tephra 4 = purple.

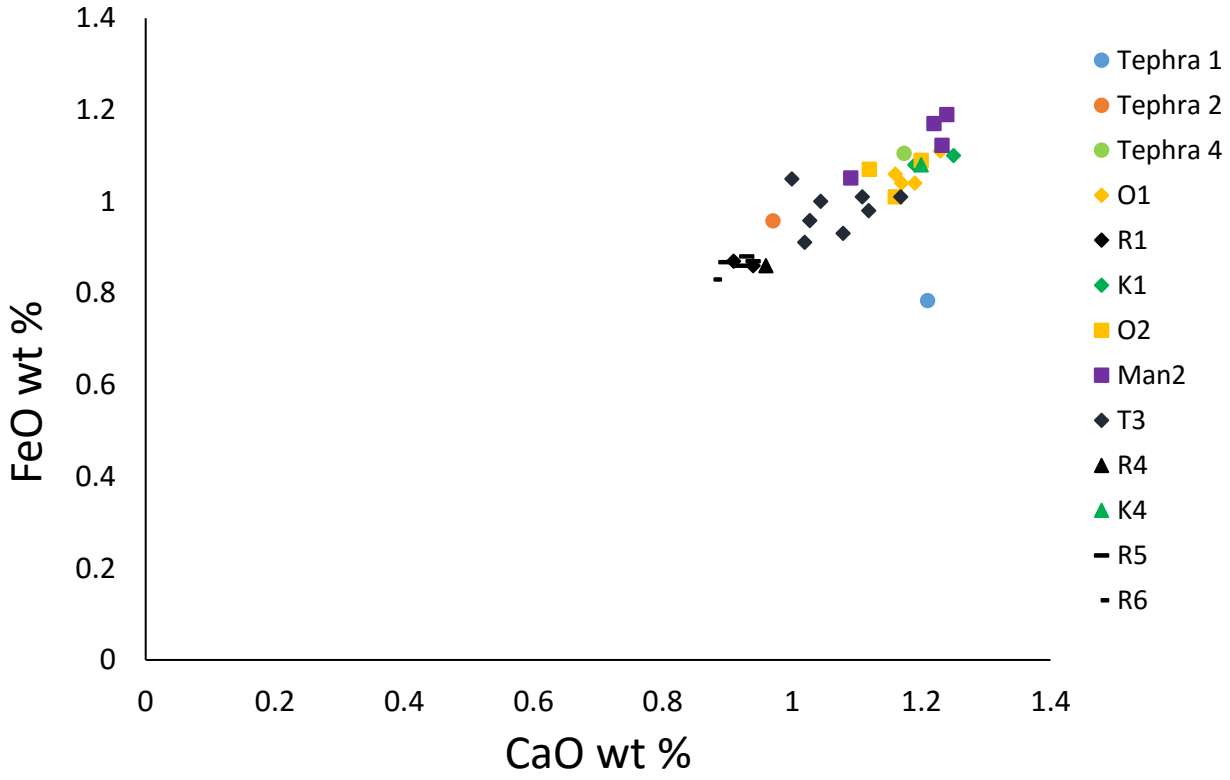

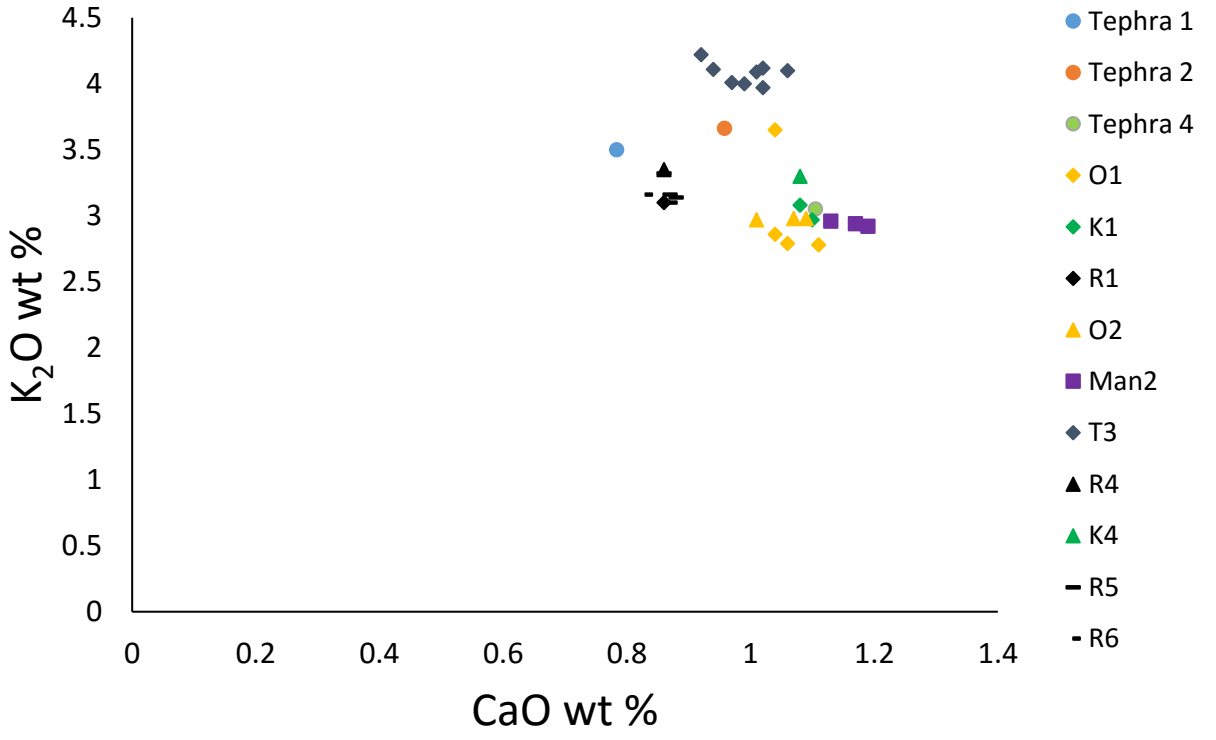

Figure .0.2: Analysing the major element composition of tephra 1, 2, and 3. R=Rotoehu, T=Tahuna, H=Hauparu, M=Maketu, Man=Mangaone, O=Omataroa and K=Kawakawa. 1=Allan et al. (2008), 2=Smith et al. (2002), 3=Smith and Shane (2002), 4=Shane et al. (2006), 5=Horrocks et al. (2000) and 6=Alloway et al. (1994)

Appendix 2: Oxcal Age models

TAN1106-28

```
Plot()
{
Curve("Marine13","Marine13.14c");
Delta_R("LocalMarine", 400,400);
Outlier_Model("General",T(5),U(0,4),"t");
P_Sequence("variable",1,1,U(-2,2))
{
Boundary()
{
z=455;
};
R_Date("330-331",43730,400)
{
z=330.5;
Outlier( 0.05);
};
R_Date("313-314",40930,330)
{
z=313.5;
Outlier( 0.05);
};
R_Date("283-284",35130,200)
{
z=283.5;
Outlier( 0.05);
};
R_Date("273-274",32660,160)
{
z=273.5;
Outlier( 0.05);
};
R_Date("255-256",30170,120)
{
z=255.5;
Outlier( 0.05);
};
R_Date("243-244",29450,120)
{
z=243.5;
```

```
Outlier( 0.05);
};
R_Date("218-219",26440,100)
{
z=218.5;
Outlier( 0.05);
};
R_Date("175-176",22900,80)
{
z=175.5;
Outlier( 0.05);
};
R_Date("133-134",20930,70)
{
z=133.5;
Outlier( 0.05);
};
R_Date("80-81",16716,53)
{
z=80.5;
Outlier( 0.05);
};
R_Date("50-51",10972,31)
{
z=50.5;
Outlier( 0.05);
};
R_Date("10-11",2860,18)
{
z=10.5;
Outlier( 0.05);
};
Boundary()
{
};
};
};
```

TAN1106-28 OxCal age model

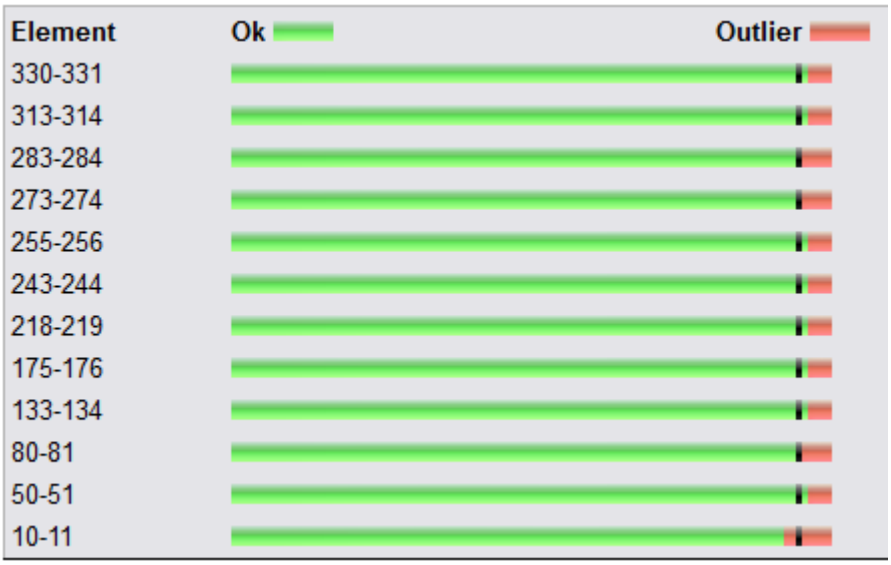

Figure .0.3: Outlier model for TAN1106-28. Element shows the depth of the age sample in cm, or identifies tephra and the MIS4 isotope drop. The thick black line shows 95% convergence between the calibrated age and the modelled age. The green bar shows agreement and the red shows outliers. All dates were run on a general outlier model looking for outliers in time (t)

MD97-2121

Plot()

Curve("Marine13","Marine13.14c");
Delta_R("LocalMarine", 400,400);
Outlier_Model("General",T(5),U(0,4),"t");
P_Sequence("variable",1,0.2,U(-2,2))
{
Boundary()
{
z=1850;
};
C_Date("IsotopeDrop",-58368,100)
{
z=1800;
Outlier(0.05);
};
R_Date("1490-1491",38710,410)
{
z=1490.5;
Outlier(0.05);
};
R_Date("1439-1440",43500,330)
{
z=1439.5;
Outlier(0.05);

};
R_Date("1434-1435",38660,260)
{
z=1434.5;
Outlier(0.05);
};
C_Date("Rotoehu",-43150,4000)
{
z=1433.5;
Outlier(0.05);
};
R_Date("1432-1433",40010,250)
{
z=1432.5;
Outlier(0.05);
};
R_Date("1395-1396",33120,150)
{
z=1395.5;
Outlier(0.05);
};
R_Date("1353-1354",31890,350)
{
z=1353.5;
Outlier(0.05);
};
R_Date("1346-1347",37940,230)
{
z=1346.5;
Outlier(0.05);
};
C_Date("Tahuna",-37350,2400)
{
z=1345.5;
Outlier(0.05);
};
R_Date("1344-1345",32160,140)
{
z=1344.5;
Outlier(0.05);
};
R_Date("1309-1310",33590,550)
{
z=1309.5;
Outlier(0.05);
};
R_Date("1268-1269",31500,140)

```
{
z=1268.5;
Outlier( 0.05);
};
R_Date("1234-1235",31090,250)
{
z=1234.5;
Outlier( 0.05);
};
R_Date("1195-1196",29810,140)
{
z=1195.5;
Outlier( 0.05);
};
R_Date("1154-1155",28250,170)
{
z=1154.5;
Outlier( 0.05);
};
R_Date("1126-1127",26250,150)
{
z=1126.5;
Outlier( 0.05);
};
R_Date("1085-1086",25500,100)
{
z=1085.5;
Outlier( 0.05);
};
R_Date("1041-1042",24050,130)
{
z=1041.5;
Outlier( 0.05);
};
R_Date("984-985",22450,130)
{
z=984.5;
Outlier( 0.05);
};
C_Date("Kawakawa",-23410,160)
{
z=982.5;
Outlier ( 0.05);
};
R_Date("872-873",19920,100)
{
z=872.5;
```

```
Outlier( 0.05);
};
R_Date("748-749",17550,110)
{
z=748.5;
Outlier( 0.05);
};
C_Date("Rerewhakaaitu",-15546, 462)
{
z=670.5;
Outlier( 0.05);
};
R_Date("514-515",12664, 60)
{
z=514.5;
outlier( 0.5);
};
C_Date("Waiohau",-12059, 155)
{
z=510.5;
Outlier( 0.05);
};
R_Date("480-481",12265,96)
{
z=480.5;
Outlier(0.05);
};
R_Date("420-421",10818,70)
{
z=420.5;
Outlier( 0.05);
};
C_Date("Poronui", -9220, 115)
{
z=408.5;
Outlier( 0.05);
};
C_Date("Rotoma",-7473, 120)
{
z=342.5;
Outlier( 0.05);
};
R_Date("310-311",8286,60)
{
z=310.5;
Outlier( 0.05);
};
```

C_Date("Tuhua", -4627, 547)
{
z=270.5;
Outlier(0.05);
};
R_Date("196-197",5379,57)
{
z=196.5;
Outlier(0.05);
};
C_Date("Whakatane",-3576, 145)
{
z=190.5;
Outlier(0.05);
};
R_Date("110-111",3241,56)
{
z=110.5;
Outlier(0.05);
};
C_Date("Waimihia",-1451, 108)
{
z=106.5;
Outlier(0.05);
};
R_Date("58-59",2203,56)
{
z=58.5;
Outlier(0.05);
};
C_Date("Taupo",232, 10)
{
z=54.5;
Outlier(0.05);
};
R_Date("40-41",1748,56)
{
z=40.5;
Outlier(0.05);
};
R_Date("35-36",1139,60)
{
z=35.5;
Outlier(0.05);
;
R_Date("19-20",1032,60)
{

```
z=19.5;
Outlier( 0.05);
};
Boundary()
{
z=0;
};
};
};
```

MD97-2121 age model

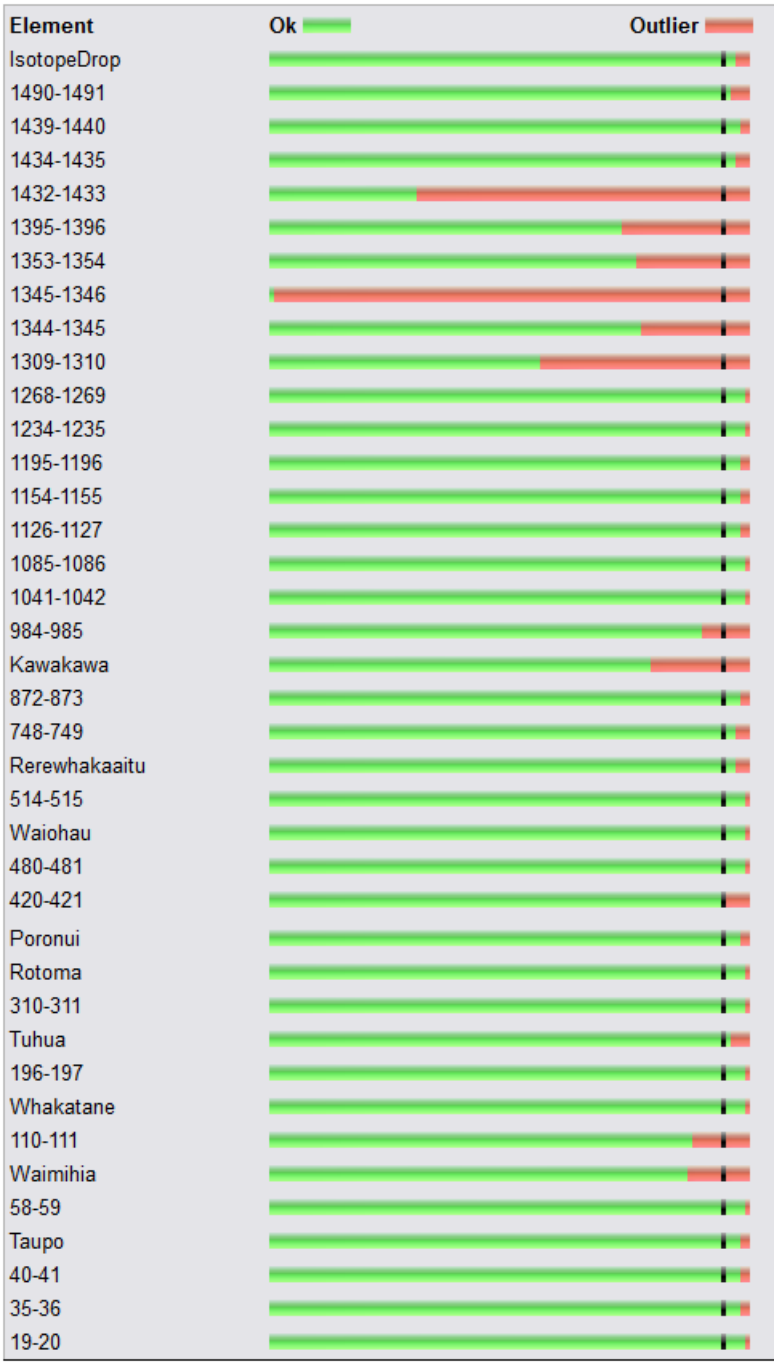

Figure .0.4: Outlier model for MD97-2121. Element shows the depth of the age sample in cm, or identifies tephra and the MIS4 isotope drop. The thick black line shows 95% convergence between the calibrated age and the modelled age. The green bar shows agreement and the red shows outliers. All dates were run on a general outlier model looking for outliers in time (t)

Appendix 3: ITRAX data

See CD-ROM

Appendix 4: Grainsize, $CaCO_3$ and Stable isotope data

See CD-ROM